UNIVERSITY OF CALIFORNIA SAN DIEGO

Characterizing land-atmosphere interactions with surface air temperature variability and heat wave intensity

A dissertation submitted in partial satisfaction of the
requirements for the degree
Doctor of Philosophy

in

Oceanography

by

Anna Louise Merrifield

Committee in charge:

Shang-Ping Xie, Chair
Daniel R. Cayan
Carlos F. Coimbra
Clara Deser
Amato T. Evan
Joel R. Norris

2018

The dissertation of Anna Louise Merrifield is approved, and it is acceptable in quality and form for publication on microfilm and electronically:

_____

_____

_____

_____

_____

_____

Chair

University of California San Diego

2018

DEDICATION

Dedicated to my family.

EPIGRAPH

"See here how everything
led up to this day,
and it’s just like any other day
that’s ever been."

— Robert Hunter and Jerry Garcia

TABLE OF CONTENTS

LIST OF FIGURES

LIST OF TABLES

ACKNOWLEDGEMENTS

I would like thank my advisor, Dr. Shang-Ping Xie, for his guidance. I benefited immeasurably from our meetings and have always felt so privileged to be a part of the Xie group. I would like to acknowledge my committee members at SIO, Dr. Dan Cayan, Dr. Carlos Coimbra, Dr. Amato Evan, and Dr. Joel Norris, for their advice and feedback on this dissertation. I would also like to thank my committee member and supervisor at NCAR, Dr. Clara Deser, for giving me the opportunity to work with and learn from her and the CAS group. It was an amazing opportunity.

This dissertation is a collection of papers that have been accepted or are in preparation for publication.

Chapter 2, in full, is a reprint of the material as it appears in *Journal of Climate*, 2016: Anna L. Merrifield and Shang-Ping Xie, "Summer U.S. Surface Air Temperature Variability: Controlling Factors and AMIP Simulation Biases." The dissertation author was the primary investigator and author of this paper.

Chapter 3, in full, is a reprint of the material as it appears in *Geophysical Research Letters*, 2017: Anna L. Merrifield, Flavio Lehner, Shang-Ping Xie, and Clara Deser, "Removing Circulation Effects to Assess Central U.S. Land-Atmosphere Interactions in the CESM Large Ensemble." The dissertation author was the primary investigator and author of this paper.

Chapter 5, in part is currently being prepared for submission for publication of the material. Anna L. Merrifield, Isla R. Simpson, and Clara Deser. The dissertation/thesis author was the primary investigator and author of this material.

VITA

2013	B.S., Physics Massachusetts Institute of Technology
2013–2018	Graduate Student Researcher Climate, Atmospheric Science & Physical Oceanography, University of California, San Diego
2014	M.S., Earth Sciences Scripps Institution of Oceanography, University of California, San Diego
2018	Ph.D., Oceanography Scripps Institution of Oceanography, University of California, San Diego

PUBLICATIONS

Journal Articles

1. Merrifield, A. L., F. Lehner, S.-P. Xie, & C. Deser (2017). Removing Circulation Effects to Assess Central US Land-Atmosphere Interactions in the CESM Large Ensemble. *Geophysical Research Letters*, 44(19):9938-9946.
2. Merrifield, A. L. & S.-P. Xie (2016). Summer US surface air temperature variability: Controlling factors and AMIP simulation biases. *Journal of Climate*, 29(14):5123-5139.

Conference Presentations

1. Merrifield, A. L., F. Lehner, S.-P. Xie, & C. Deser (2017). Removing Circulation Effects to Assess Land-Atmosphere Interactions in Observations and GLACE-CMIP5. American Geophysical Union Fall Meeting, New Orleans, LA. Oral Presentation.
2. Merrifield, A. L., F. Lehner, S.-P. Xie, & C. Deser (2017). Assessing Northern Hemisphere Land-Atmosphere Hotspots Using Dynamical Adjustment. European Geophysical Union General Assembly. Vienna, Austria. Poster.
3. Merrifield, A. L., F. Lehner, S.-P. Xie, & C. Deser (2017). Assessing Northern Hemisphere Land-Atmosphere Hotspots Using Dynamical Adjustment. Fourth Santa Fe Conference on Global & Regional Climate Change. Santa Fe, NM. Oral Presentation.
4. Merrifield, A. L., C. Deser, S.-P. Xie, L. Terray, F. Lehner, & A. S. Phillips (2016). Assessing the Central US Land-Atmosphere Hotspot using Dynamical Adjustment. American Geophysical Union Fall Meeting. San Francisco, CA. Poster.

5. Merrifield, A. L., F. Lehner, L. Terray, & C. Deser (2016). U. S. Warm Season Temperature - Precipitation Relationships in the CESM Large Ensemble. Community Earth System Model Workshop. Breckenridge, CO. Poster.
6. Merrifield, A. L., N.C. Johnson, Y. Kosaka, & S.-P. Xie (2014). Understanding the Influence of Terrestrial Water Anomalies on Summer Surface Air Temperature Variability over North America. American Geophysical Union Fall Meeting. San Francisco, CA. Poster.
7. Merrifield, A. L., R. G. Prinn, & S. Ono (2012). An Ongoing Observational Study of Greenhouse Gas Emissions in the Greater Boston Area. American Geophysical Union Fall Meeting. San Francisco, CA. Poster.

ABSTRACT OF THE DISSERTATION

Characterizing land-atmosphere interactions with surface air temperature variability and heat wave intensity

by

Anna Louise Merrifield

Doctor of Philosophy in Oceanography

University of California, San Diego, 2018

Shang-Ping Xie, Chair

A series of model simulations and statistical analyses are used to examine the drivers of summer surface air temperature (SAT) variability over the continental United States (US) and the drivers of extreme heat events over Europe. An overarching goal is to improve understanding of the land-surface feedback on summer SAT, a topic of considerable socioeconomic importance. North American summer SAT variability is well-observed and known to be influenced strongly by the large-scale atmospheric circulation as well as by the land surface. Current global climate models forced with observed sea surface temperature tend to overestimate year-to-year summer SAT variations, notably in the central US, which has been identified as a "hot spot" of land-atmosphere

interaction. Chapter 2 explores the hypothesis that models are overly sensitive to variations in soil moisture in the central US. Evidence is presented that links central US SAT variability in models to sensible heat flux variability, an indicator of soil moisture influence. However, the "true" influence of the land surface on SAT is not well constrained by observations and is challenging to characterize in the presence of internal atmospheric variability.

A technique called dynamical adjustment is used to separate the influence of atmospheric circulation on SAT from the influence of the land surface on SAT. It is shown in Chapter 3 that removing the effect of circulation on SAT strengthens the correlation between preseason soil moisture and SAT in the central US. Uncertainty associated with dynamical adjustment is assessed in Chapter 4, and it is confirmed that the influence of the land surface on SAT can be characterized using solely SAT and atmospheric pressure, which are well-observed fields. Extreme summer SAT in Europe is also influenced by atmospheric circulation and the land surface; the impact of preseason soil moisture on a seasonally persistent European heat wave event is assessed in Chapter 5. By superposing the same heat wave circulation pattern on an initial condition ensemble, it is shown that a heat wave following a dry spring can be up to 3°C hotter than a heat wave following a wet spring.

Chapter 1

Introduction

Climate models are important tools. They help us to better understand climate variability and allow us to make conjectures about future climate change. While we will have to wait to determine the accuracy of climate model projections, we can assess a model's ability to represent things like surface air temperature (SAT) variability, which have been carefully observed (Brohan et al., 2006). Broadly, this dissertation focuses on the simulation of SAT in climate models, in order to improve understanding of the physical processes that contribute to interannual fluctuations and seasonal extremes. More specifically, we assess summer SAT over land in the Northern Hemisphere (NH) midlatitudes and demonstrate how its year-to-year variability and its intensity during a heat wave can be used to characterize the more complex, more sparsely observed land surface feedback.

Summer is a season of socioeconomic importance in both the United States (US) and Europe, and exceptionally hot summers pose risks to human health and livelihood which are and will continue to be difficult to cope with (Hansen et al., 2012). Prior notice of an exceptionally warm summer would be valuable, but such predictions can only be made if climate models accurately represent observed climate. Current climate models tend to share systematic biases, and notably overestimate year-to-year variations in summer SAT in the central US (Mueller and

Seneviratne, 2014; Berg et al., 2014; Merrifield and Xie, 2016).

Model biases are often caused by a misrepresentation of underlying physical processes. Summer SAT variability in the central US is controlled by midlatitude atmospheric circulation patterns, but the region has also been identified as a "hot spot" of land-atmosphere interaction (e.g. Koster et al., 2004a). SAT biases in the central US may be related to an excessive land-atmosphere interaction in models; we investigate this hypothesis in Chapter 2.

The land surface influences the atmosphere through a series of nonlinear processes, which link soil moisture and vegetation with evapotranspiration, the evolution of the planetary boundary layer, cloud formation and precipitation (e.g. Findell and Eltahir, 2003a; Tawfik et al., 2015a,b; Santanello et al., 2017). These processes feedback on one another and modify SAT on diurnal to synoptic timescales in ways that are difficult, if not prohibitively expensive to directly observe (Jimenez et al., 2014; Ferguson et al., 2012). Due to a lack of long, large-scale, direct measurements of land surface properties (and the spatial and temporal heterogeneity of the land surface), the coupling between the land surface and atmosphere is not yet well constrained (e.g. Findell, 2015; Santanello et al., 2017).

On climate time-scales of a month or longer, the complexity of the land surface's influence on SAT can be represented to first order by soil moisture and surface fluxes (Seneviratne et al., 2010, 2013). The notion of hot spots comes from the theory that, in certain regions, the presence (absence) of soil moisture partitions the outgoing turbulent heat flux towards evapotranspiration (the sensible heat flux). Because the phase change of water requires energy, SAT tends to be cooler over a wetter land surface. When conditions are dry, there is more sensible heating of the atmosphere. There are two primary factors that determine if soil moisture variability is driving variations in SAT: its control on evapotranspiration and its magnitude. Evapotranspiration is a key component of global water and energy cycles, recycling around 60% of terrestrial precipitation (Oki and Kanae, 2006) and using more than half of the total solar energy absorbed by the land surface (Trenberth et al., 2009). In regions where water is scarce, such as the arid southwestern

US, evapotranspiration is strongly controlled by soil moisture, but soil moisture has little impact on SAT variability because the absolute magnitude evapotranspiration is near zero. In wet regions, such as the humid eastern US, the absolute magnitude of evapotranspiration is large enough to influence the atmosphere, but its variability is controlled by the availability of incoming energy rather than the availability of water. Therefore, hot spots, where soil moisture exerts influence on SAT through surface fluxes are located in transition regions between arid and humid climate zones, like the central US (Findell and Eltahir, 2003b; Seneviratne et al., 2010; **?**).

Hot spots were first defined within a climate model framework, in part because models allow for the comparison between coupled and uncoupled land-atmosphere regimes (Lorenz et al., 2015). The Global Land-Atmosphere Coupling Experiment (GLACE) was initiated by Koster et al. (2006, 2011) as a means of comprehensively evaluating the land-atmosphere coupling strength in climate models. In GLACE, the strength of the soil moisture-SAT coupling is determined by comparing SAT variance in interactive and prescribed soil moisture simulations. Regions where multiple models agree that SAT variability is enhanced in the coupled simulation when compared to the prescribed soil moisture simulation were defined as hot spots. Though models may agree on hot spots because they share the same biases (Koster et al., 2006), the GLACE-derived hot spot in the central US remains well accepted by the climate modeling community (e.g. Seneviratne et al., 2006a; Zhang et al., 2008; Krakauer et al., 2010; Guo and Dirmeyer, 2013; Berg et al., 2014; **?**).

Although there is model consensus that the land-atmosphere coupling is strong in the central US, observational evidence for the hot spot is less conclusive (e.g. Findell et al., 2011; Song et al., 2016). Miralles et al. (2012) and Ford and Quiring (2014) presented evidence in support of the central US. land-atmosphere hotspot in reanalysis products and in-situ observations respectively. Using remote sensing measurements of the land surface, **?**Ferguson et al. (2012) determined that land-atmosphere coupling strength is generally overestimated by land models, but didn't rule out a central U.S. hotspot relative to other parts of the world. Phillips and Klein

(2014) indicate that the energetic forcing of the atmosphere on the land surface is substantial in the central US, but the land's energetic feedback on the atmosphere is comparatively weak. Assessments of North American hydroclimate variability report that local evaporation in the central US can be up to 4 times larger in models than in observationally constrained estimates, suggesting land-atmosphere interactions are overemphasized in models (Ruiz-Barradas and Nigam, 2005; Wu and Dickinson, 2005; Ruiz-Barradas and Nigam, 2006, 2013).

It is unclear if this disaccord between models and observations is due to a misrepresentation of the land surface feedback in models or due to a lack of relevant land surface observations. Reconciling models with observations will likely require a new way to characterize the land surface feedback on SAT, one that doesn't rely on specialized experiments or land surface properties that are difficult to measure. The logical basis for a land surface feedback metric is SAT variability, as demonstrated in GLACE (Koster et al., 2004b), but characterizing the "land surface driven" portion of SAT variability is difficult because SAT variability depends also on atmospheric circulation patterns (Wallace et al., 1995; Branstator and Teng, 2017). The influence of atmospheric circulation on SAT must be accounted for in order to determine the influence of the land surface.

A way to account for the influence of atmospheric circulation on SAT is through dynamical adjustment. Traditionally, dynamical adjustment methods have been developed to identify and remove the contribution of atmospheric circulation from SAT trends (**?**Wallace et al., 2012; Smoliak et al., 2015; Saffioti et al., 2017). However, the method developed by Deser et al. (2016) (henceforth, "dynamical adjustment"), can also be used to characterize the influence of atmospheric circulation on interannual SAT variability. Dynamical adjustment leverages the relationship between circulation and SAT (Lorenz, 1969) to empirically characterize the SAT pattern associated with the large-scale atmospheric circulation present in a given month. Removing this "dynamic" component of SAT leaves behind SAT anomalies that are likely related to thermodynamic processes, such as the land surface feedback in the summer. Chapters 3

and 4 of this dissertation focuses on whether dynamical adjustment can be used to define a land-atmospheric hot spot metric based solely on SAT and an indicator of circulation, such as geopotential height or sea level pressure (SLP).

During extreme heat wave events, the influence of the land surface on SAT can extend beyond interannual land-atmosphere hot spots. A region where this has been shown to occur is continental Europe (Fischer et al., 2007a; Lorenz et al., 2010; Vogel et al., 2017). Europe is situated in the vicinity of the polar jet stream and susceptible to persistent blocking events that cause heat waves (Egger, 1978; Perkins, 2015). As the climate system warms, these blocking-induced heat waves may become more frequent, intense, and persistent (e.g Schär and Jendritzky, 2004; Meehl and Tebaldi, 2004; Beniston et al., 2007).

Soil conditions amplify or damp heat wave SAT. Beneath a blocking high, heat builds and evaporative demand increases throughout the day as large-scale horizontal advection and enhanced entrainment bring warm air to the boundary layer. The heat then remains beneath the nocturnal boundary layer and accumulates, causing soils to dry further (Miralles et al., 2014). By this mechanism, dry initial soil conditions increase the risk of dangerously extreme heat; with no water to evaporate, the sensible heat flux exacerbates the event. Using an initial condition ensemble of summers with the same heat wave circulation pattern and different initial land surface states, we assess to what extent preseason soil moisture conditions exacerbate an exceptionally hot European summer in Chapter 5.

Chapter 2

Summer U.S. Surface Air Temperature Variability: Controlling Factors and AMIP Simulation Biases

Summer U.S. Surface Air Temperature Variability: Controlling Factors and AMIP Simulation Biases

ANNA L. MERRIFIELD AND SHANG-PING XIE

Scripps Institution of Oceanography, University of California, San Diego, La Jolla, California

(Manuscript received 30 September 2015, in final form 4 April 2016)

ABSTRACT

This study documents and investigates biases in simulating summer surface air temperature (SAT) variability over the continental United States in the Atmospheric Model Intercomparison Project (AMIP) experiment from phase 5 of the Coupled Model Intercomparison Project (CMIP5). Empirical orthogonal function (EOF) and multivariate regression analyses are used to assess the relative importance of circulation and the land surface feedback at setting summer SAT over a 30-yr period (1979–2008). Regions of high SAT variability are closely associated with midtropospheric highs, subsidence, and radiative heating accompanying clear-sky conditions. The land surface exerts a spatially variable influence on SAT through the sensible heat flux and is a second-order effect in the high-variability centers of action (COAs) in observational estimates. The majority of the AMIP models feature high SAT variability over the central United States, displaced south and/or west of observed COAs. SAT COAs in models tend to be concomitant and strongly coupled with regions of high sensible heat flux variability, suggesting that excessive land–atmosphere interaction in these models modulates U.S. summer SAT. In the central United States, models with climatological warm biases also feature less evapotranspiration than ERA-Interim but reasonably reproduce observed SAT variability in the region. Models that overestimate SAT variability tend to reproduce ERA-Interim SAT and evapotranspiration climatology. In light of potential model biases, this analysis calls for careful evaluation of the land–atmosphere interaction hot spot region identified in the central United States. Additionally, tropical sea surface temperatures play a role in forcing the leading EOF mode for summer SAT in models. This relationship is not apparent in observations.

1. Introduction

There are many socioeconomic consequences of exceptionally warm summers in the continental United States. Extreme summer temperatures can cause hundreds of millions of dollars in crop damage (NOAA/NWS 2015) and strain water resources in drought-prone regions like the Southwest. In recent years, excessive heat has become the number-one weather-related killer, surpassing hurricanes, floods, tornadoes, and lightning strikes (Thacker et al. 2008). Around 500 heat-related deaths occurred in a one-week period during the 1995 Chicago heat wave (Whitman et al. 1997). Accurate forecasts of U.S. summer surface air temperature (SAT) will become more crucial as the climate system warms; it is anticipated that North American heat waves will become more intense, occur more frequently, and persist longer in duration in the second half of the twenty-first century (Meehl and Tebaldi 2004; Ganguly et al. 2009).

General circulation models (GCMs) must be shown to simulate the current mean state and variability of summer SAT to bolster confidence in future projections of summer climate, as processes governing SAT operate in response to increased CO_2 (Xie et al. 2015). SAT climatology is determined by the distribution of solar insolation and orography. Interannual variations in SAT about the mean state are driven by atmospheric circulation and are much more challenging to simulate spatially than global mean SAT. Because the atmosphere loses memory of its initial state on subseasonal time scales, models must rely on the slowly varying states of the ocean and land surface for predictive skill (Koster et al. 2006). Even if the model atmosphere responds perfectly to forcings at the surface, near-term (from annual to decadal) predictive skill is diminished by internal variability, which is intrinsic to chaotic systems and inherently unpredictable because of its random

Corresponding author address: Anna L. Merrifield, Scripps Institution of Oceanography, University of California, San Diego, 9500 Gilman Dr., MC 0206, La Jolla, CA 92093.
E-mail: almerrif@ucsd.edu

DOI: 10.1175/JCLI-D-15-0705.1

temporal phase (Deser et al. 2012). Further uncertainty arises from computational limitations that require simplified numerical formulations and parameterizations of subgrid-scale physical processes.

Despite the complexity of the climate system and the practical limits of models, atmospheric GCMs forced with observed sea surface temperatures (SSTs) are generally skillful at capturing both the mean state and variability of winter SAT over the continental United States (Sheffield et al. 2013; Deser et al. 2014). In the winter [December–February (DJF)], tropical forcings are strong. SST anomalies associated with El Niño–Southern Oscillation (ENSO) peak and exert influence on the extratropical atmosphere through eddy-driven changes in mean meridional circulation and stationary planetary waves in the Pacific–North American (PNA) sector (Seager et al. 2003; Kushnir et al. 2010; Zhou et al. 2014). The distribution of solar radiation in winter sets up a strong meridional temperature gradient in the Northern Hemisphere. In the free troposphere, the meridional temperature gradient sustains tropical–extratropical teleconnections by maintaining the zonal jet stream. At the surface, atmospheric circulation anomalies dictate SAT patterns by advecting air parcels across these gradients. The predictability of U.S. winter SAT is enhanced because of the SST-forced component of atmospheric variability.

In contrast during the summer [June–August (JJA)], U.S. SAT variability is, to first order, the product of internal variability in the midlatitude atmosphere (Wallace et al. 1995, 2015). The strong temperature gradient that maintains the zonal structure of the westerly jet in the winter weakens in the summer. Meanders in the upper-tropospheric flow create high pressure systems that can persist for weeks in the free troposphere (Charney and DeVore 1979; Egger 1978). Subsiding air beneath these blocking anticyclones warms adiabatically and is accompanied by clear skies and light winds, which are conditions conducive to summer warming (Meehl and Tebaldi 2004; Lau and Nath 2012). At the surface, the semipermanent Pacific and Bermuda highs direct northwesterly flow into the Pacific Northwest and southeasterly flow over the eastern seaboard. The circulation reaching the continental interior also is anticyclonic in structure, with a southerly jet along the Sierra Madre that brings moisture from the Gulf of Mexico to the Great Plains (Nigam and Ruiz-Barradas 2006). Thermal anticyclones also tend to form in July over cold polar regions, like the snow and ice fields of Canada, and propagate southeast over the continental United States (Zishka and Smith 1980). The primary North American anticyclone track lies over the Great Lakes and north-central United States (Davis et al. 1997).

Although tropical SST is not the dominant driver of U.S. summer SAT variability (Barlow et al. 2001), many studies have noted a connection between tropical SST forcing regions on the midlatitude summer atmosphere (e.g., Shaw and Voigt 2015; Arblaster and Alexander 2012; Pegion and Kumar 2010; Schubert et al. 2009; Lau et al. 2006; Sutton and Hodson 2005; McCabe et al. 2004; Higgins et al. 2000). Protracted La Niña events have been associated with persistent droughts, notably the large-scale midlatitude drying between 1998 and 2002 (Hoerling and Kumar 2003), the Texas drought and heatwave of 2011 (Hoerling et al. 2013), and the Dust Bowl of the 1930s (Schubert et al. 2004; Seager et al. 2005). Some studies (Ding and Wang 2005; Ding et al. 2011) suggest that model skill derives from the predictable zonal mean component of the circumglobal teleconnection. Wang and Ting (1999) and Ting (1994) showed that nonlinear interactions among monsoonal heating-induced flows link U.S. summer climate to convective regions near Asia in the NCEP–NCAR reanalyses and GCMs. Kushnir et al. (2010) showed that warm SSTs in the tropical North Atlantic can exert an ''upstream'' control on SAT by weakening the subtropical North Atlantic anticyclone, driving northerly cold advection and anomalous subsidence over North America. SSTs associated with decadal modes of variability, such as the Atlantic multidecadal oscillation (AMO) and Pacific decadal oscillation (PDO), can influence U.S. summer SAT by modulating the Great Plains low-level jet, which brings warm, moist air from the Gulf of Mexico to the central United States (Weaver 2013).

Land surface conditions can also affect summer SAT variability (Seneviratne et al. 2006; Lorenz et al. 2010), in not too wet (energy limited) and not too dry (moisture limited) soil moisture (SM) ''hot spot'' regions like the central United States (Koster et al. 2004a,b, 2006; Dirmeyer 2011; Berg et al. 2014). To describe relationships between the atmosphere and the land surface, we use ''interaction'' to refer to a general association between two variables, ''coupling'' to refer to the degree one variable controls another, and ''feedback'' to refer to a two-way coupling, following Lorenz et al. (2015). For example, soil moisture–climate coupling refers to the soil moisture control on SAT variability through the sensible heat flux. Zhang et al. (2008) investigated the role of the land–atmosphere coupling on U.S. summer climate variability using regional climate models and found that the strong coupling between soil moisture and daily mean temperature contributed 30%–60% of the total interannual SAT variance in the southwestern, north-central, and southeastern United States.

Land–atmosphere interactions occur primarily through the surface energy balance. Terrestrial water acts to

partition outgoing energy into latent heat flux at the expense of sensible heat flux Q_H, resulting in cooler SAT (Seneviratne et al. 2010). When atmospheric conditions are stable under anticyclones, the positive feedback between the land and atmosphere allows the sensible heat flux to enhance warm temperatures and increase SAT variability. Warm, dry conditions come with a high atmospheric demand for water, reducing soil moisture. Without water to evaporate, more outgoing energy is available to heat the atmosphere (Seneviratne et al. 2010; Miralles et al. 2012). Soil desiccation has been shown to contribute to mega-heat waves in Europe (Fischer et al. 2007a,b; Miralles et al. 2014), but fewer studies have assessed the impact of the land surface on severe temperature extremes in the United States (Diffenbaugh et al. 2005). Assessments of North American hydroclimate variability suggest that land–atmosphere interactions are overemphasized in models during the warm season and report that local evaporation in the central United States can be up to 4 times larger in models than in observationally constrained estimates (Ruiz-Barradas and Nigam 2005; Wu and Dickinson 2005; Ruiz-Barradas and Nigam 2006, 2013). Mueller and Seneviratne (2014) also document land hydrological and climate biases and highlight the overestimation (underestimation) of temperature (evaporation) in central U.S. climatology in CMIP5 simulations. Quantification of land surface coupling during the warm season is cited as a high research priority (Perkins 2015), and the land surface is thought to be key in improving model forecasts of SAT on seasonal time scales (Koster et al. 2011).

While the circulation and land surface controls on summer SAT variability are generally recognized, gaps exist in quantifying the relative importance of the involved physical mechanisms (Perkins 2015) and in systematically evaluating summer variability in climate models. Models are important for prediction, projection, and attribution, but careful investigation and documentation of their skills and errors are required before their output can be used with confidence. The present study evaluates the performance of atmospheric models in simulating summer SAT variability over the continental United States; this is one of few such CMIP5 assessments to our knowledge. Evaluations of model SAT benefit from the excellent accuracy and coverage of U.S. SAT measurements, which constrain gridded products from atmospheric reanalyses. In addition, summer SAT is strongly affected by land–atmosphere interactions, which in turn can be evaluated using SAT. To document model skill, we present maps of U.S. summer SAT variability and contrast them with their winter, higher-skill counterparts. In summer, the regions of high SAT variance differ spatially between observations and models, a discrepancy that we suggest is due to an excessively strong central U.S. land–atmosphere interaction in models. To evaluate this hypothesis, we assess the relative importance of circulation and the land surface at setting summer SAT and examine the effects of the SST-forced and internal components of variability in the midlatitude summer atmosphere. This study assesses the nature and sources of U.S. summer SAT variability in the AMIP experiment, with the aim of validating its predictive capability.

We organize the remaining sections as follows. The observational datasets, model experiments, and methods are described briefly in section 2. Observational and model estimates of U.S. summer SAT climatology and variability are documented in section 3, and model skill is contrasted between summer and winter. In section 4, the relative importance of circulation and the land surface on observed and simulated JJA SAT variability is evaluated. The land surface's role in climatological SAT model biases is also assessed. Other potential causes for model biases are explored in section 5, including differences in SST forcing regions and the lead–lag response to ENSO variability. A summary of findings and discussion of the complexities of the land–atmosphere interaction are given in section 6.

2. Observational estimates, simulations, and methods

a. Observational estimates

We use the European Centre for Medium-Range Weather Forecasts (ECMWF) interim reanalysis (ERA-Interim) for monthly mean SAT, 500-hPa geopotential height Z_{500}, and surface fluxes (Dee et al. 2011) on a 1.5° latitude × 1.5° longitude grid from 1979 to 2008. For verification, we use NCEP North American Regional Reanalysis (NARR; Mesinger et al. 2006). Spatial patterns of variability are similar for the reanalysis products, so for conciseness we present maps based on the ERA-Interim fields. (Relationships between SAT, Z_{500}, and the land surface in Figs. 5 and 6, described in greater detail below, are presented for both ERA-Interim and NARR.)

ERA-Interim 30-yr JJA SAT, Z_{500}, Q_H climatology, and regions of the United States used to describe the spatial structure of the considered fields are shown in Fig. 1. For clarity, we will refer to ERA-Interim SAT and Z_{500} as observed because the fields are well measured and thus well constrained in reanalysis products. However, it is important to acknowledge shortcomings in reanalysis surface flux estimates. By design, water and energy budgets are not closed in reanalysis products, and surface flux observations are spatially sparse and

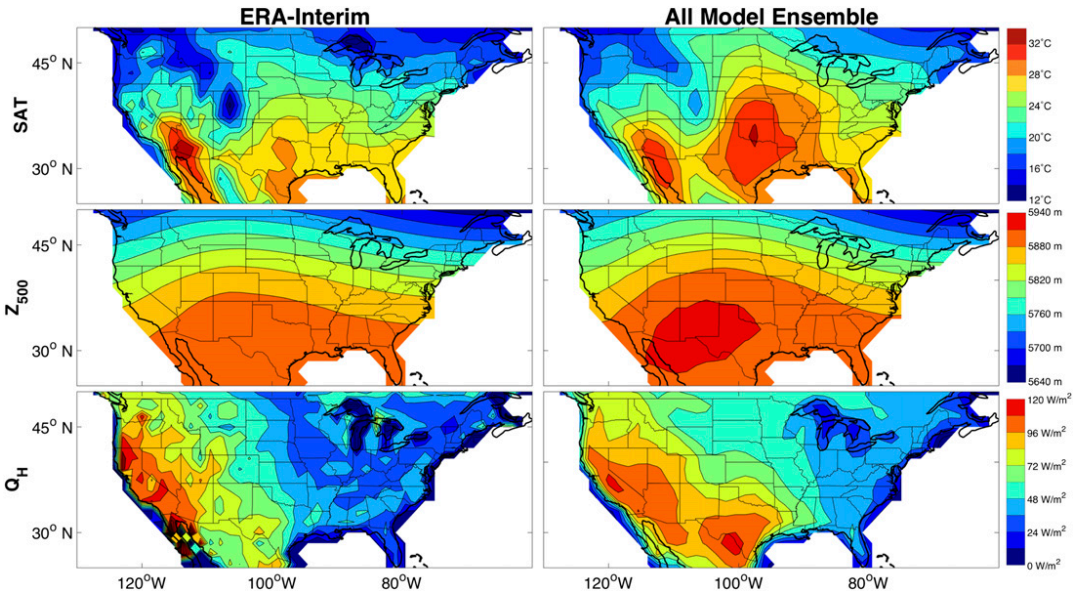

FIG. 1. The 30-yr climatology (1979–2008) of (top) SAT, (middle) Z_{500}, and (bottom) Q_H for (left) ERA-Interim and (right) the all-model ensemble.

temporally limited. Because surface fluxes are not well constrained, studies recommend exercising great caution when using them (e.g., Trenberth et al. 2011; Ferguson et al. 2012). For this reason, we will consider interannual variations and spatial patterns of ERA-Interim surface flux estimates in this assessment but not base any conclusions on the magnitude of the fluxes themselves.

b. AMIP experiments

For comparison with reanalysis fields, we use monthly mean SAT, Z_{500}, and surface fluxes from 14 models in the CMIP5 AMIP experiment (Taylor et al. 2012). In each model, AMIP runs are initialized months prior to January 1979 with different atmospheric states to form initial condition ensembles with between 2 and 10 ensemble members. All 14 initial condition ensembles are combined to form an all-model ensemble with 58 members. In addition to time-evolving external forcings, the AMIP runs are forced by observed SST and sea ice states. Land surface states interact with the atmosphere and vary among modeling groups. Salient information about each model used is given in Table 1, with further details given in Table 9.A.1 of the Intergovernmental Panel on Climate Change (IPCC) Fifth Assessment Report (AR5; Flato et al. 2013). The CMIP5 all-model ensemble climatologies are shown in Fig. 1 (right). Models vary in their ability to capture observed SAT climatology over the continental United States, and many feature warm biases in the central United States. We will consider model climatological biases as we assess model performance in depicting SAT variability.

c. Methods

SAT variability is characterized as the standard deviation in seasonally averaged, ocean-masked SAT fields within 24°–52°N and 45°–145°W. Winter averages are formed over DJF and summer averages over JJA. For the AMIP ensembles, the interannual variance of the 30-yr record (1979–2008) is computed for each member, then averaged over the ensemble and square rooted to avoid suppressing the internal component of variability. To emphasize spatial variability, the standard deviations depicted in Figs. 2 and 3 are scaled by their domain-average standard deviations, which are reported in the lower right corner of each panel. Model fields are plotted on their native grids in Figs. 2 and 3 and are regridded to the reanalysis grid (1.5° × 1.5°) for the remaining figures.

Empirical orthogonal function (EOF) analysis is used to describe dominant modes of JJA SAT variability. EOFs are computed after removing a mean and linear trend from the JJA SAT time series and applying a square root cosine latitude spatial weighting. Each EOF spatial mode has an associated temporal coefficient, or principal component (PC). For the AMIP ensembles, an EOF analysis is performed on both 1) the ensemble mean and 2) the concatenated n by 30-yr record of the JJA averaged fields, where n is the number of member runs for each model. Averaging across ensemble members suppresses the internal variability present in each individual realization, emphasizing the model's response to external forcing (Deser et al. 2015). Concatenating realizations preserves both the forced and internal components that comprise the observed variability.

TABLE 1. Salient information about the CMIP5 AMIP experiments used. The values in parentheses under the gridpoint resolution column are the spectral truncation of the model resolution. (Expansions of acronyms are available online at http://www.ametsoc.org/PubsAcronymList.)

Model acronym	Abbreviation	Institute	Members	Gridpoint resolution (lat × lon)	Citation
All-model ensemble	All		58	121 × 240	
BCC_CSM1.1(m)	BCC	Beijing Climate Center	3	160 × 320 (T106)	Wu et al. (2014)
CanAM4	CAN	Canadian Centre for Climate Modelling and Analysis	4	64 × 128 (T42)	Arora et al. (2011)
CMCC-CM	CMCC	Centro Euro-Mediterraneo per I Cambiamenti Climatici	3	240 × 480	Scoccimarro et al. (2011)
CSIRO Mk3.6.0	CSIRO	Commonwealth Scientific and Industrial Research Organisation in collaboration with the Queensland Climate Change Centre of Excellence	10	96 × 192 (T63)	Rotstayn et al. (2012)
GFDL CM3	GFDL	Geophysical Fluid Dynamics Laboratory	5	90 × 144	Donner et al. (2011)
GISS-E2-R	GISS	NASA Goddard Institute for Space Studies	6	90 × 144	Kim et al. (2012)
IPSL-CM5A-LR	IPSL	L'Institut Pierre-Simon Laplace	5	96 × 96	Dufresne et al. (2013)
FGOALS-s2	LASG	LASG, Institute of Atmospheric Physics, Chinese Academy of Science	3	108 × 128	Bao et al. (2013)
MIROC5	MIROC	Atmosphere and Ocean Research Institute (The University of Tokyo), National Institute for Environmental Studies	2	128 × 256 (T85)	Watanabe et al. (2010)
HadGEM2-A	MOHC	Met Office Hadley Centre	3	145 × 192	Collins et al. (2011)
MPI-ESM-MR	MPI	Max Planck Institute for Meteorology	3	96 × 192 (T63)	Giorgetta et al. (2012)
MRI-CGCM3	MRI	Meteorological Research Institute	3	160 × 320 (T106)	Yukimoto et al. (2012)
CCSM4	NCAR	National Center for Atmospheric Research	5	192 × 288	Gent et al. (2011)
NorESM1-M	NCC	Norwegian Climate Centre	3	96 × 144	Bentsen et al. (2013)

Correlations of the leading JJA SAT principal component (PC1) with Z_{500} and Q_H are computed for each grid point. This method highlights regions of temporal covariability between SAT and potential dynamic (circulation) and thermodynamic (surface flux) controls. The 95% significance is determined by assuming a Student's t distribution with $N - 2$ degrees of freedom, where N is the number of years in the record. When anomalies are spatially similar, temporally coincident, and physically consistent, we infer relationships between fields.

A local multivariate regression analysis and calculation of the soil moisture–climate coupling proposed by Dirmeyer (2011), Dirmeyer et al. (2013a,b), and Dirmeyer et al. (2014) are used to further examine relationships between JJA SAT, Z_{500}, and Q_H. JJA SAT, Z_{500}, and Q_H are averaged in boxed regions within the SAT centers of action (COAs), and the resulting time series are normalized by their standard deviations. We interpret the Z_{500} and Q_H regression coefficients b_Z and b_Q as indicators that SAT variability within the COA is associated with atmospheric circulation and local sensible heat flux, respectively.

The pathway for SM anomalies to influence the atmosphere in the COA is assessed through the Dirmeyer soil moisture–climate coupling metric $I_{\text{SM–SAT}}$ described in Lorenz et al. (2015):

$$I_{\text{SM–SAT}} = \sigma(\text{SAT})\rho(\text{SM}, Q_H)\rho(Q_H, \text{SAT}). \quad (1)$$

The metric $I_{\text{SM–SAT}}$ accounts for the terrestrial segment (SM–Q_H) and atmospheric segment (Q_H–SAT) of the land surface feedback through correlations ρ and is suppressed in regions of low SAT variability by σ(SAT) (Dirmeyer 2011; Dirmeyer et al. 2013a,b, 2014). We evaluate the

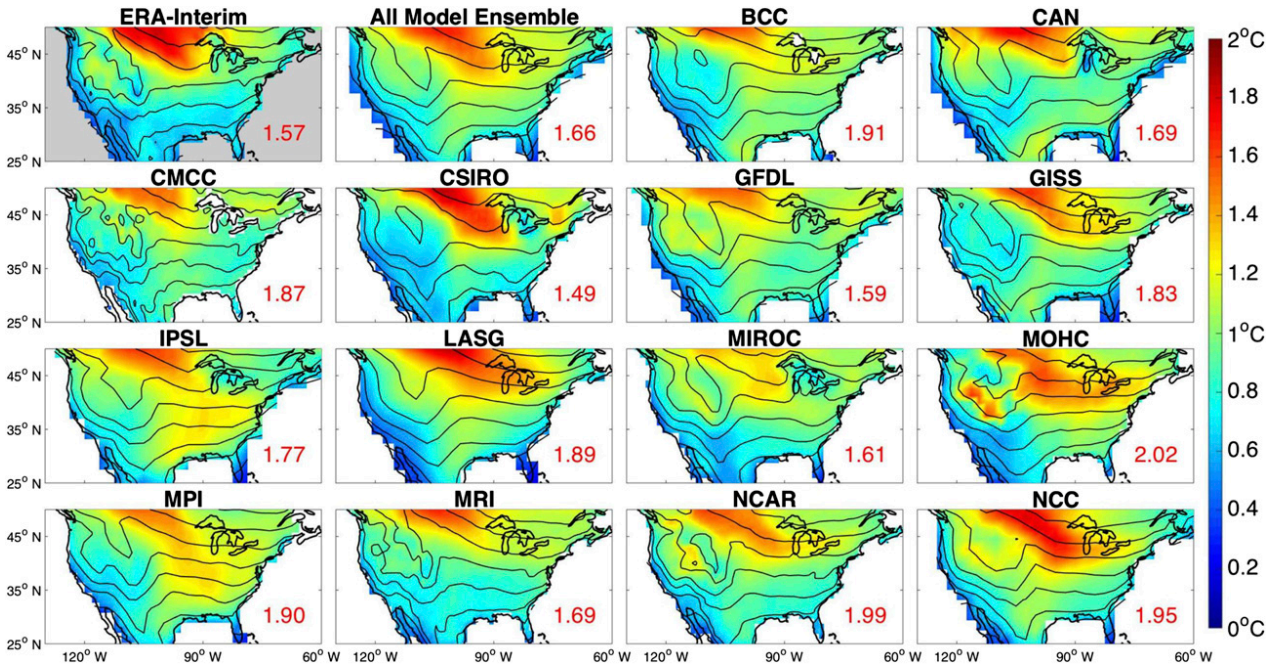

FIG. 2. DJF SAT standard deviation maps (color) for 1979–2008. The observed variability is presented in the panel labeled "ERA-Interim." Each map contains the mean SAT (°C; black contours ranging from −15° to 15°C with an interval of 5°C). Maps are scaled by the domain-average standard deviation (given in red in the lower right corner). Models reproduce the spatial structure of DJF SAT variability, which is largest in the north-central United States.

relationship between mean SAT and mean evapotranspiration with a second soil moisture–temperature coupling estimate proposed by Seneviratne et al. (2006), ρ(evapotranspiration, SAT), which gives insight into climatological biases in the central United States. Finally, we consider the role of the global ocean through remote atmospheric pathways on U.S. summer SAT by regressing SSTs and 300-hPa heights Z_{300} on JJA SAT PC1.

3. SAT variability—DJF versus JJA

In boreal winter, the jet stream is strong and tropical SST anomalies peak, providing the foundation for teleconnections such as the PNA pattern to influence U.S. SAT. Standard deviation maps (Fig. 2) illustrate how the various models depict spatial patterns of winter SAT variability. The 30-yr DJF SAT climatology is shown in black contours, with values ranging from −15° to 15°C in 5°C increments. Both observed and modeled winter SAT climatologies have a zonal-banded structure, with the exception of lower temperatures at high altitude over the Rocky Mountains. From year to year, winter temperatures fluctuate most[1] by up to 2.9°C in a region that extends down from western Canada over the north-central United States. Because advection of the mean SAT gradient by anomalous circulation dominates over other mechanisms (Thompson and Wallace 2000), this feature is captured in most AMIP models and the spatial structure of DJF SAT variability is well represented in CMIP5. The magnitude of DJF SAT variability in the domain tends to be higher in models than in observations, which is due to higher values of variability in the southeastern and south-central United States. Models with more members, such as CSIRO Mk3.6.0, have higher skill in reproducing observed variability, illustrating the power of larger ensembles to represent realistic internal variability in the presence of model error (Kay et al. 2015).

Model simulations of SAT variability over the continental United States are less similar to observational estimates in the summer than they are in the winter (Fig. 3). In the summer, observed climatological temperatures range from about 10°C over the Rocky Mountains to 35°C in the Mojave and Sonoran Desert regions of the Southwest. Aside from these regions, the observed JJA SAT climatology also has a zonal structure. A major discrepancy between observed and modeled JJA SAT climatology is a meridional warm bias spanning the central United States, which occurs in 9 of the 14 models and in the all-model ensemble [Fig. 1 (top right) and

[1] While the maps in Figs. 2 and 3 are scaled by their domain-averaged σ, values of variability reported in section 3 are unscaled.

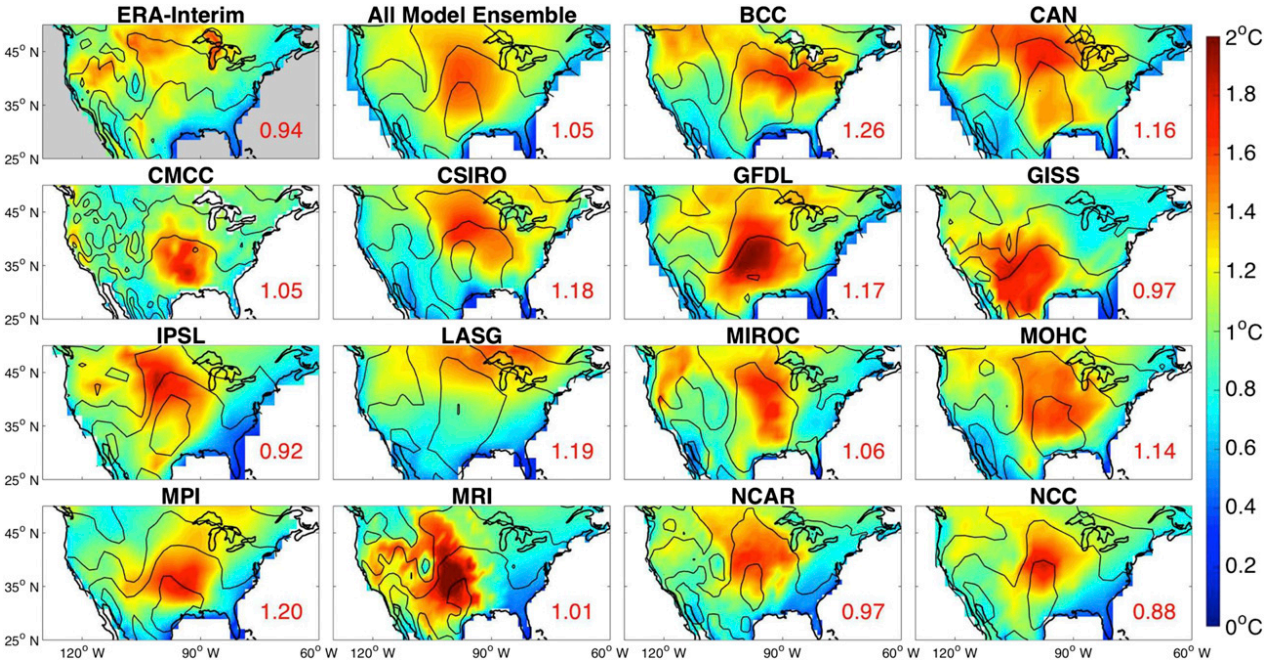

FIG. 3. As in Fig. 2, but for JJA SAT. Models show a discrepancy in the position and strength of high-variability COAs in JJA SAT. Model COAs tend to occur over the south-central United States, a region that also features a climatological warm bias in many models (°C; black contours ranging from 15° to 35°C with an interval of 5°C).

Fig. 3]. Causes of this warm bias are investigated in section 4.

Interannual variations in SAT are less localized and less pronounced in summer than in winter. ERA-Interim JJA temperatures vary by 1°–1.2°C over much of the United States, with lower variability (~0.5°C) along the southeastern seaboard due to the thermal inertia of the Gulf Stream. The largest JJA SAT variability (1.6°C) occurs in the southern northwest Great Basin cold desert and north-central Great Plains, on either side of the Rocky Mountain range. This pattern of summer SAT variability is poorly simulated in most of the AMIP models, which tend to feature regions of high variability in the central United States. Most models feature either a large swath of variability over the north-central United States [e.g., BCC_CSM1.1(m), CSIRO Mk3.6.0, and CCSM4] or a highly localized COA in the south-central United States (e.g., CMCC-CM, GISS-E2-R, and MRI-CGCM3). In MRI-CGCM3, SAT variability over Kansas and the Oklahoma Panhandle exceeds 2.1°C, doubling observed values in the region.

Models with JJA SAT COAs in the south-central United States tend to have SAT climatologies that are similar to observed. Models with JJA SAT COAs in the north-central United States have pronounced warm biases in the south-central United States. We conjecture that model skill in simulating U.S. summer SAT will improve if the causes of the warm bias and spurious variability in the central United States are identified and managed.

4. Relative importance of circulation versus land–atmosphere coupling

We examine summer SAT interannual variability in the AMIP models by considering the leading EOF mode (EOF1; Figs. 4a,d). The associated time series (PC1) is correlated with JJA Z_{500} (Figs. 4b,e) and Q_H (Figs. 4c,f) time series at each grid point. This method is used to demonstrate association between SAT and the main physical processes that are expected to contribute to its variability and to identify the relative importance of these contributions in the central U.S. model COAs. We focus on EOF1 because it features a dominant COA centered in the north-central United States and captures a sizable percentage (38%) of the domain-integrated, normalized variance in the 30-yr reanalysis record. Model EOF1s feature the regions of high SAT variability (Fig. 3) that we are interested in evaluating. The boxed region (9° × 15°) in each panel corresponds to the region of highest SAT variability in each EOF1.

In the observed COA, SAT interannual variability correlates highly with Z_{500}, indicating the importance of midtropospheric highs in establishing warm SATs in this region (Meehl and Tebaldi 2004; Lau and Nath 2012). ERA-Interim Q_H and SAT are marginally correlated in

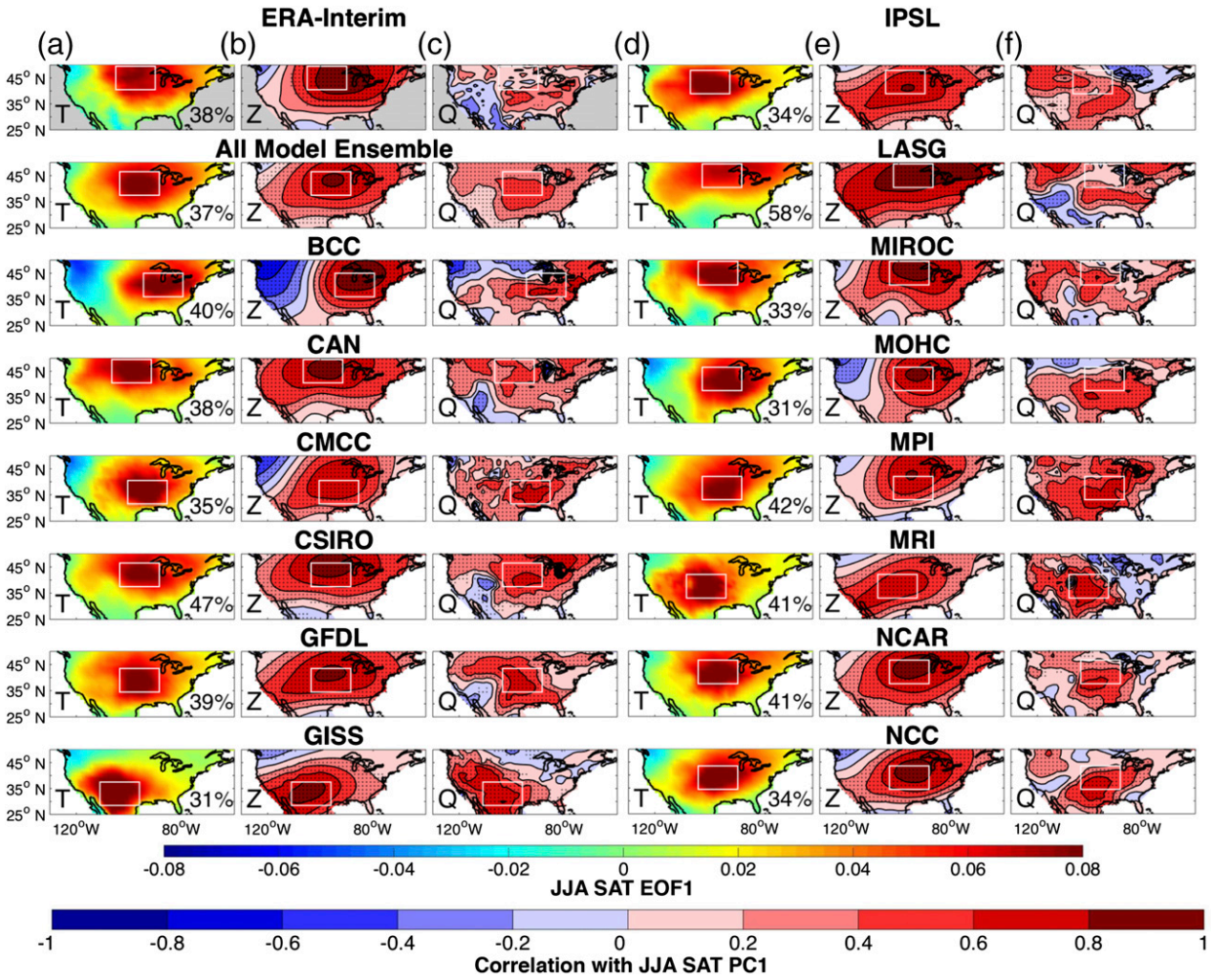

FIG. 4. (a),(d) JJA SAT EOF1 and correlations between PC1 and (b),(e) Z_{500} and (c),(f) Q_H. Percent of normalized variance explained by SAT EOF1 is given in the lower right of (a),(d). Boxes show the location of high-variability SAT COA regions that will be used for a local regression analysis.

the COA, positively correlated in the southeastern and south-central United States, and negatively correlated in the Southwest. ERA-Interim correlations that exceed ± 0.36 are different than zero at the 95% significance level and are stippled in Fig. 5. Significant positive SAT–Q_H correlations in the eastern United States indicate a prominent land surface feedback, with warm SATs in the region amplified by soil desiccation (Findell and Eltahir 2003). Correlations in the southwestern portion of the United States fall below the 95% significance threshold likely because the region is moisture limited (Seneviratne et al. 2010) so surface fluxes are rarely large enough to influence SAT variability.

In the AMIP experiment, all but two models have JJA SAT EOF1s that resemble the observed north-central U.S. COA pattern. However, model COAs tend to extend either farther west (CanAM4, CSIRO Mk3.6.0, MIROC5, and IPSL-CM5A-LR) or south (CMCC-CM, GFDL CM3, MPI-ESM-MR, and NorESM1-M) than observed. The two model exceptions have COAs in the Southwest (GISS-E2-R) and south-central United States (MRI-CGCM3), similar to their respective variability patterns in Fig. 3. As in observations, models tend to capture the relationship between surface temperature and midtropospheric circulation, with high SAT–Z_{500} correlations in the COAs. However, the highest model SAT–Z_{500} correlations are not centered within the boxed region of highest SAT variability in all cases (e.g., CMCC-CM, HadGEM-A, and NorESM1-M).

A notable difference between the models and ERA-Interim is the high model SAT–Q_H correlations found within the COA regions (boxed regions in Figs. 4c,f). Moreover, the general shape and position of the COA closely resemble the Q_H projection. In contrast,

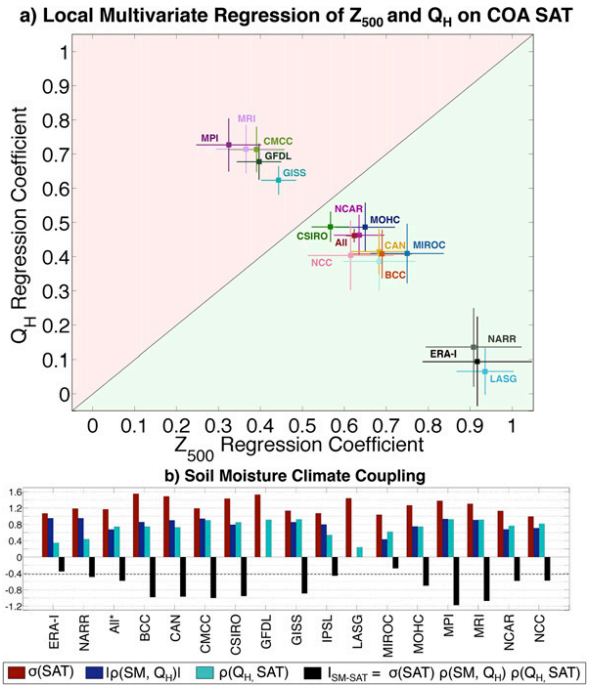

FIG. 5. (a) A comparison of Z_{500} and Q_H multivariate regression coefficients (b_Z and b_Q), with 95% confidence intervals, and (b) the Dirmeyer soil moisture–climate coupling metric and its constituents calculated in the boxed averaged region within the COA. If b_Z exceeds b_Q, as it does in observations (ERA-Interim in black and NARR in gray), variability in the SAT COA is more closely associated with atmospheric circulation patterns (green region). If b_Q exceeds b_Z, variability in the SAT COA is more closely associated with variations in the local sensible heat flux (red region). In (b), the red bars are the box-averaged standard deviation of SAT, blue bars are the magnitude of the soil moisture–Q_H correlation (which is negative), and teal bars are the Q_H–SAT correlation. All but one model I_{SM-SAT} (black bars) exceed the average observed I_{SM-SAT} (−0.42, dashed line).

ERA-Interim shows weak SAT–Q_H correlations in the north-central U.S. COA. We interpret the high SAT–Q_H model correlations as an indication that spurious SAT variability in the AMIP models may be due to Q_H fluctuations contributing an unrealistically high land–atmosphere coupling compared to observational estimates.

To examine further the relationships between JJA SAT and Z_{500} and Q_H, we apply a multivariate regression analysis within SAT COAs. Each variable is spatially averaged within the boxed regions indicated in Fig. 4 and normalized by the standard deviation. We regress SAT onto Z_{500} and Q_H to obtain regression coefficients b_Z and b_Q, respectively, with confidence intervals computed assuming serially independent time series. If b_Z exceeds b_Q, we categorize variability in the SAT COA as more closely associated with atmospheric circulation patterns than with the land surface (green region in Fig. 5a). In ERA-Interim, b_Z (0.92) exceeds b_Q (0.09), demonstrating a clear association between atmospheric circulation and SAT variability in the COA. A similar relationship is found in NARR, with $b_Z = 0.91$ and $b_Q = 0.14$. Only one model, FGOALS-s2, has similarly attributed COA SAT variability, with $b_Z = 0.93$ and $b_Q = 0.07$. The majority of models fall within the circulation-associated regime with less separation than ERA-Interim between the Z_{500} and Q_H regression coefficients; in the all-model ensemble, $b_Z = 0.62$ and $b_Q = 0.46$.

If b_Q exceeds b_Z, variability in the SAT COA is categorized as more closely associated with variations in the local sensible heat flux than with circulation (red region of Fig. 5a). AMIP models with shifts in the position of the COA relative to observed, such as GISS-E2-R, fall within the surface-flux-dominated regime. Models with striking regions of high SAT variability in the central United States (CMCC-CM, MPI-ESM-MR, and MRI-CGCM3) have a large discrepancy in SAT control attribution with their average b_Q (0.72) doubling their b_Z (0.36).

To accompany the regression analysis, the Dirmeyer soil moisture–climate coupling metric [Eq. (1)] and its constituents for the box-averaged regions within the COAs are shown in Fig. 5b. The metric comprises the correlations between soil moisture and sensible heat flux (the terrestrial segment, blue bar) and between sensible heat flux and SAT (the atmospheric segment, cyan bar), which are weighted by the standard deviation of SAT (red bar). For the CMIP5 models, we use total soil moisture content because it is an output provided by all but two modeling centers (GFDL and LASG). Root zone (~0–70 cm) soil moisture is likely more suitable for this analysis, but Dirmeyer (2011) showed that although total column soil moisture–based metric values are muted with respect to surface soil moisture–based values, their spatial patterns are consistent.

Most models and the all-model ensemble show values of I_{SM-SAT} that exceed both ERA-Interim (−0.35) and NARR (−0.44) values (average dashed in Fig. 5b), supporting the visual evidence of a strong relationship between the land and atmosphere in the COA. IPSL-CM5A-LR and MIROC5 have lower values of the soil moisture–climate coupling because of lower than average SAT variability combined with a weak terrestrial (MIROC5) or atmospheric (IPSL-CM5A-LR) coupling segment. Models with the largest I_{SM-SAT} are surface-flux-dominated models, MPI-ESM-MR (−1.18), MRI-CGCM3 (−1.07), and CMCC-CM (−1.00). In the same regions, ERA-Interim and NARR I_{SM-SAT} do not exceed −0.49 (not shown). These regions of strong land–atmosphere coupling in the surface-flux-dominated models roughly coincide with the land–atmosphere interaction hot spot region defined in other studies (e.g.,

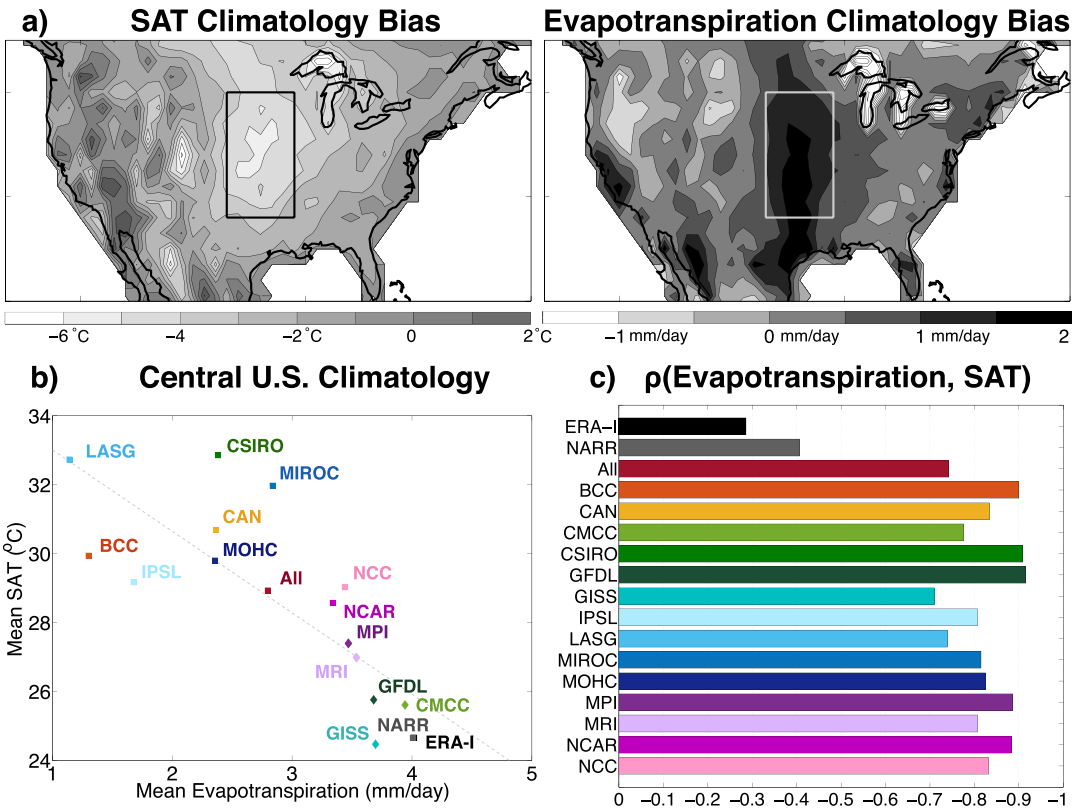

FIG. 6. (a) ERA-Interim–all-model ensemble (left) SAT and (right) evapotranspiration showing the climatological warm and dry bias in the central United States (boxed region; 33°–45°N, 92°–101°W). (b) The average evapotranspiration (mm day^{-1}) vs average SAT (°C) in the central United States showing a linear relationship in the central United States; less evapotranspiration leads to a climatological warm bias in models. Squares indicate models with circulation-associated SAT variability, and diamonds indicate models with surface-flux-associated SAT variability in the COA. (c) Correlations between box-averaged evapotranspiration and SAT give an estimate of land–atmosphere coupling strength.

Ruiz-Barradas and Nigam 2005; Koster et al. 2004a,b). However, land–atmosphere interactions in these hot spot regions appear to be both excessive with respect to observational estimates and a main contributor to spurious model SAT variability in the central United States.

Biases in mean summer SAT also have been related to biases in evapotranspiration (Mueller and Seneviratne 2014). We evaluate the relationship between mean SAT and evapotranspiration (Fig. 6) and focus on 33°–45°N, 92°–101°W, a region of climatological warm bias in the central United States, where SAT in the all-model ensemble exceeds observed SAT by more than 5°C (Fig. 6a). The region coincides with the meridional strip of evapotranspiration bias, where ERA-Interim values exceed all-model ensemble values by more than 1.5 mm day^{-1}. Mean SAT in the region is plotted against mean evapotranspiration in Fig. 6b, and there is a statistically significant linear relationship between SAT and evapotranspiration. Higher (lower) evapotranspiration means less (more) energy is available to heat the atmosphere, so wetter (drier) models tend to be less warm (warmer) in the central United States.

Models with near observed mean SAT in the region are the same models that have excessive, land surface–linked SAT variability in the central United States (Fig. 6b, diamonds). In this case, the models have similar values of mean central U.S. evapotranspiration to ERA-Interim but larger interannual surface flux variations in the region, with standard deviations exceeding ERA-Interim by up to 0.45 mm day^{-1}. Models with a climatological warm bias in the central United States can be up to 8°C warmer than observed but have circulation-associated SAT variability in their COAs, similar to observed (Fig. 6b, squares). Because these models have lower mean values of evapotranspiration, fluctuations in soil moisture have less effect on the atmosphere.

The land–atmosphere coupling strength is estimated through the correlations between seasonal mean SAT and evapotranspiration, a relationship that has shown pattern agreement with more rigorous measures of land–atmosphere coupling obtained through performing

prescribed and freely varying soil moisture experiments (Koster et al. 2006; Seneviratne et al. 2006). Negative correlations suggest a soil moisture control on fluxes to the atmosphere and temperature, although correlations become less meaningful as the magnitude of evapotranspiration diminishes (Seneviratne et al. 2006). The central United States is considered a transition region, limited by the availability of neither moisture nor radiation (Seneviratne et al. 2010), so we feel that the evapotranspiration–temperature correlation gives insight into the land–atmosphere coupling in our region of interest. All models have high evapotranspiration–temperature correlations in the region, exceeding ERA-Interim (NARR) correlations by 0.55 (0.41) on average, which further indicates models have a more robust land–atmosphere coupling than has been observationally estimated.

In summary, local regression analysis supports the visual SAT–control relationships established in our EOF analysis. We find that the land surface plays a larger role in setting U.S. summer SAT variability in the AMIP experiment than in ERA-Interim. The land–atmosphere coupling is considerably stronger in models than in ERA-Interim, both in regions of high SAT variability and in regions of climatological warm biases. Models with high SAT variability in the south-central United States feature clear covariability between COA SAT and Q_H. Models with more realistic SAT variability in the central United States tend to have a climatological warm bias. We conclude that strong land–atmosphere interactions along with climatological surface flux biases are responsible for spurious U.S. summer SAT variability in the AMIP ensemble.

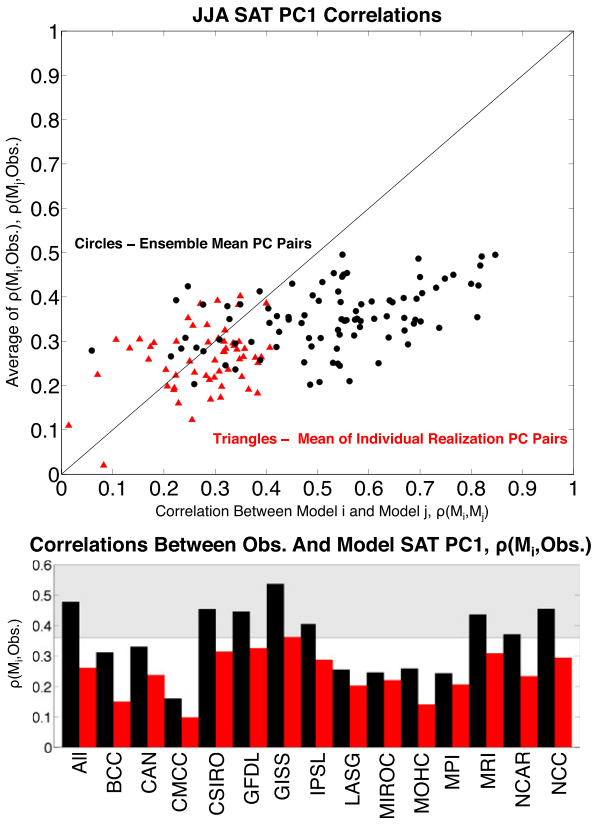

FIG. 7. (top) JJA SAT principal component correlations among model pairs (x axis) and average reanalysis–model pair correlation (y axis). Ensemble mean PC1s represent the forced component of variability (black circles) and individual realization PC1s represent the forced and internal components of variability (red triangles). (bottom) Correlations between modeled and observed JJA SAT PC1s, with the threshold for 95% significance indicated by the lower boundary of the gray shaded region.

5. SST forcing

While we attribute spurious U.S. summer SAT variability to an enhanced land surface feedback in the AMIP ensemble, other forcing biases can also contribute. SST variability in the equatorial Pacific, tropical Atlantic, and Indian Oceans can influence the midlatitude atmosphere and thus SAT variability over land. Regressing global SSTs onto JJA SAT PC1 illustrates potential SST forcing regions that impact common patterns of U.S. summer SAT. SSTs are prescribed over the 30-yr AMIP period, so biases arise from how the modeled atmosphere responds to slowly varying ocean states.

To evaluate model bias in SST forcing, correlations among SAT model PCs, defined as $\rho(M_i, M_j)$ for the correlation between model i and model j, are scattered against the average of the observed (obs)–model correlation pair $[\rho(M_i, \text{obs}) + \rho(M_j, \text{obs})]/2$ in Fig. 7. Because observed SAT variability includes an internal component as well as an SST-forced component, both ensemble mean PC pairs [black circles in Fig. 7 (top), forced component] and the average of individual realization PC pairs [red triangles in Fig. 7 (top), both forced and internal components] are considered. Correlations between observed and model PCs are all positive, which suggests a robust SST forcing. The black circles fall to the right of the one-to-one line, with correlations among ensemble mean PCs exceeding those between ensemble mean and observed PCs. This indicates that the models have similar, robust responses to the prescribed ocean forcing, despite having differences in physical and numerical formulations. Individual realization PCs correlate less strongly with observed than ensemble mean PCs (Fig. 7, bottom), and the scatter of red triangles around the one-to-one line is consistent with the effect of random internal variability. In the presence of internal variability, models are no more correlated with each other than they are with observations.

The bar graph in Fig. 7 (bottom) also shows which models share a forced component of summer SAT variability with ERA-Interim. Models in the AMIP experiment are forced with observed SSTs, so significant correlations between modeled and observed PCs arise from a common response to the shared boundary condition. For those models exhibiting significant correlations, we evaluate SST and circulation patterns associated with JJA SAT EOF1.

Potential regions of SST forcing (color) are highlighted in JJA SAT PC1–SST regression maps in Fig. 8. SSTs are regressed onto SAT PC1s, normalized by their standard deviation, to illustrate the variation (°C) in SST per standard deviation of SAT variability. Regions of the global ocean where SST correlates significantly (95%) with JJA (ensemble mean) SAT PC1 are stippled. SST influence can be felt over land through the atmosphere, so upper-tropospheric heights (i.e., Z_{300}), regressed on normalized JJA SAT PC1, are contoured to show the associated circulation patterns.

In ERA-Interim, sizable patches in the North Pacific, the tropical and North Atlantic, and the Caribbean Sea covary with the leading mode of JJA SAT. Correlations are notably not significant in the equatorial Pacific ENSO forcing region, emphasizing that there is not a substantial pathway for ENSO to influence the extratropical atmosphere over the United States in boreal summer (Barlow et al. 2001). Significant correlations in the Caribbean Sea illustrate the pathway for surrounding oceans to influence summer climate in the continental interior through the Great Plains low-level jet (Ruiz-Barradas and Nigam 2006; Weaver 2013). The wavy structure of observed Z_{300} anomalies in the Northern Hemisphere midlatitudes is characteristic of spatially organized internal variability. Significant correlations between JJA SAT PC1 and midlatitude Atlantic SST appear to be due to the covariability between COAs within the internally generated midlatitude zonal wave train.

The AMIP models, however, appear to be highly sensitive to ENSO's influence in the concurrent summer. Significant negative correlations in the eastern equatorial Pacific and positive correlations in the western tropical Pacific tie model summer warming to an ocean described as "perfect" for widespread midlatitude drying (Hoerling and Kumar 2003). Models shown do not feature significant correlations in the Caribbean Sea, suggesting an absence of Great Plains low-level jet–driven climate variability in AMIP simulations, consistent with the findings of Ruiz-Barradas and Nigam (2006). Model Z_{300} anomalies are generally positive in the midlatitudes in either hemisphere. The interhemispheric symmetry of these zonal bands of high pressure is indicative of tropical SST forcing.

Lead–lag correlations between U.S. summer SAT and the seasonally averaged Niño-3.4 index show how models are sensitive to ENSO conditions (Fig. 9). Observed lead–lag correlations (thick black line in Fig. 9) are compared to ensemble mean PC correlations (colored lines in Fig. 9a) and to individual model realizations (thin gray lines in Fig. 9b). The realization that most resembles observations in Fig. 9b is highlighted in blue. Correlations that fall within the shaded regions are significant at 95%. In observations, JJA SAT PC1 does not significantly correlate with the Niño-3.4 index until the subsequent winter–spring [from February–April (FMA) to May–July (MJJ)], indicating an association between JJA SAT EOF1 and a developing ENSO event. All but two ensemble mean PC1s, representing SST-forced SAT variability, correlate significantly with the Niño-3.4 index in the antecedent winter–spring, with correlations peaking at a two-month lead [April–June (AMJ)]. All ensemble mean PC1s correlate with the Niño-3.4 at lag 0, illustrating the role La Niña conditions may play in warm summer conditions over the United States in models. Individual realizations show a complex correlation picture owing to the presence of internal variability in each PC1. The average across all realization correlations is shown in red in Fig. 9, which crosses the 95% significance threshold in AMJ. Because the preseason ENSO-forced signal emerges even in the presence of internal variability, the response of the model atmosphere to SST variability must also be addressed to reduce summer SAT biases.

6. Conclusions

We show that while winter SAT variability over the continental United States is well represented in the AMIP experiment, the AMIP models do not reproduce observed patterns of U.S. SAT variability in boreal summer. The AMIP models evaluated here feature either a spurious region of high summer SAT variability displaced south and/or west of observed or a significant climatological warm bias in the central United States. To address these errors, we investigate potential sources of excessive U.S. summer SAT variability in the AMIP experiment. In observations, the leading mode of U.S. summer SAT variability between 1979 and 2008 is associated with a large-scale anticyclone over the north-central United States. Significant correlations between SAT EOF1 and Q_H suggest that the land surface contributes to variability on the margins of the observed COA but is a second-order influence in the region of highest SAT variability. The majority of models have JJA SAT EOF1s that resemble the observed COA, but all feature variability extending farther south and/or west than observed to coincide with regions of high sensible heat variability. Models with enhanced SAT variability over the central United States show high temporal correlations between SAT and Q_H

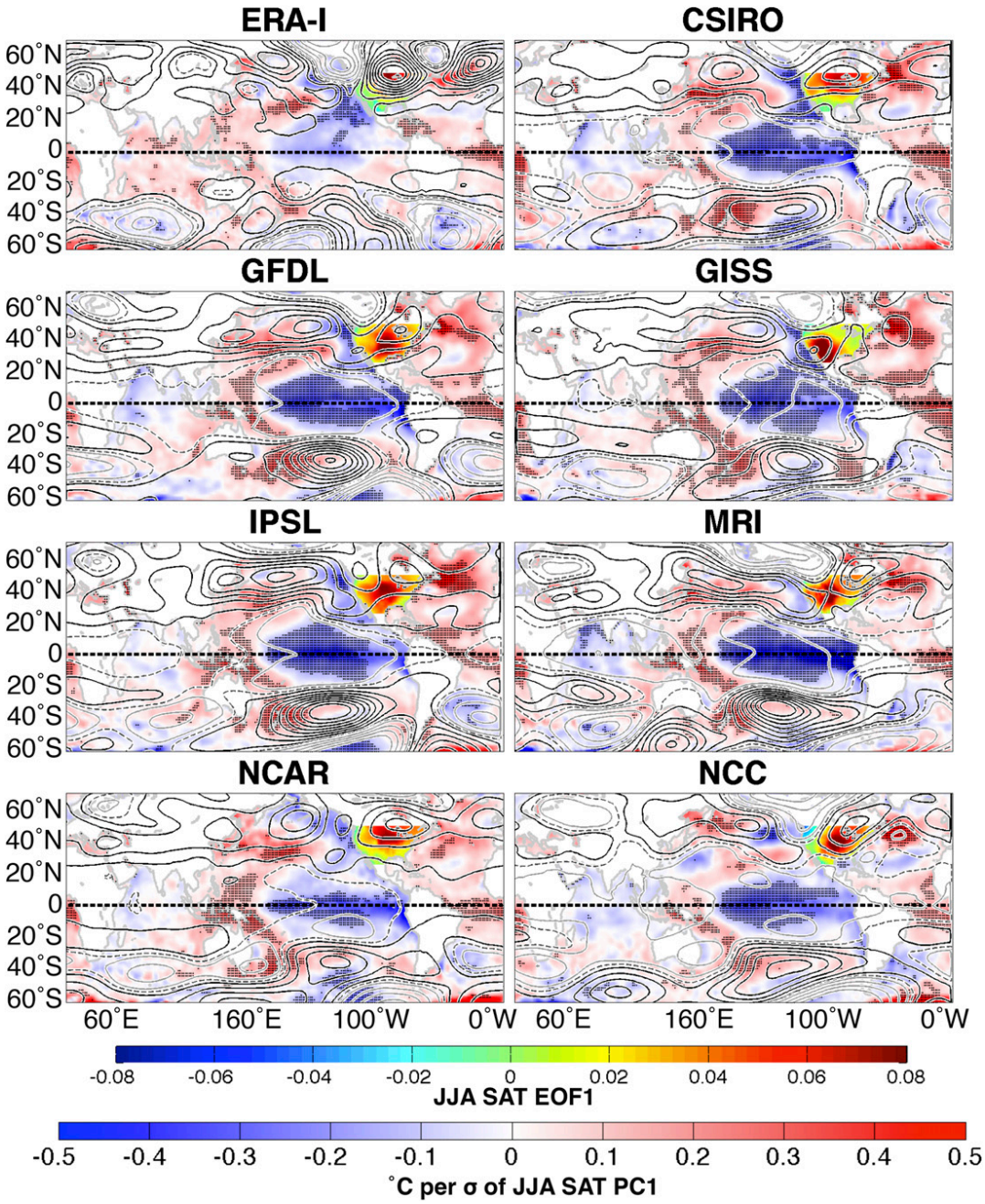

FIG. 8. Maps show regression of SST (color) and Z_{300} (contours) on normalized JJA (ensemble mean) SAT PC1. Regions of significant correlations (95% confidence) between SAT PC1 and SST are stippled. Models shown have statistically significant correlations between their ensemble mean JJA SAT PC1 and observed JJA SAT PC1 (Fig. 7, bottom). Positive Z_{300} contours (black) range from 2 to 30 m, and negative contours (light gray) range from −2 to −14 m in 4-m intervals. The 0 m contour is dashed in dark gray. The regressions can be interpreted as the dimensioned variation in SST (°C) or Z_{300} (m) per standard deviation of SAT PC1.

in their COAs, which suggests a robust land–atmosphere coupling in that region.

To quantify the relative contributions of circulation (Z_{500}) and the land surface (Q_H) on JJA SAT variability, a multivariate regression is performed in the regions of highest variability within each SAT EOF1 COA. Spurious central U.S. SAT variability associates more closely with variations in sensible heat than with variations in circulation and occurs in regions where the land and atmosphere are strongly coupled. Models with Q_H-dominated SAT variability have higher values of mean evapotranspiration in the central United

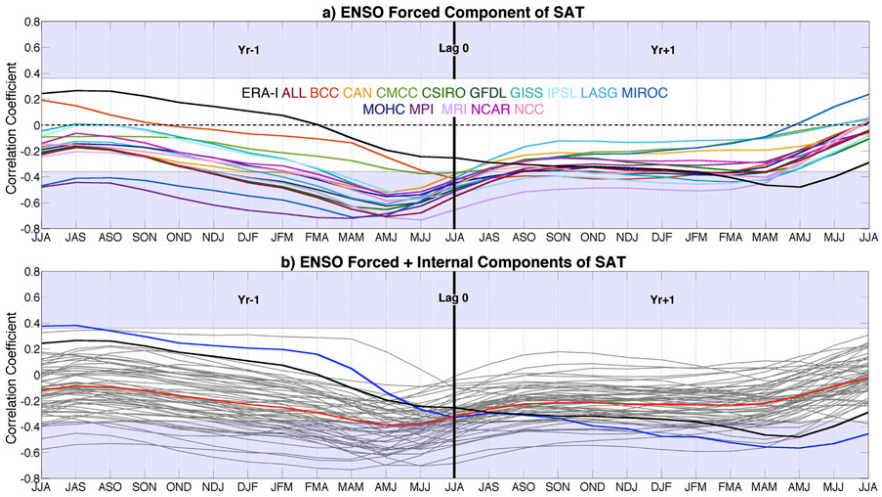

FIG. 9. Lead–lag correlations between the seasonally averaged Niño-3.4 index and JJA SAT PC1. (a) Observed correlations (thick black line) compared to the model ensemble mean correlations. (b) Observed correlations are compared to correlations of each model realization (thin gray lines). The realization correlation that most resembles observations is highlighted in blue. The average across all realization correlations is shown in red. Correlations that fall within the shaded regions are significant at 95%.

States than models with circulation-associated SAT variability. These higher values aid in setting realistic SAT climatology in the central United States but contribute to additional SAT variability. Models with circulation-dominated SAT variability tend to have a climatological warm bias in the central United States, with mean summer temperatures up to 8°C warmer than observed. This warm bias is tied to lower mean evapotranspiration in the region than observed, which results in the land surface having a more realistic influence on SAT variability. All models evaluated appear to have land surface–associated SAT biases in the central United States.

Addressing issues with the bulk land–atmosphere interaction is challenging as the exchanges of energy, water, and momentum between the surface and atmosphere are complex and largely taking place at subgrid scales (e.g., Ek and Holtslag 2004; Sellers et al. 1997). Our understanding of large-scale land–atmosphere interactions is rapidly improving, but current observations are spatially and temporally insufficient to be used to ''tune'' relevant model parameters. Land surface model grid cells are forced by the model atmosphere, where biases in precipitation and cloud radiative processes affect water and energy cycles (e.g., Ruiz-Barradas and Nigam 2006; Vial et al. 2013). Grid cells are mosaicked with different land-cover types to account for urban and vegetated areas. Vegetated areas are further subdivided by plant functional type to account for variations in plant morphology, such as leaf and stem area and canopy height (Bonan et al. 2002). Many models account for land-use changes from harvests, fires, and urbanization on seasonal time scales, as green vegetation fraction impacts the surface energy budget (Ek et al. 2003). The type and vertical layer structure of soils must be considered to replicate the effects of surface albedo and soil moisture memory. The aggregate of physical parameterizations are ultimately integrated to pass information to the atmosphere on a gridbox scale. Process scale assessments and a detailed understanding of the model physics are necessary to identify specific processes that cause the land–atmosphere issues in the AMIP experiment.

Tropical SST forcing contributes to summer SAT variability over the United States. Models respond to SST patterns that are different than observed but similar to one another. High correlations between JJA SAT PC1 and SST in the equatorial Pacific, accompanied by interhemispherically symmetric bands of high pressure in the upper troposphere, indicate that the ENSO contribution to extratropical climate variability in the summer is too high in models. Most models are sensitive to ENSO conditions in the antecedent spring and all models significantly correlate with the Niño-3.4 index at lag 0. This forced signal emerges above internal variability.

We conclude that an excessive land surface feedback is responsible for spurious U.S. summer SAT variability in the AMIP experiment. Further examination of the AMIP land surface feedback is warranted, particularly in conjunction with regional observations and on time scales conducive to assessing the directionality of control–response relationships. The AMIP biases documented in this study affect regions identified from models as hot spots of land–atmosphere interaction (Koster et al.

2004a) and limit the skill of model-based attributions of extreme heat wave events (Stott et al. 2004). Evaluating physical parameterizations that contribute to the bulk land surface feedback, precipitation variability, and cloud biases is key to improving model skill in simulating summer climate variability.

Acknowledgments. This work is supported by the National Science Foundation Graduate Research Fellowship Program under Grant DGE-1144086. We are grateful to the World Climate Research Programme's Working Group on Coupled Modelling for coordinating the CMIP5 experiment and to the participating climate modeling groups (listed in Table 1 of this paper) for providing the model output used in this study. NCEP reanalysis data are provided by the NOAA/OAR/ESRL PSD, Boulder, Colorado, from their website (http://www.esrl.noaa.gov/psd/). We thank Yu Kosaka for helping to initiate this project and Clara Deser, Karen McKinnon, Michael Ek, and Randal Koster for their valuable feedback during the writing process. We also thank the three anonymous reviewers, whose insights greatly improved this manuscript.

REFERENCES

Arblaster, J., and L. Alexander, 2012: The impact of El Niño–Southern Oscillation on maximum temperature extremes. *Geophys. Res. Lett.*, **39**, L20702, doi:10.1029/2012GL053409.

Arora, V. K., and Coauthors, 2011: Carbon emission limits required to satisfy future representative concentration pathways of greenhouse gases. *Geophys. Res. Lett.*, **38**, L05805, doi:10.1029/2010GL046270.

Bao, Q., and Coauthors, 2013: The Flexible Global Ocean–Atmosphere–Land System Model, spectral version 2: FGOALS-s2. *Adv. Atmos. Sci.*, **30**, 561–576, doi:10.1007/s00376-012-2113-9.

Barlow, M., S. Nigam, and J. M. Wallace, 2001: ENSO, Pacific decadal variability, and U.S. summertime precipitation, drought, and stream flow. *J. Climate*, **14**, 2105–2128, doi:10.1175/1520-0442(2001)014<2105:EPDVAU>2.0.CO;2.

Bentsen, M., and Coauthors, 2013: The Norwegian Earth System Model, NorESM1-M—Part 1: Description and basic evaluation of the physical climate. *Geosci. Model Dev.*, **6**, 687–720, doi:10.5194/gmd-6-687-2013.

Berg, A., B. R. Lintner, K. L. Findell, S. Malyshev, P. C. Loikith, and P. Gentine, 2014: Impact of soil moisture–atmosphere interactions on surface temperature distribution. *J. Climate*, **27**, 7976–7993, doi:10.1175/JCLI-D-13-00591.1.

Bonan, G. B., K. W. Oleson, M. Vertenstein, S. Levis, X. Zeng, Y. Dai, R. E. Dickinson, and Z.-L. Yang, 2002: The land surface climatology of the Community Land Model coupled to the NCAR Community Climate Model. *J. Climate*, **15**, 3123–3149, doi:10.1175/1520-0442(2002)015<3123:TLSCOT>2.0.CO;2.

Charney, J., and J. G. DeVore, 1979: Multiple flow equilibria in the atmosphere and blocking. *J. Atmos. Sci.*, **36**, 1205–1216, doi:10.1175/1520-0469(1979)036<1205:MFEITA>2.0.CO;2.

Collins, W. J., and Coauthors, 2011: Development and evaluation of an Earth-system model—HadGEM2. *Geosci. Model Dev.*, **4**, 1051–1075, doi:10.5194/gmd-4-1051-2011.

Davis, R. E., B. P. Hayden, D. A. Gay, W. L. Phillips, and G. V. Jones, 1997: The North Atlantic subtropical anticyclone. *J. Climate*, **10**, 728–744, doi:10.1175/1520-0442(1997)010<0728:TNASA>2.0.CO;2.

Dee, D. P., and Coauthors, 2011: The ERA-Interim reanalysis: Configuration and performance of the data assimilation system. *Quart. J. Roy. Meteor. Soc.*, **137**, 553–597, doi:10.1002/qj.828.

Deser, C., A. Phillips, V. Bourdette, and H. Teng, 2012: Uncertainty in climate change projections: The role of internal variability. *Climate Dyn.*, **38**, 527–547, doi:10.1007/s00382-010-0977-x.

——, ——, M. A. Alexander, and B. V. Smoliak, 2014: Projecting North American climate over the next 50 years: Uncertainty due to internal variability. *J. Climate*, **27**, 2271–2296, doi:10.1175/JCLI-D-13-00451.1.

——, L. Terray, and A. S. Phillips, 2015: Forced and internal components of winter air temperature trends over North America during the past 50 years: Mechanisms and implications. *J. Climate*, **29**, 2237–2258, doi:10.1175/JCLI-D-15-0304.1.

Diffenbaugh, N., J. Pal, R. Trapp, and F. Giorgi, 2005: Fine-scale processes regulate the response of extreme events to global climate change. *Proc. Natl. Acad. Sci. USA*, **102**, 15 774–15 778, doi:10.1073/pnas.0506042102.

Ding, Q., and B. Wang, 2005: Circumglobal teleconnection in the Northern Hemisphere summer. *J. Climate*, **18**, 3483–3505, doi:10.1175/JCLI3473.1.

——, ——, J. M. Wallace, and G. Branstator, 2011: Tropical–extratropical teleconnections in boreal summer: Observed interannual variability. *J. Climate*, **24**, 1878–1896, doi:10.1175/2011JCLI3621.1.

Dirmeyer, P. A., 2011: The terrestrial segment of soil moisture–climate coupling. *Geophys. Res. Lett.*, **38**, L16702, doi:10.1029/2011GL048268.

——, Y. Jin, B. Singh, and X. Yan, 2013a: Evolving land–atmosphere interactions over North America from CMIP5 simulations. *J. Climate*, **26**, 7313–7327, doi:10.1175/JCLI-D-12-00454.1.

——, ——, ——, and ——, 2013b: Trends in land–atmosphere interactions from CMIP5 simulations. *J. Hydrometeor.*, **14**, 829–849, doi:10.1175/JHM-D-12-0107.1.

——, Z. Wang, M. J. Mbuh, and H. E. Norton, 2014: Intensified land surface control on boundary layer growth in a changing climate. *Geophys. Res. Lett.*, **41**, 1290–1294, doi:10.1002/2013GL058826.

Donner, L. J., and Coauthors, 2011: The dynamical core, physical parameterizations, and basic simulation characteristics of the atmospheric component AM3 of the GFDL global coupled model CM3. *J. Climate*, **24**, 3484–3519, doi:10.1175/2011JCLI3955.1.

Dufresne, J.-L., and Coauthors, 2013: Climate change projections using the IPSL-CM5 Earth system model: From CMIP3 to CMIP5. *Climate Dyn.*, **40**, 2123–2165, doi:10.1007/s00382-012-1636-1.

Egger, J., 1978: Dynamics of blocking highs. *J. Atmos. Sci.*, **35**, 1788–1801, doi:10.1175/1520-0469(1978)035<1788:DOBH>2.0.CO;2.

Ek, M. B., and A. A. M. Holtslag, 2004: Influence of soil moisture on boundary layer cloud development. *J. Hydrometeor.*, **5**, 86–99, doi:10.1175/1525-7541(2004)005<0086:IOSMOB>2.0.CO;2.

——, K. E. Mitchell, Y. Lin, E. Rogers, P. Grunmann, V. Koren, G. Gayno, and J. D. Tarpley, 2003: Implementation of Noah land surface model advancements in the National Centers for Environmental Prediction operational mesoscale Eta Model. *J. Geophys. Res.*, **108**, 8851, doi:10.1029/2002JD003296.

Ferguson, C. R., E. F. Wood, and R. K. Vinukollu, 2012: A global intercomparison of modeled and observed land–atmosphere coupling. *J. Hydrometeor.*, **13**, 749–784, doi:10.1175/JHM-D-11-0119.1.

Findell, K., and E. Eltahir, 2003: The impact of El Niño–Southern Oscillation on maximum temperature extremes.

J. Hydrometeor., **4**, 570–583, doi:10.1175/1525-7541(2003)004<0570:ACOSML>2.0.CO;2.

Fischer, E., S. Seneviratne, P. Vidale, D. Lüthi, and C. Schär, 2007a: Soil moisture–atmosphere interactions during the 2003 European summer heatwave. *J. Climate*, **20**, 5081–5099, doi:10.1175/JCLI4288.1.

——, ——, D. Lüthi, and C. Schär, 2007b: The contribution of land–atmosphere coupling to recent European summer heatwaves. *Geophys. Res. Lett.*, **34**, L06707, doi:10.1029/2006GL029068.

Flato, G., and Coauthors, 2013: Evaluation of climate models. *Climate Change 2013: The Physical Science Basis*, T. F. Stocker et al., Eds., Cambridge University Press, 741–866. [Available online at http://www.ipcc.ch/pdf/assessment-report/ar5/wg1/WG1AR5_Chapter09_FINAL.pdf.]

Ganguly, A. R., K. Steinhaeuser, D. J. Erickson III, M. Branstetter, E. S. Parish, N. Singh, J. Drake, and L. Buja, 2009: Higher trends but larger uncertainty and geographic variability in 21st century temperature and heat waves. *Proc. Natl. Acad. Sci. USA*, **106**, 15 555–15 559, doi:10.1073/pnas.0904495106.

Gent, P. R., and Coauthors, 2011: The Community Climate System Model version 4. *J. Climate*, **24**, 4973–4991, doi:10.1175/2011JCLI4083.1.

Giorgetta, M., and Coauthors, 2012: CMIP5 simulations of the Max Planck Institute for Meteorology (MPI-M) based on the MPI-ESM-LR model: The AMIP experiment, served by ESGF. DKRZ World Data Center for Climate, accessed 2 April 2015, doi:10.1594/WDCC/CMIP5.MXELam.

Higgins, R., A. Leetmaa, Y. Xue, and A. Barnston, 2000: Dominant factors influencing the seasonal predictability of U.S. precipitation and surface air temperature. *J. Climate*, **13**, 3994–4017, doi:10.1175/1520-0442(2000)013<3994:DFITSP>2.0.CO;2.

Hoerling, M., and A. Kumar, 2003: The perfect ocean for drought. *Science*, **299**, 691–694, doi:10.1126/science.1079053.

——, and Coauthors, 2013: Anatomy of an extreme event. *J. Climate*, **26**, 2811–2832, doi:10.1175/JCLI-D-12-00270.1.

Kay, J. E., and Coauthors, 2015: The Community Earth System Model (CESM) large ensemble project: A community resource for studying climate change in the presence of internal climate variability. *Bull. Amer. Meteor. Soc.*, **96**, 1333–1349, doi:10.1175/BAMS-D-13-00255.1.

Kim, D., A. Sobel, A. D. Del Genio, Y.-H. Chen, S. Camargo, M.-S. Yao, M. Kelley, and L. Nazarenko, 2012: The tropical subseasonal variability simulated in the NASA GISS general circulation model. *J. Climate*, **25**, 4641–4659, doi:10.1175/JCLI-D-11-00447.1.

Koster, R. D., and Coauthors, 2004a: Realistic initialization of land surface states: Impacts on subseasonal forecast skill. *J. Hydrometeor.*, **5**, 1049–1063, doi:10.1175/JHM-387.1.

——, and Coauthors, 2004b: Regions of strong coupling between soil moisture and precipitation. *Science*, **305**, 1138–1140, doi:10.1126/science.1100217.

——, and Coauthors, 2006: GLACE: The Global Land–Atmosphere Coupling Experiment. Part I: Overview. *J. Hydrometeor.*, **7**, 590–610, doi:10.1175/JHM510.1.

——, and Coauthors, 2011: The second phase of the Global Land–Atmosphere Coupling Experiment: Soil moisture contributions to subseasonal forecast skill. *J. Hydrometeor.*, **12**, 805–822, doi:10.1175/2011JHM1365.1.

Kushnir, Y., R. Seager, M. Ting, N. Naik, and J. Nakamura, 2010: Mechanisms of tropical Atlantic SST influence on North American precipitation variability. *J. Climate*, **23**, 5610–5628, doi:10.1175/2010JCLI3172.1.

Lau, N.-C., and M. J. Nath, 2012: A model study of heat waves over North America: Meteorological aspects and projections for the twenty-first century. *J. Climate*, **25**, 4761–4784, doi:10.1175/JCLI-D-11-00575.1.

——, A. Leetmaa, and M. J. Nath, 2006: Attribution of atmospheric variations in the 1997–2003 period to SST anomalies in the Pacific and Indian Ocean basins. *J. Climate*, **19**, 3607–3628, doi:10.1175/JCLI3813.1.

Lorenz, R., E. Jaeger, and S. Seneviratne, 2010: Persistence of heat waves and its link to soil moisture memory. *Geophys. Res. Lett.*, **37**, L09703, doi:10.1029/2010GL042764.

——, A. J. Pitman, A. L. Hirsch, and J. Srbinovsky, 2015: Intraseasonal versus interannual measures of land–atmosphere coupling strength in a global climate model: GLACE-1 versus GLACE-CMIP5 Experiments in ACCESS1.3b. *J. Hydrometeor.*, **16**, 2276–2295, doi:10.1175/JHM-D-14-0206.1.

McCabe, G., M. Palecki, and J. Betancourt, 2004: Pacific and Atlantic Ocean influences on multidecadal drought frequency in the United States. *Proc. Natl. Acad. Sci. USA*, **101**, 4136–4141, doi:10.1073/pnas.0306738101.

Meehl, G. A., and C. Tebaldi, 2004: More intense, more frequent, and longer lasting heat waves in the 21st century. *Science*, **305**, 994–997, doi:10.1126/science.1098704.

Mesinger, F., and Coauthors, 2006: NCEP North American Regional Reanalysis. *Bull. Amer. Meteor. Soc.*, **87**, 343–360, doi:10.1175/BAMS-87-3-343.

Miralles, D. G., M. van den Berg, R. Teuling, and R. D. Jeu, 2012: Soil moisture–temperature coupling: A multiscale observational analysis. *Geophys. Res. Lett.*, **39**, L21707, doi:10.1029/2012GL053703.

——, A. J. Teuling, C. C. van Heerwaarden, and J. V.-G. de Arellano, 2014: Mega-heatwave temperatures due to combined soil desiccation and atmospheric heat accumulation. *Nat. Geosci.*, **7**, 345–349, doi:10.1038/ngeo2141.

Mueller, B., and S. Seneviratne, 2014: Systematic land climate and evapotranspiration biases in CMIP5 simulations. *J. Hydrometeor.*, **41**, 128–134, doi:10.1002/2013GL058055.

Nigam, S., and A. Ruiz-Barradas, 2006: Seasonal hydroclimate variability over North America in global and regional reanalyses and AMIP simulations: A mixed assessment. *J. Climate*, **19**, 815–837, doi:10.1175/JCLI3635.1.

NOAA/NWS, 2015: Natural hazard statistics: Weather fatalities. National Climatic Data Center, accessed 20 August 2015. [Available online at http://www.nws.noaa.gov/om/hazstats.shtml.]

Pegion, P. J., and A. Kumar, 2010: Multimodel estimates of atmospheric response to modes of SST variability and implications for droughts. *J. Climate*, **23**, 4327–4341, doi:10.1175/2010JCLI3295.1.

Perkins, S., 2015: A review on the scientific understanding of heatwaves—Their measurement, driving mechanisms, and changes at the global scale. *Atmos. Res.*, **164–165**, 242–267, doi:10.1016/j.atmosres.2015.05.014.

Rotstayn, L. D., S. J. Jeffrey, M. A. Collier, S. M. Dravitzki, A. C. Hirst, J. I. Syktus, and K. K. Wong, 2012: Aerosol- and greenhouse gas–induced changes in summer rainfall and circulation in the Australasian region: A study using single-forcing climate simulations. *Atmos. Chem. Phys.*, **12**, 6377–6404, doi:10.5194/acp-12-6377-2012.

Ruiz-Barradas, A., and S. Nigam, 2005: Warm season rainfall variability over the U.S. Great Plains in observations, NCEP and ERA-40 reanalyses, and NCAR and NASA atmospheric model simulations. *J. Climate*, **18**, 1808–1830, doi:10.1175/JCLI3343.1.

——, and ——, 2006: IPCC's twentieth-century climate simulations: Varied representations of North American hydroclimate variability. *J. Climate*, **19**, 4041–4058, doi:10.1175/JCLI3809.1.

——, and ——, 2013: Atmosphere–land surface interactions over the Southern Great Plains: Characterization from pentad analysis of DOE ARM field observations and NARR. *J. Climate*, **26**, 875–886, doi:10.1175/JCLI-D-11-00380.1.

Schubert, S., M. J. Suarez, P. J. Pegion, R. D. Koster, and J. T. Bachmeister, 2004: Causes of long-term drought in the U.S. Great Plains. *J. Climate*, **17**, 485–503, doi:10.1175/1520-0442(2004)017<0485:COLDIT>2.0.CO;2.

——, and Coauthors, 2009: A U.S. CLIVAR project to assess and compare the responses of global climate models to drought-related SST forcing patterns: Overview and results. *J. Climate*, **22**, 5251–5272, doi:10.1175/2009JCLI3060.1.

Scoccimarro, E., and Coauthors, 2011: Effects of tropical cyclones on ocean heat transport in a high-resolution coupled general circulation model. *J. Climate*, **24**, 4368–4384, doi:10.1175/2011JCLI4104.1.

Seager, R., N. Harnik, Y. Kushnir, W. Robinson, and J. Miller, 2003: Mechanisms of hemispherically symmetric climate variability. *J. Climate*, **16**, 2960–2978, doi:10.1175/1520-0442(2003)016<2960:MOHSCV>2.0.CO;2.

——, Y. Kushnir, C. Herweijer, N. Naik, and J. Velez, 2005: Modeling of tropical forcing of persistent droughts and pluvials over western North America: 1856–2000. *J. Climate*, **18**, 4065–4088, doi:10.1175/JCLI3522.1.

Sellers, P. J., and Coauthors, 1997: Modeling the exchanges of energy, water, and carbon between continents and the atmosphere. *Science*, **275**, 502–509, doi:10.1126/science.275.5299.502.

Seneviratne, S., D. Lüthi, M. Litschi, and C. Schär, 2006: Land–atmosphere coupling and climate change in Europe. *Nature*, **443**, 205–209, doi:10.1038/nature05095.

——, T. Corti, E. Davin, M. Hirschi, E. Jaeger, I. Lehner, B. Orlowsky, and A. Teuling, 2010: Investigating soil moisture–climate interactions in a changing climate: A review. *Earth-Sci. Rev.*, **99**, 125–161, doi:10.1016/j.earscirev.2010.02.004.

Shaw, T. A., and A. Voigt, 2015: Tug of war on summertime circulation between radiative forcing and sea surface warming. *Nat. Geosci.*, **8**, 560–566, doi:10.1038/ngeo2449.

Sheffield, J., and Coauthors, 2013: North American climate in CMIP5 experiments. Part II: Evaluation of historical simulations of intraseasonal to decadal variability. *J. Climate*, **26**, 9247–9290, doi:10.1175/JCLI-D-12-00593.1.

Stott, P. A., D. A. Stone, and M. R. Allen, 2004: Human contribution to the European heatwave of 2003. *Nature*, **432**, 610–614, doi:10.1038/nature03089.

Sutton, R., and D. Hodson, 2005: Atlantic Ocean forcing of North American and European summer climate. *Science*, **309**, 115–118, doi:10.1126/science.1109496.

Taylor, K. E., R. J. Stouffer, and G. A. Meehl, 2012: An overview of CMIP5 and the experiment design. *Bull. Amer. Meteor. Soc.*, **93**, 485–498, doi:10.1175/BAMS-D-11-00094.1.

Thacker, M. T., R. Lee, R. I. Sabogal, and A. Henderson, 2008: Overview of deaths associated with natural events, United States, 1979–2004. *Disasters*, **32**, 303–315, doi:10.1111/j.1467-7717.2008.01041.x.

Thompson, D. W. J., and J. M. Wallace, 2000: Annular modes in the extratropical circulation. Part I: Month-to-month variability. *J. Climate*, **13**, 1000–1016, doi:10.1175/1520-0442(2000)013<1000:AMITEC>2.0.CO;2.

Ting, M., 1994: Maintenance of northern summer stationary waves in a GCM. *J. Atmos. Sci.*, **51**, 3286–3308, doi:10.1175/1520-0469(1994)051<3286:MONSSW>2.0.CO;2.

Trenberth, K. E., J. T. Fasullo, and J. Mackaro, 2011: Atmospheric moisture transports from ocean to land and global energy flows in reanalyses. *J. Climate*, **24**, 4907–4924, doi:10.1175/2011JCLI4171.1.

Vial, J., J.-L. Dufresne, and S. Bony, 2013: On the interpretation of inter-model spread in CMIP5 climate sensitivity estimates. *Climate Dyn.*, **41**, 3339–3362, doi:10.1007/s00382-013-1725-9.

Wallace, J. M., Y. Zhang, and J. A. Renwick, 1995: Dynamic contribution to hemispheric mean temperature trends. *Science*, **270**, 780–783, doi:10.1126/science.270.5237.780.

——, C. Deser, B. Smoliak, and A. Phillips, 2015: Attribution of climate change in the presence of internal variability. *Climate Change: Multidecadal and Beyond*, C.-P. Chang et al., Eds., World Scientific Publishing, 1–29.

Wang, H., and M. Ting, 1999: Seasonal cycle of the climatological stationary waves in the NCEP–NCAR reanalysis. *J. Atmos. Sci.*, **56**, 3892–3919, doi:10.1175/1520-0469(1999)056<3892:SCOTCS>2.0.CO;2.

Watanabe, M., and Coauthors, 2010: Improved climate simulation by MIROC5: Mean states, variability, and climate sensitivity. *J. Climate*, **23**, 6312–6335, doi:10.1175/2010JCLI3679.1.

Weaver, S. J., 2013: Factors associated with decadal variability in Great Plains summertime surface temperatures. *J. Climate*, **26**, 343–350, doi:10.1175/JCLI-D-11-00713.1.

Whitman, S., G. Good, E. Donoghue, N. Benbow, W. Shou, and S. Mou, 1997: Mortality in Chicago attributed to the July 1995 heat wave. *Amer. J. Public Health*, **87**, 1515–1518, doi:10.2105/AJPH.87.9.1515.

Wu, T., and Coauthors, 2014: An overview of BCC climate system model development and application for climate change studies. *J. Meteor. Res.*, **28**, 34–56, doi:10.1007/s13351-014-3041-7.

Wu, W., and R. E. Dickinson, 2005: Warm-season rainfall variability over the U.S. Great Plains and its correlation with evapotranspiration in a climate simulation. *Geophys. Res. Lett.*, **32**, L17402, doi:10.1029/2005GL023422.

Xie, S.-P., and Coauthors, 2015: Towards predictive understanding of regional climate change. *Nat. Climate Change*, **5**, 921–930, doi:10.1038/nclimate2689.

Yukimoto, S., and Coauthors, 2012: A new global climate model of the Meteorological Research Institute: MRI-CGCM3—Model description and basic performance. *J. Meteor. Soc. Japan*, **90A**, 23–64, doi:10.2151/jmsj.2012-A02.

Zhang, J., W.-C. Wang, and L. R. Leung, 2008: Contribution of land–atmosphere coupling to summer climate variability over the contiguous United States. *J. Geophys. Res.*, **113**, D22109, doi:10.1029/2008JD010136.

Zhou, Z.-Q., S.-P. Xie, X.-T. Zheng, Q. Liu, and H. Wang, 2014: Global warming–induced changes in El Niño teleconnections over the North Pacific and North America. *J. Climate*, **27**, 9050–9064, doi:10.1175/JCLI-D-14-00254.1.

Zishka, K. M., and P. J. Smith, 1980: The climatology of cyclones and anticyclones over North America and surrounding ocean environs for January and July, 1950–77. *Mon. Wea. Rev.*, **108**, 387–401, doi:10.1175/1520-0493(1980)108<0387:TCOCAA>2.0.CO;2.

Chapter 2, in full, is a reprint of the material as it appears in *Journal of Climate*, 2016: Anna L. Merrifield and Shang-Ping Xie, "Summer U.S. Surface Air Temperature Variability: Controlling Factors and AMIP Simulation Biases." The dissertation author was the primary investigator and author of this paper.

Chapter 3

Removing Circulation Effects to Assess Central US Land-Atmosphere Interactions in the CESM Large Ensemble

AGU PUBLICATIONS

Geophysical Research Letters

RESEARCH LETTER
10.1002/2017GL074831

Key Points:
- Summer temperatures in the central U.S. are influenced by circulation and land surface conditions
- Circulation effects on summer temperatures can be removed with dynamical adjustment
- Residual temperature variability in the central U.S. reflects the land surface feedback

Supporting Information:
- Supporting Information S1

Correspondence to:
A. Merrifield,
almerrif@ucsd.edu

Citation:
Merrifield, A., Lehner, F., Xie, S.-P., & Deser, C. (2017). Removing circulation effects to assess central U.S. land-atmosphere interactions in the CESM Large Ensemble. *Geophysical Research Letters*, *44*, 9938–9946. https://doi.org/10.1002/2017GL074831

Received 12 JUL 2017
Accepted 17 SEP 2017
Accepted article online 22 SEP 2017
Published online 13 OCT 2017

Removing Circulation Effects to Assess Central U.S. Land-Atmosphere Interactions in the CESM Large Ensemble

Anna Merrifield[1], Flavio Lehner[2], Shang-Ping Xie[1], and Clara Deser[2]

[1]Scripps Institution of Oceanography, University of California, San Diego, CA, USA, [2]Climate and Global Dynamics Division, National Center for Atmospheric Research, Boulder, CO, USA

Abstract Interannual variability of summer surface air temperature (SAT) in the central United States (U.S.) is influenced by atmospheric circulation and land surface feedbacks. Here a method of dynamical adjustment is used to remove the effects of circulation on summer SAT variability over North America in the Community Earth System Model Large Ensemble. The residual SAT variability is shown to reflect thermodynamic feedbacks associated with land surface conditions. In particular, the central U.S. is a "hot spot" of land-atmosphere interaction, with residual SAT accounting for more than half of the total SAT variability. Within the "hot spot," residual SAT anomalies show higher month-to-month persistence through the warm season and a redder spectrum than dynamically induced SAT anomalies. Residual SAT variability in this region is also shown to be related to preseason soil moisture conditions, surface flux variability, and local atmospheric pressure anomalies.

1. Introduction

Adverse impacts from anthropogenic climate change are likely to be exacerbated in summer when temperatures are already at their seasonal maximum. Indeed, exceptionally warm summers projected by climate models will jeopardize crops, strain water resources, and tax human health (Romero-Lankao et al., 2014; Lehner, Wahl, et al., 2017). With a surfeit of solar radiation present, summer SAT over land is set by large-scale atmospheric circulation patterns, topography, and cloud cover and modified regionally by land surface conditions.

The land surface influences the atmosphere through a series of nonlinear processes, linking soil moisture with evapotranspiration, cloud formation and precipitation (e.g., Findell & Eltahir, 2003; Tawfik et al., 2015a, 2015b). Modeling studies identify a "hot spot" of land-atmosphere interaction in the central U.S. (e.g., Koster et al., 2006; Lorenz et al., 2015; Zhang et al., 2008). There are indications, however, that the land-atmosphere coupling in such hot spot regions might be overestimated in climate models (Fischer et al., 2012; Sippel et al., 2017; Stegehuis et al., 2013). In the central U.S., for example, models tend to feature warmer mean SAT (Mueller & Seneviratne, 2014) and more interannual SAT variability (Berg et al., 2014; Merrifield & Xie, 2016) than observed. The land surface influence on SAT is challenging to quantify (Yang et al., 2004) due to the confounding influence of internal atmospheric variability (Deser et al., 2012; Wallace et al., 1995, 2015). For example, hot extremes brought about by persistent anticyclonic conditions in the atmosphere are often intensified by dry soils (Durre et al., 2000; Miralles et al., 2014; Vogel et al., 2017).

This study uses the empirical method of "dynamical adjustment" (Deser et al., 2016; Lehner, Deser, et al., 2017) to remove the circulation-induced component of SAT variability in the Community Earth System Large Ensemble. We examine the relative magnitude, spatial pattern, and temporal persistence of circulation versus thermodynamic drivers of summer SAT variability over the U.S., with particular attention on the central U.S. hot spot region identified in previous studies. Specifically, we evaluate whether the thermodynamic component of SAT variability helps isolate influences of anomalous land surface conditions. The remainder of the paper is structured as follows. Section 2 introduces the model simulations and dynamical adjustment methodology. Results are presented in Section 3, beginning with two case studies and then generalizing to characterize the dynamic and thermodynamic contributions to SAT variability in the Community Earth System Model Large Ensemble. Sections 4 and 5 provide a summary and discussion, respectively.

2. Climate Model Simulations and Dynamical Adjustment Methodology

We analyze the role of the atmospheric circulation and land surface condition on summer SAT variability over the historical period (1920–2005) in the 30 member ensemble of simulations conducted with the National Center of Atmospheric Research (NCAR) Community Earth System Model version 1 (CESM1), hereafter referred to as the CESM Large Ensemble (CESM-LE) (Kay et al., 2015). The CESM-LE is a fully coupled, 1° horizontal resolution initial condition ensemble; each ensemble member is subjected to identical CMIP5-based external forcing scenarios. The members differ slightly from one another in their initial atmospheric state. Large ensembles allow us to sample internal variability in the presence of forced climate changes, thereby providing a range of possible climate trajectories to analyze (Deser et al., 2012; Lehner et al., 2016).

We employ constructed circulation analogues to dynamically adjust monthly mean SAT fields in the CESM-LE. The method is summarized briefly here and in more detail in the supporting information; the reader is referred to Deser et al. (2016) for a full description.The method relies on the ability to reconstruct a given monthly mean circulation field ("target month"), represented here by monthly mean 500 mb geopotential height (Z500) as opposed to SLP as in Deser et al. (2016), from a large set of imperfect analogues obtained from the CESM1 preindustrial control simulation (Kay et al., 2015) with the same model setup. The closest analogues (in terms of Euclidean distance from the target month over the domain 20–90°N, 180–10°W) are linearly combined with an optimal set of weights, to reconstruct the target Z500 field in the CESM-LE. The same optimal linear combination is then applied to the accompanying SAT fields in the control simulation to construct the dynamically induced component of SAT. This dynamical component is then subtracted from the original SAT field of the target month to obtain the residual SAT component, which we interpret as being primarily thermodynamically induced and potentially land surface driven.

3. Results

3.1. Two Julys With Similar Circulation but Different SAT

In the central U.S., different SAT anomalies can exist under similar atmospheric circulation conditions (Figure 1). To illustrate this, we select two Julys from the CESM-LE (July 1963 of member 15, and July 1925 of member 22) featuring similar midlatitude bands of high pressure at 500 hPa (Z500) with centers in the vicinity of the Aleutian islands and the west coast of the U.S. and a low-pressure center over western Canada, similar to the pattern described by McKinnon et al. (2016). SAT anomalies in the two cases differ most notably in the central U.S., while they are broadly similar elsewhere. The configuration of SAT anomalies associated with the Z500 pattern indicate that atmospheric circulation anomalies are largely responsible for the warm (cool) anomalies in the western U.S. (Canada) (Figures 1c and 1d). The local warm anomaly over the central U.S. in case 2 (Figure 1f), which exceeds average central U.S. SAT by more than 5°C, is not accounted for by dynamical adjustment and might hence be of thermodynamic origin. In contrast, there is no significant central U.S. SAT anomaly present in case 1 (Figure 1e). To investigate possible mechanisms explaining the differences in residual SAT anomaly over the central U.S., we compare area-averaged land surface parameters in the region shown in Figures 1e and 1f (32.5–41.9°N, 90–101.25°W). We consider soil moisture, sensible and latent heat fluxes, the shortwave cloud radiative effect, which is the difference between all-sky and clear-sky downward shortwave radiation at the surface (Cheruy et al., 2014), and the diurnal temperature range, which serves as proxy for local boundary layer moisture conditions (Dai et al., 1999; Lewis & Karoly, 2013). The land surface anomalies are presented in terms of percent difference from their long-term averages.

In case 1 (green bars in Figure 1g), soils are 4% wetter than average. The surface heat flux is partitioned in favor of latent (8%) over sensible (−14%) heating. Local atmospheric conditions were largely unremarkable, with modest reductions in cloud cover (−11%) and diurnal temperature range (−2%). In case 2 (blue bars in Figure 1g), soils are 11% drier than average. Anomalously dry soil conditions exist in the previous spring in case 2, from a −4% anomaly in April to a −10% anomaly in June (not shown). The sensible heat flux in the region is more than twice the long-term average (102%), in conjunction with a 25% reduction in the latent heat flux due to drier soils. Cloud cover is below average in case 2 (−30%), which suggests that the increase of incoming shortwave radiation that accompanies reductions in cloud cover contribute to the SAT anomaly in the region. The diurnal temperature range is 30% larger than average, which is consistent with drier boundary layer conditions that result in enhanced radiative warming during the day and cooling at night. The residual SAT anomaly in case 2 likely originated from heat flux partitioning by the land surface with reduced cloud cover playing a role, a narrative consistent with other case studies (e.g., Namias, 1982; Orth & Seneviratne, 2017; Perkins, 2015).

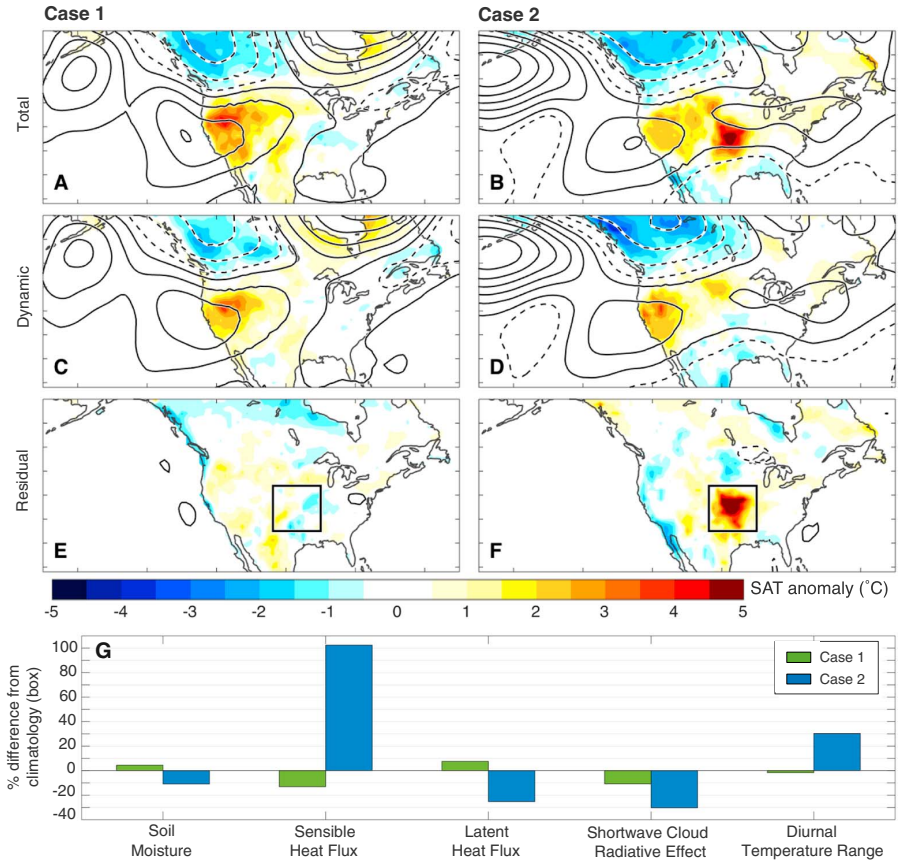

Figure 1. (a, b) Total, (c, d) dynamical, and (e,f) residual SAT anomalies (color) in two Julys with similar attendant circulation (Z500; contours) in the CESM-LE. Anomalies are calculated from the historical period mean (1920–2005). Z500 contours range from 5 to 95 m (solid) and −5 to −50 m (dashed) in 15 m intervals. (g) Area-averaged surface conditions for each July, expressed as percent difference from the historical period mean.

3.2. Defining the Hot Spot

The selected cases in Figure 1 demonstrate how residual SAT can help to identify the spatial extent and estimate the magnitude of the land surface's influence on summer SAT. To take a more general look at the SAT variability that might be driven by land surface conditions, we calculate the standard deviation (σ) of dynamic and residual SAT anomalies across all summers (June–August; JJA) of the historical portion of each member of the CESM-LE and then average the 30 σ values. Note that for each year and grid point, the ensemble-mean dynamic (residual) SAT has been subtracted from each ensemble member's dynamic (residual) SAT before computing σ, thereby isolating the contribution from internal variability. Interannual variability of dynamic JJA SAT in the CESM-LE is of comparable magnitude over the western and central U.S., though dynamics explain over three quarters of the total SAT σ in the former and less than half in the latter region (Figure 2a). Residual JJA SAT variability is highest along the arc of the Great Plains with almost no residual variability in the western U.S. (Figure 2b). The lack of residual σ west of the Rocky Mountains is consistent with the region being too dry overall for moisture variations to influence SAT (Kamae et al., 2016; Seneviratne et al., 2010). In the central U.S., the magnitude of residual variability suggests that the land surface feedbacks may be responsible for more than a quarter of total SAT σ. The southern central US (32.5–41.9°N, 90–98.75°W) stands out as a "hot spot," with more than half of the total SAT σ considered thermodynamic. Hereafter, SAT averaged over this region is defined as hot spot SAT.

The land surface's influence on SAT can also be inferred from temporal characteristics of dynamic and residual SAT within the hot spot region. Evidence of the land surface feedback can be seen on intraseasonal

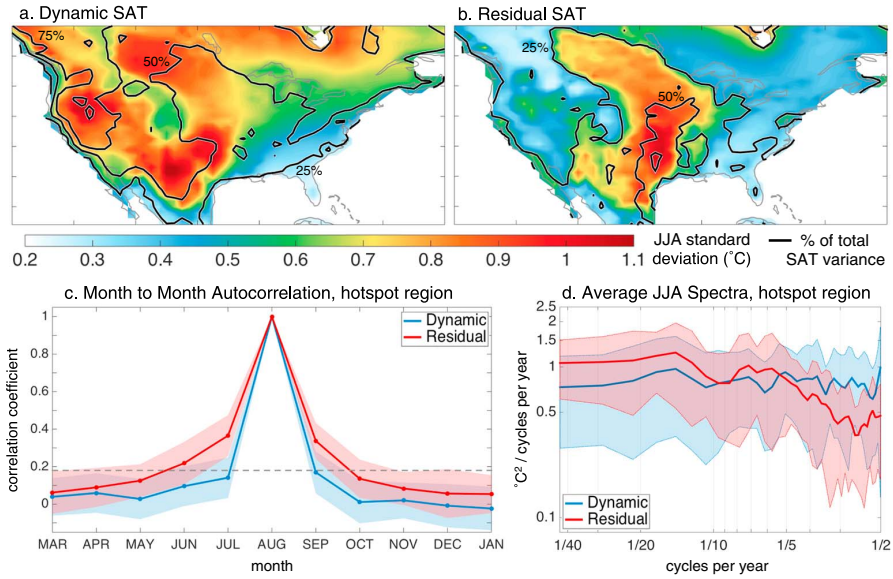

Figure 2. Standard deviation of (a) dynamic and (b) residual JJA SAT in color, overlaid with percent of total JJA SAT variance explained in black contours, averaged across 30 members of CESM-LE over the historical period. (bottom) Temporal features of hot spot region dynamic (blue) and residual (red) SAT. (c) August hot spot SAT autocorrelation and (d) spectra of JJA hot spot SAT, in terms of ensemble average (solid line) and 1σ ensemble spread (shading).

(Figure 2c) to multidecadal (Figure 2d) timescales. Autocorrelation of dynamic (blue) and residual (red) August SAT anomalies are shown in Figure 2c, where the solid curve shows the average and the shading shows the range across the 30 members of the CESM-LE. Although there is considerable spread in autocorrelations among the 30 model runs for both dynamic and residual SAT, on average, residual SAT has a longer decorrelation timescale than dynamic SAT. Residual autocorrelation significant at 95% (above gray dashed line in Figure 2c, see supporting information) arises in June and continues until September, which suggests that residual SAT originates from a persistent surface forcing which exerts influence throughout the warm season. Dynamic SAT reflects the shorter-lived influence of atmospheric circulation that is not significantly correlated from month to month. The spectra of dynamic (blue) and residual (red) JJA SAT anomalies over the 86 year historical period are shown in Figure 2d, where the solid curve shows the average and the shading shows the range across the ensemble. The spectrum of dynamic JJA SAT has approximately equal power at all frequencies, while the spectrum of residual JJA SAT has more energy at lower frequencies. The redder residual spectrum is consistent with the notion that residual SAT reflects the integration of stochastic atmospheric forcing by the land surface (Delworth & Manabe, 1993).

3.3. Developing a Thermodynamic Narrative

The above results suggest that residual SAT variability in the hot spot region might be land surface driven. Within the model, we can attempt to develop a thermodynamic narrative for this land surface influence. We explore several aspects of the land surface feedback in the JJA SAT hot spot region: the relationship between SAT and soil moisture (Figure 3) and between SAT and local SLP (Figure 4). We quantify the former by showing correlation maps of the components of JJA hot spot SAT and total soil moisture from the antecedent spring through the subsequent fall (Figure 3). Correlations (r) are computed from a concatenated record of 2,580 model years (30 simulations, 86 years each) and are determined to be significant at 95% if they exceed about 0.03 in absolute value (see supporting information). Total JJA hot spot SAT is negatively correlated with spring (March–May; MAM) soil moisture from the Gulf Coast through the central Great Plains (Figure 3i). The spatial structure of the correlation suggests that moist southerly flow from the Gulf provides the moisture necessary for the land surface to influence the atmosphere (Kushnir et al., 2010; Feng et al., 2011). The maximum of these lagged correlations ($r = -0.25$) occur in the southern portion of the hot spot. The average correlation of dynamic JJA hot spot SAT with MAM soil moisture in the hot spot is very low ($r = -0.05$; Figure 3ii), which suggests that the spring soil moisture state in the central U.S. does not influence the

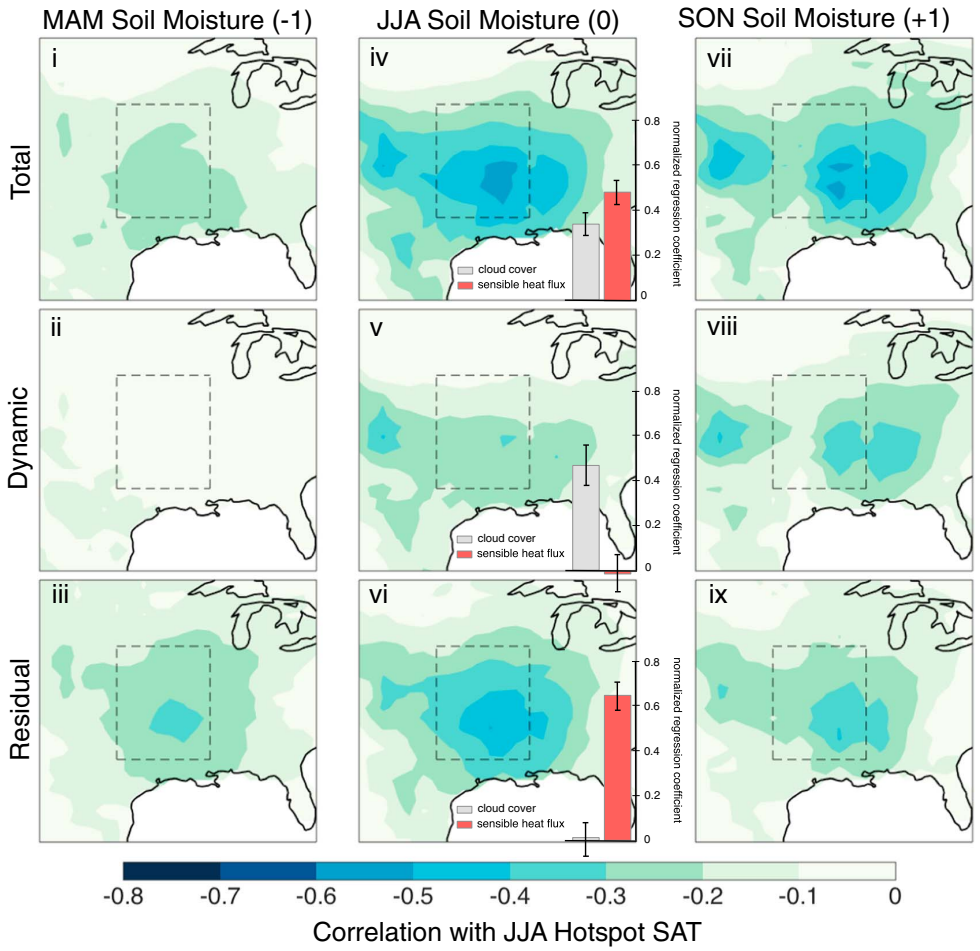

Figure 3. Correlation maps of (i, iv, vii) total, (ii, v, viii) dynamic, and (iii, vi, ix) residual JJA hot spot SAT with total column soil moisture at each grid point. The left column shows correlation with preseason (MAM) soil moisture, the middle with concurrent JJA soil moisture, and the right with postseason (SON) soil moisture. Normalized regression coefficients for JJA cloud cover (b_{cld}; gray) and sensible heat flux (b_{shf}; red) regressed on each component of JJA SAT are inlaid in Figures 3iv–3vi. Bars (whiskers) represent ensemble average (spread).

atmospheric circulation patterns that follow. Removing the influence of dynamics, however, leads to higher correlations between MAM soil moisture and JJA SAT (Figure 3iii). In fact, residual JJA hot spot SAT is more highly correlated with MAM soil moisture in the hot spot than total SAT is ($r = -0.36$). This supports our hypothesis that removing circulation-induced SAT variability allows us to better characterize SAT variability driven by the land surface feedback.

Instantaneous correlations in the hot spot are of similar magnitude for total and residual JJA SAT and JJA soil moisture, and dynamic SAT correlations remain weaker (Figures 3iv–3vi). Fall (September–November; SON) soil moisture is more highly correlated with JJA SAT and its components than MAM soil moisture is (Figures 3vii–3ix). Correlations of SON soil moisture with dynamic and residual hot spot SAT are of similar magnitude, which suggests that a hot summer dries soils in the hot spot whether the warm anomaly was circulation induced or land surface driven. To strengthen the case that residual hot spot SAT is land surface driven, we determine the relative influence of cloud cover and surface fluxes through a multivariate regression of the shortwave cloud radiative effect and the sensible heat flux on JJA hot spot SAT (bars inlaid in Figures 3iv–3vi). In each ensemble member, all fields are normalized by standard deviation at each grid point. A multivariate regression is then carried out at each grid point and the resulting normalized regression coefficients, b_{cld} and b_{shf}, are averaged over the hot spot to estimate relative contribution of clouds versus the land

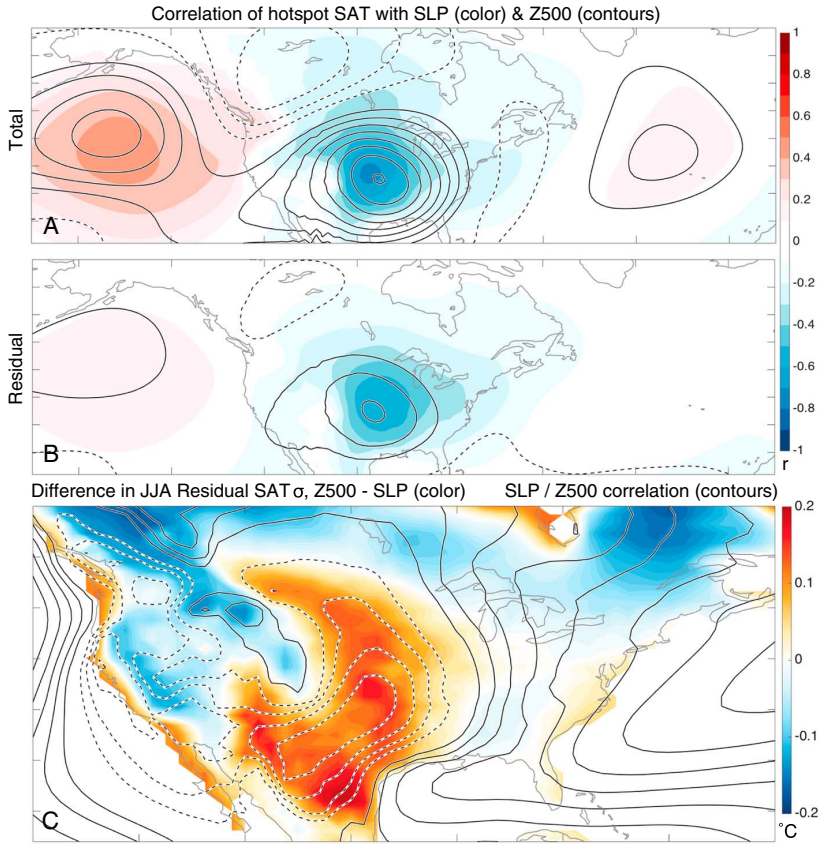

Figure 4. (a) Correlation map of total JJA hot spot SAT with SLP in color and with Z500 in contours. Z500 correlation contours range from 0.1 to 0.8 (solid) and −0.1 to −0.3 (dashed) in intervals of 0.1. (b) Same as Figure 4a, but with residual JJA hot spot SAT. (c) Difference in the standard deviation of JJA residual SAT (°C; color) using Z500 versus SLP to represent circulation. The residual SAT variability difference map is overlaid with a map of the correlation between SLP and Z500 (contours). Correlation contours range from 0.1 to 0.8 (solid) and −0.1 to −0.4 (dashed) in intervals of 0.1.

surface feedback. Bars in Figures 3iv–3vi show the average, and whiskers show the range in b_{cld} and b_{shf} across the ensemble. Cloud cover and the sensible heat flux play comparable roles in setting total JJA hot spot SAT, with an average b_{cld} of 0.34 and b_{shf} of 0.48 (Figure 3iv). This supports the narrative posited in Figure 1 that warm SAT anomalies in the hot spot occur in conjunction with clear skies, more incoming shortwave radiation, and an increased sensible heat flux. Regression on the components of JJA hot spot SAT confirm that variations in dynamic and residual SAT have different physical underpinnings. Dynamic SAT variability (Figure 3v) relates primarily to variations in cloud cover (b_{cld} = 0.46), as large cloud systems that impact radiation tend to be coupled to large-scale atmospheric circulation (Bony et al., 2015). Residual SAT variability (Figure 1vi) is primarily driven by variations in the sensible heat flux (b_{shf} = 0.64), which reflects the thermodynamic partitioning of surface fluxes by soil moisture in the hot spot region (Seneviratne et al., 2010). This illustrates the efficacy of dynamical adjustment in separating circulation induced from thermodynamic anomalies, as the method is able to reveal relationships between hot spot SAT and multiple aspects of the land surface feedback.

In winter, dynamic SAT and SLP are expected to show a quadrature relationship consistent with horizontal advection. In summer, surface lows form over hot, dry land surfaces and in regions of differential heating such as coastlines and are identifiable by a local anticorrelation between SAT and SLP (Rowson & Colucci, 1992). Because thermal lows are associated with local land surface conditions, their presence is not necessarily reflective of the large-scale circulation patterns that drive dynamic SAT. Over the ocean, the midlatitude atmosphere tends to feature SLP anomalies of the same sign as Z500 anomalies (Figure 4a). In the hot spot, positive (negative) correlations between JJA SAT and Z500 (SLP) are highest locally (Figure 4a). Low pressure

at the surface and high pressure aloft is representative of the atmospheric baroclinicity that sets up thermodynamically over hot, dry land surfaces. Dynamical adjustment removes covariability between hot spot SAT and Z500 as expected, both locally and remotely (Figure 4b). Correlations between residual hot spot SAT and SLP, however, remain almost unchanged over the hot spot region. After dynamical adjustment, local correlation between SAT and Z500 is reduced from 0.80 to 0.31 while local correlation between SAT and SLP is only reduced from −0.73 to −0.60. The magnitude of the remaining residual SAT-SLP correlation supports the thermodynamic interpretation of SAT variability in the hot spot region, that the state of the land surface (e.g., soil moisture) influences local SAT, which in turn sets up a spatially concomitant SLP signature. The remaining residual SAT-Z500 correlation is substantially reduced but not negligible, which is expected in a coupled system. The relationship may reflect the influence of large-scale circulation on soil moisture or vice versa (Fernando et al., 2016; Koster et al., 2016).

We have repeated the dynamical adjustment method using SLP (rather than Z500) as an indicator of circulation. Residual SAT σ from the two methods are compared in Figure 4c. More SAT variance is removed with SLP analogues than with Z500 analogues (i.e., Z500-derived residual σ is larger than SLP-derived residual σ) along the arc of the Great Plains, in the U.S. Southwest and Northern Mexico, and in coastal regions. These are regions where thermal lows are known to occur (Johnson, 2003) with feature of a negative correlation between Z500 and SLP (Figure 4c; dashed contours) representative of the baroclinic thermal low signature.

4. Summary

We have presented evidence that a method of dynamical adjustment developed by Deser et al. (2016) can be used to evaluate land surface-driven SAT variability in the CESM-LE. The dynamic and residual components of summer SAT are presented in terms of interannual variability, and the central U.S. hot spot of land surface-driven SAT is defined where residual variability accounts for more than half of the total JJA SAT variance. Temporal characteristics of the dynamic and residual (i.e., thermodynamic) hot spot SAT suggest that the latter is land surface driven. Finally, a general thermodynamic narrative is developed for residual SAT using the entire CESM-LE. Dynamical adjustment is able to reveal clear relationships between summer SAT and two key aspects of the land surface feedback (preseason soil moisture and sensible heat flux variability) that are normally obscured by the influence of atmospheric circulation. Dynamical adjustment performed with Z500 rather than SLP also leaves behind a thermodynamic, surface low signature that accompanies warm SAT in the hot spot. We conclude that dynamical adjustment can be used to empirically estimate the magnitude and spatial extent of land surface-driven SAT variability.

5. Discussion

Dynamical adjustment was previously employed to develop a physical understanding of SAT trends (Deser et al., 2016; Lehner, Deser, et al., 2017). The method also gives insight into interannual variability, allowing us to determine why one summer is hotter than another. Residuals tend to be larger in the summer than in the winter when horizontal advection plays a more prominent role in setting SAT (Deser et al., 2014; Sheffield et al., 2013). This does not necessarily mean that dynamical adjustment is not useful in the summer, just that thermodynamic processes play a role in setting SAT that is comparable in magnitude to dynamics. Determining the thermodynamic basis for the summer residual both validates dynamical adjustment as a method and indicates where land-atmosphere interactions may be meaningful.

We evaluate dynamical adjustment in a model, where there are thousands of years of simulation from which to pick analogues, and land surface information is temporally and spatially complete. Because dynamical adjustment is an empirical method, having as many analogues as possible is key to effectively characterizing circulation (van den Dool, 1994). Analogues may capture one aspect of circulation in the domain but have different features elsewhere and are therefore "imperfect." Additionally, care must be taken when using a linear method to explain features of a nonlinear coupled system. Land-atmosphere interactions are two way, which makes separating the forcing and response a challenge, particularly on monthly timescales (Levine et al., 2016). Further assessment of dynamical adjustment is warranted, particularly regarding its application to observational data sets (Lehner, Deser, et al., 2017). Temperature is a well-measured field, both spatially and temporally, while land surface observations tend to be limited. Developing a land-atmosphere hot spot definition based solely on temperature would allow us to leverage the observational record prior to the satellite era, ensuring robust statistics.

Acknowledgments
We thank Laurent Terray for conceiving the method of dynamical adjustment used in this study and Karen McKinnon, Adam Phillips, Nicolas Siler, and Jeffery Strong for helpful discussion. We also thank two anonymous reviewers for their constructive feedback. A. M. was supported by National Science Foundation (NSF) Graduate Research Fellowship Program under grant DGE-1144086 and the Graduate Student Visiting Fellowship at the National Center for Atmospheric Research. F. L. is supported by a Postdoc Applying Climate Expertise (PACE) fellowship cosponsored by NOAA and the Bureau of Reclamation. The CESM-LE simulations are available on the Earth System Grid (www.earthsystemgrid.org). The National Center for Atmospheric Research is sponsored by NSF.

References

Berg, A., Lintner, B. R., Findell, K. L., Malyshev, S., Loikith, P. C., & Gentine, P. (2014). Impact of soil moisture–Atmosphere interactions on surface temperature distribution. *Journal of Climate*, *27*, 7976–7993. https://doi.org/10.1175/JCLI-D-13-00591.1

Bony, S., Stevens, B., Frierson, D. M. W., Jakob, C., Kageyama, M., Pincus, R., … Webb, M. J. (2015). Clouds, circulation, and climate sensitivity. *Nature Geoscience*, *8*, 261–268. https://doi.org/10.1038/ngeo2398

Cheruy, F., Dufresne, J. L., Hourdin, F., & Ducharne, A. (2014). Role of clouds and land-atmosphere coupling in midlatitude continental summer warm biases and climate change amplification in CMIP5 simulations. *Geophysical Research Letters*, *41*, 6493–6500. https://doi.org/10.1002/2014GL061145

Dai, A., Trenberth, K., & Karl, T. (1999). Effects of clouds, soil moisture, precipitation, and water vapor on diurnal temperature range. *Journal of Climate*, 2451–2473. https://doi.org/10.1175/1520-0442(1999)012<2451: EOCSMP>2.0.CO;2

Delworth, T., & Manabe, S. (1993). Climate variability and land surface processes. *Advances in Water Resources*, *16*, 3–20. https://doi.org/10.1016/0309-1708(93)90026-C

Deser, C., Phillips, A., Alexander, M. A., & Smoliak, B. V. (2014). Projecting North American climate over the next 50 years: Uncertainty due to internal variability. *Journal of Climate*, *27*, 2271–2296. https://doi.org/10.1175/JCLI-D-13-00451.1

Deser, C., Phillips, A., Bourdette, V., & Teng, H. (2012). Uncertainty in climate change projections: the role of internal variability. *Climate Dynamics*, *38*, 527–547. https://doi.org/10.1007/s00382-010-0977-x

Deser, C. A., Terray, L., & Phillips, A. S. (2016). Forced and internal components of winter air temperature trends over North America during the past 50 years: Mechanisms and implications. *Journal of Climate*, *29*, 2237–2258. https://doi.org/10.1175/JCLI-D-15-0304.1

Durre, I., Wallace, J., & Lettenmaier, D. (2000). Dependence of extreme daily maximum temperatures on antecedent soil moisture in the contiguous United States during summer. *Journal of Climate*, *13*, 2641–2651. https://doi.org/10.1175/1520-0442(2000)013<2641:DOEDMT>2.0.CO;2

Feng, S., Hu, Q., & Oglesby, R. (2011). Influence of Atlantic sea surface temperatures on persistent drought in North America. *Climate Dynamics*, *37*, 569–586. https://doi.org/10.1007/s00382-010-0835-x

Fernando, D. N., Mo, K. C., Fu, R., Pu, B., Bowerman, A., Scanlon, B. R., … Zhang, K. (2016). What caused the spring intensification and winter demise of the 2011 drought over Texas? *Climate Dynamics*, *47*, 3077–3090. https://doi.org/10.1007/s00382-016-3014-x

Findell, K. L., & Eltahir, E. A. (2003). Atmospheric controls on soil moisture-boundary layer interactions. Part II: Feedbacks within the Continental United States. *Journal of Hydrometeorology*, *4*, 552–569. https://doi.org/10.1175/ 1525-7541(2003)004<0570:ACOSML>2.0.CO;2

Fischer, E. M., Rajczak, J., & Schär, C. (2012). Changes in European summer temperature variability revisited. *Geophysical Research Letters*, *39*, L19702. https://doi.org/10.1029/2012GL052730

Johnson, R. (2003). Thermal low. In J. Holton, J. Pyle, & J. Curry (Eds.), *Encyclopedia of Atmospheric Science* (pp. 2269–2273). London: Academic Press.

Kamae, Y., Shiogama, H., Imada, Y., Mori, M., Arakawa, O., Mizuta, R., … Ueda, H. (2016). Forced response and internal variability of summer climate over western North America. *Climate Dynamics*, *49*, 403–417. https://doi.org/10.1007/s00382-016-3350-x

Kay, J. E., Deser, C., Phillips, A., Mai, A., Hannay, C., Strand, G., … Vertenstein, M. (2015). The Community Earth System Model (CESM) Large Ensemble Project: A community resource for studying climate change in the presence of internal climate variability. *Bulletin of the American Meteorological Society*, *96*, 1333–1349. https://doi.org/10.1175/BAMS-D-13-00255.1

Koster, R., Chang, Y., Wang, H., & Schubert, S. (2016). Impacts of local soil moisture anomalies on the atmospheric circulation and on remote surface meteorological fields during boreal summer: A comprehensive analysis over North America. *Journal of Climate*, *29*, 7345–7364. https://doi.org/10.1175/JCLI-D-16-0192.1

Koster, R. D., Sud, Y. C., Guo, Z., Dirmeyer, P. A., Bonan, G., Oleson, K. W., … Xue, Y. (2006). GLACE: The Global Land-Atmosphere Coupling Experiment. Part I: Overview. *Journal of Hydrometeorology*, *7*, 590–610. https://doi.org/10.1175/JHM510.1

Kushnir, Y., Seager, R., Ting, M., Naik, N., & Nakamura, J. (2010). Mechanisms of Tropical Atlantic SST Influence on North American precipitation variability. *Journal of Climate*, *23*, 5610–5628. https://doi.org/10.1175/2010JCLI3172.1

Lehner, F., Deser, C., & Sanderson, B. (2016). Future risk of record-breaking summer temperatures and its mitigation. *Climatic Change*, 1–13. https://doi.org/10.1007/s10584-016-1616-2

Lehner, F., Deser, C., & Terray, L. (2017). Towards a new estimate of "time of emergence" of anthropogenic warming: Insights from dynamical adjustment and a large initial-condition model ensemble. *Journal of Climate*, *30*, 7739–7756. https://doi.org/10.1175/JCLI-D-16-0792.1

Lehner, F., Wahl, E. R., Wood, A. W., Blatchford, D. B., & Llewellyn, D. (2017). Assessing recent declines in Upper Rio Grande runoff efficiency from a paleoclimate perspective. *Geophysical Research Letters*, *44*, 4124–4133. https://doi.org/10.1002/2017GL073253

Levine, P. A., Randerson, J. T., Swenson, S. C., & Lawrence, D. M. (2016). Evaluating the strength of the land-atmosphere moisture feedback in Earth system models using satellite observations. *Hydrology and Earth System Sciences*, *20*(12), 4837–4856. https://doi.org/10.5194/hess-20-4837-2016

Lewis, S., & Karoly, D. (2013). Evaluation of historical diurnal temperature range trends in CMIP5 models. *Journal of Climate*, *26*, 9077–9089. https://doi.org/10.1175/JCLI-D-13-00032.1

Lorenz, R., Pitman, A. J., Hirsch, A. L., & Srbinovsky, J. (2015). Intraseasonal versus interannual measures of land-atmosphere coupling strength in a global climate model: GLACE-1 versus GLACE-CMIP5 experiments in ACCESS1.3b. *Journal of Hydrometeorology*, *16*, 2276–2295. https://doi.org/10.1175/JHM-D-14-0206.1

McKinnon, K. A., Rhines, A., Tingley, M. P., & Huybers, P. (2016). Long-lead predictions of Eastern US hot days from Pacific sea surface temperatures. *Nature Geoscience*, *9*, 389–394. https://doi.org/10.1038/ngeo2687

Merrifield, A., & Xie, S. (2016). Summer U.S. Surface air temperature variability: Controlling factors and AMIP simulation biases. *Journal of Climate*, *29*, 5123–5139. https://doi.org/10.1175/JCLI-D-15-0705.1

Miralles, D. G., Teuling, A. J., van Heerwaarden, C. C., & de Arellano, J. V.-G. (2014). Mega–heatwave temperatures due to combined soil desiccation and atmospheric heat accumulation. *Nature Geoscience*, *7*, 345–349. https://doi.org/10.1038/ngeo2141

Mueller, B., & Seneviratne, S. (2014). Systematic land climate and evapotranspiration biases in CMIP5 simulations. *Journal of Hydrometeorology*, *41*, 128–134. https://doi.org/10.1002/2013GL058055

Namias, J. (1982). Anatomy of great plains protracted heat waves (especially the 1980 U.S. summer drought). *Monthly Weather Review*, *110*, 824–838. https://doi.org/10.1175/1520-0493(1982)110<0824:AOGPPH>2.0.CO;2

Orth, R., & Seneviratne, S. (2017). Variability of soil moisture and sea surface temperatures similarly important for warm-season land climate in the community earth system model. *Journal of Climate*, *30*, 2141–2162. https://doi.org/10.1175/JCLI-D-15-0567.1

Perkins, S. E. (2015). A review on the scientific understanding of heatwaves-their measurement, driving mechanisms, and changes at the global scale. *Atmospheric Research*, *164*, 242–267. https://doi.org/10.1016/j.atmosres.2015.05.014

Romero-Lankao, P., Smith, J., Davidson, D., Diffenbaugh, N., Kinney, P., Kirshen, P., … Ruiz, L. V. (2014). North America. In V. Barros, et al. (Eds.), *Climate Change 2014: Impacts, Adaptation, and Vulnerability. Part B: Regional Aspects. Contribution of Working Group II to the Fifth Assessment Report of the Intergovernmental Panel on Climate Change* (pp. 1439–1498). Cambridge, UK: Cambridge University Press.

Rowson, D. R., & Colucci, S. J. (1992). Synoptic climatology of thermal low-pressure systems over southwestern North America. *International Journal of Climatology*, *12*, 529–545. https://doi.org/10.1002/joc.3370120602

Seneviratne, S., Corti, T., Davin, E., Hirschi, M., Jaeger, E., Lehner, I., … Teuling, A. (2010). Investigating soil moisture–climate interactions in a changing climate: a review. *Earth-Science Reviews*, *99*, 125–161. https://doi.org/10.1016/j.earscirev.2010.02.004

Sheffield, J., Camargo, S. J., Fu, R., Hu, Q., Jiang, X., Johnson, N., & Zhao, M. (2013). North American climate in CMIP5 experiments. Part II: Evaluation of historical simulations of intraseasonal to decadal variability. *Journal of Climate*, *26*, 9247–9290. https://doi.org/10.1175/JCLI-D-12-00593.1

Sippel, S., Zscheischler, J., Mahecha, M. D., Orth, R., Reichstein, M., Vogel, M., & Seneviratne, S. I. (2017). Refining multi-model projections of temperature extremes by evaluation against land-atmosphere coupling diagnostics. *Earth System Dynamics*, *8*, 387–403. https://doi.org/10.5194/esd-8-387-2017

Stegehuis, A. I., Teuling, A. J., Ciais, P., Vautard, R., & Jung, M. (2013). Future European temperature change uncertainties reduced by using land heat flux observations. *Geophysical Research Letters*, *40*, 2242–2245. https://doi.org/10.1002/grl.50404

Tawfik, A. B., Dirmeyer, P. A., & Santanello, J. A. (2015a). The heated condensation framework. Part I: Description and Southern Great Plains case study. *Journal of Hydrometeorology*, *16*, 1929–1945. https://doi.org/10.1175/JHM-D-14-0117.1

Tawfik, A. B., Dirmeyer, P. A., & Santanello, J. A. (2015b). The heated condensation framework. Part II: Climatological behavior of convective initiation and land-atmosphere coupling over the conterminous United States. *Journal of Hydrometeorology*, *16*, 1946–1961. https://doi.org/10.1175/JHM-D-14-0118.1

van den Dool, H. M. (1994). Searching for analogues, how long must we wait? *Tellus A*, *46*, 314–324. https://doi.org/10.1034/j.1600-0870.1994.t01-2-00006.x

Vogel, M. M., Orth, R., Cheruy, F., Hagemann, S., Lorenz, R., van den Hurk, B., & Seneviratne, S. (2017). Regional amplification of projected changes in extreme temperature strongly controlled by soil moisture-temperature feedbacks. *Geophysical Research Letters*, *44*, 1944–8007. https://doi.org/10.1002/2016GL071235

Wallace, J. M., Deser, C., Smoliak, B., & Phillips, A. (2015). Attribution of climate change in the presence of internal variability, In C.-P. Chang, et al. (Eds.), *Climate Change: Multidecadal and Beyond* (pp. 1–29). Singapore: World Scientific.

Wallace, J. M., Zhang, Y., & Renwick, J. A. (1995). Dynamic contribution to hemispheric mean temperature trends. *Science*, *270*, 780–783. https://doi.org/10.1126/science.270.5237.780

Yang, F., Kumar, A., & Lau, K. (2004). Potential predictability of US summer climate with perfect soil moisture. *Journal of Hydrometeorology*, *5*(5), 883–895. https://doi.org/10.1175/1525-7541(2004)005<0883:PPOUSC>2.0.CO;2

Zhang, J., Wang, W.-C., & Leung, L. R. (2008). Contribution of land-atmosphere coupling to summer climate variability over the contiguous United States. *Journal of Geophysical Research*, *113*, D22109. https://doi.org/10.1029/2008JD010136

Chapter 3, in full, is a reprint of the material as it appears in *Geophysical Research Letters*, 2017: Anna L. Merrifield, Flavio Lehner, Shang-Ping Xie, and Clara Deser, "Removing Circulation Effects to Assess Central U.S. Land-Atmosphere Interactions in the CESM Large Ensemble." The dissertation author was the primary investigator and author of this paper.

Chapter 4

Evaluation of Summer Dynamical Adjustment: Method Uncertainty and Sensitivity Analysis

4.1 Introduction

In Chapter 2, a method to remove the effects of circulation on summer surface air temperature (SAT) variability over North America was presented. This method, dynamical adjustment, performed on the Community Earth System Model version 1 (CESM1) Large Ensemble, was shown to reveal the central US as a region where SAT variability is influenced by both circulation and land surface processes in approximately equal measure (Merrifield et al., 2017). The central US is a well known "hot spot" of land-atmosphere interaction (e.g. Koster et al., 2004b,a, 2006; Dirmeyer, 2011; Berg et al., 2014), and the fact the hotspot region can be identified by a method that requires only temperature and pressure records is promising. SAT and sea level pressure (SLP) are among the most comprehensively measured atmospheric fields prior to the satellite era (Trenberth and Paolino, 1980). In contrast, land surface observations tend

to be both spatially and temporally limited (Seneviratne et al., 2010; Betts et al., 1996), which hinders understanding of the land surfaces' influence year-to-year on continental scales.

While summer dynamical adjustment has been shown to highlight a known hot spot of land-atmosphere interaction in CESM, the method requires further evaluation to determine its efficacy in an observational framework. The ideal circumstances for dynamical adjustment, which is an empirical method, can be achieved in a model framework. In observations, there are practical limitations to the method, mainly due to the length of observational records (van den Dool, 1994). Dynamical adjustment is conceptually similar to the analogue method of weather forecasting (Lorenz, 1969), but leverages the relationship between atmospheric circulation and SAT on monthly timescales rather than daily timescales. The method relies on the ability to reconstruct a monthly mean circulation field (e.g. July 2005), which will be represented in this chapter by SLP as in Deser et al. (2016), from a large set of analogues. In a model, the large set of SLP analogues can be selected from thousands of years of possible Julys in a control run (Lehner et al., 2017; Deser et al., 2016). In observations, SLP analogues must be selected from approximately 100 Julys in the observational record. This version of dynamical adjustment, referred to as the "leave-one-out" method, will be used in this chapter in order for conclusions to be applicable to observed dynamical adjustment. The name leave-one-out comes from the fact analogues come from the same record as the target month, therefore the target month must be excluded from the record prior to analogue selection.

It is important to acknowledge that because of the paucity of analogue choices in leave-one-out dynamical adjustment, the term "analogue" is a bit of a misnomer. The term evokes the idea of a match, though in practice, analogues may not closely resemble the target which is discussed in more detail in the following paragraph. For convenience, we will continue to refer to the months used in target SLP construction as "analogues", but we do so with the understanding that target and analogue patterns may differ over the selection domain.

A month is determined to be an analogue of the target month if the Euclidean distance

between target and analogue SLP is small. Euclidean distance is computed at each grid point and averaged over the domain 20-90°N, 180-10°W. This selection metric, therefore, does not require an analogue to match the target month spatially over the whole domain. This is necessary because, with O(100) possible options, it is statistically unlikely that a "perfect" analogue will exist for a particular target month. (van den Dool, 1994) found that it would take on the order of 10^{30} years to find two Northern hemisphere circulation patterns that match within observational uncertainty. With this in mind, a smaller than hemispheric domain (20-90°N, 180-10°W) and iterative averaging schemes are employed in dynamical adjustment to make the most of "imperfect" analogues available (Wallace et al., 2012; Deser et al., 2014, 2016).

Once the Euclidean distances are determined, the N_a closest SLP analogues are chosen, and the iterative process of selecting N_s of N_a SLP analogues and optimally reconstructing target SLP commences. For sections 3a-c of this chapter, we use $N_a = 80$ and $N_s = 50$, following Lehner et al. (2017). A sensitivity analysis to N_s is presented in section 3d. The optimal reconstruction of target SLP is mathematically equivalent to multivariate linear regression; each analogue is assigned a weight (β_i) such that a weighted linear combination of analogues produces a least-squares estimate of the target SLP. The analogue weighting scheme ensures that analogues which are further from (closer to) the target, in a Euclidean distance sense, contribute less (more) to the constructed SLP field.

Once SLP is constructed, the weights derived for each SLP analogue are applied to their corresponding monthly-averaged SAT fields. Prior to the application of weights, a quadratic trend representing anthropogenic warming is removed from the SAT record at each point in space. The purpose of this detrending is discussed in section 3c and in Deser et al. (2016). The weighted, detrended SAT fields are then used to construct a dynamic SAT anomaly field for the target month. SLP, which is a representative of low-level atmospheric circulation, and SAT are physically related; SLP-derived weights are applied to SAT to empirically construct that relationship. Conceptually, dynamic SAT anomalies are those that would occur given the

attendant circulation pattern. The second through fifth steps of dynamical adjustment (selection of N_s of N_a SLP analogues, optimal reconstruction of target SLP, and construction of dynamic SAT) are then repeated N_r times. In this chapter, $N_r = 100$, following Lehner et al. (2017). The dynamic component of SAT in the target month is the average of the N_r constructions.

Once dynamic SAT has been determined, residual SAT is computed as the difference between total and dynamic SAT for each month. By removing the effect of circulation from total SAT, residual SAT is believed to reflect the influence of thermodynamic processes associated with the state of the land surface (Deser et al., 2016; Lehner et al., 2017). In winter, a lack of snow cover or sea ice in Hudson Bay may induce a residual warm anomaly due to the reduction of albedo (Deser et al., 1993). In summer, a lack of soil moisture in a land-atmosphere hot spot region may cause a residual warm anomaly due to an enhanced sensible heat flux (Seneviratne et al., 2010; Miralles et al., 2012). Over North America, residual SAT anomalies are relatively small in comparison to dynamic SAT anomalies in boreal winter (December-January-February; DJF). In boreal summer (June-July-August; JJA), however, residual SAT anomalies are often as large as dynamic SAT anomalies.

There are several possible explanations for the difference in relative magnitude of residual SAT between DJF and JJA. Residual SAT anomalies arise from either physical processes (i.e. surface feedbacks due to snow cover or soil moisture), methodological error, or a combination of the two. In DJF, conditions are conducive for the dynamic SAT to be the dominant component of total SAT and residual SAT to be minimal. Physically, horizontal advection at the surface sets SAT, while the westerly jets, maintained by the hemispheric meridional temperature gradient, advect barotropic planetary waves that set SLP patterns over North America (e.g. Hurrell, 2015; Sheffield et al., 2013; Deser et al., 2014). Methodologically, the strength and organized structure of winter tropical-extratropical teleconnections (e.g. Seager et al., 2003; Kushnir et al., 2010; Zhou et al., 2014) allow for plenty of close SLP analogues choices. These three ingredients: (1) close analogues available to construct SLP patterns, (2) SLP representing the large-scale

circulation and (3) the influence of large-scale circulation on SAT, combine to ensure DJF dynamic SAT is accurately represented as the dominant component of SAT variability.

In JJA, conditions allow residual SAT to reach a maximum. Physically, radiation throughout the summer hemisphere weakens the meridional temperature gradient, which weakens the zonal mean zonal wind and diminishes the amplitude of both free tropospheric and quasistationary Rossby waves that govern midlatitude climate (Petoukhov et al., 2013; Coumou et al., 2015). In conjunction with an overall weakening of atmospheric circulation in the summer, SLP over the North American continent can be influenced by thermally-induced features (Fast and McCorcle, 1991; Johnson, 2003) that introduce baroclinicity beneath large-scale disturbances. Locally-influenced SLP patterns are spatially concomitant with SAT, which is different from the out of phase relationship associated with frontal systems. Finally, as previously described, land surface processes can modify summer SAT (Seneviratne et al., 2010). Therefore, residual summer SAT may stem from methodological challenges (an inability to reconstruct SLP patterns, inconsistent relationships between SLP and the large-scale circulation, and SLP and SAT) as well as thermodynamic processes.

By evaluating summer dynamical adjustment, we aim to determine if residual SAT is representative of the land surface feedback, as posited in Merrifield et al. (2017), or is representative of methodological shortcomings, which are in part due to the nature of summer dynamics. We address three aspects of summer dynamical adjustment in this chapter. First, we obtain an estimate of the fraction of residual SAT that is due to intrinsic method uncertainty vs. land surface processes. Second, we determine if land surface processes in analogues contribute to and "contaminate" dynamic SAT. Third, we document sensitivities of summer dynamical adjustment to analogue selection period and the number of analogues selected. Implications for the potential observational application of summer dynamical adjustment is discussed in section 4. Findings from this method evaluation are summarized in section 5.

4.2 Global Land Atmosphere Coupling Experiment-Coupled Model Intercomparison Project (GLACE-CMIP5)

The Global Land Atmosphere Coupling Experiment-Coupled Model Intercomparison Project (GLACE-CMIP5) is a coordinated effort by several modeling centers to investigate the role of soil moisture in a changing climate system (Seneviratne et al., 2013). The GLACE-CMIP5 framework is an extension of the GLACE model intercomparison study initiated by Randal Koster (Koster et al., 2004a, 2006; Guo et al., 2006), which assessed the global land-atmosphere coupling in boreal summer, identifying regions where models agreed that land surface anomalies affect temperature and precipitation.

In GLACE, two simulations are compared: the first with interactive soil moisture (hereafter, CTL) and the second with prescribed soil moisture (hereafter, SMclim following Lorenz et al. (2016)). SMclim is equivalent to expA in Seneviratne et al. (2013). The two simulations otherwise have the same configuration; identical sea surface temperatures (SST), sea ice, land use, and CO_2 concentrations are prescribed (Seneviratne et al., 2013). This setup isolates the influence of soil moisture variability on surface climate, provided that each simulation has similar internal atmospheric variability.

In this chapter, we use the National Center of Atmospheric Research (NCAR) contribution to GLACE-CMIP5 (hereafter "CESM GLACE") to evaluate summer dynamical adjustment (Neale et al., 2013; Lawrence et al., 2011). Using CESM GLACE allows us to assess the validity of conclusions made using the CESM1 Large Ensemble in Merrifield et al. (2017). CESM GLACE and the CESM1 Large Ensemble use the same Community Land Model (CLM4), but CESM GLACE uses an older version of the Community Atmospheric Model (CAM4 vs. CAM5) (Meehl et al., 2013). The two simulations we are considering are the CTL simulation, which is the r6i1p1 contribution to CMIP5, and the SMclim simulation, which has prescribed climatological soil moisture computed from the CTL simulation (Seneviratne et al., 2013). Climatological soil

moisture is from computed in terms of monthly averages over the 1971-2000 reference period and resulting seasonal cycle is imposed by interpolating between the midpoints of the adjacent months at each simulation timestep (Berg et al., 2017). Time-evolving SST, sea ice, land use from the CTL simulation are also prescribed in SMclim. The two runs both experience historical (1950-2005) and RCP8.5 (2006-2100) forcing scenarios, as per the CMIP5 protocol (Taylor et al., 2012). We focus on the historical period in this chapter, as in Merrifield et al. (2017).

4.3 Dynamical Adjustment of the CESM GLACE Simulation

Several aspects of summer dynamical adjustment can be evaluated by dynamically adjusting the CESM GLACE simulations. The first two evaluation opportunities stem from the difference in land-atmosphere coupling in the CTL and SMclim simulations. Interannual variability of JJA SAT, the latent heat flux, and soil moisture over the historical period are shown for the CTL and SMclim simulations in Figure 4.1, a-f. The three fields are involved in the canonical land-atmosphere coupling, where the presence or absence of soil moisture partitions the surface turbulent heat flux to either cool or warm SAT (Seneviratne et al., 2010; Dirmeyer, 2011; Berg et al., 2014). The central US stands out as a region where soil moisture, latent heat, and SAT vary in the CTL simulation and do not in SMclim. With soil moisture, this difference in variability is by construction (SMclim soil moisture is prescribed to climatological values). A timeseries of monthly mean soil moisture at 36.28°N, 103.75°W is shown for CTL (black) and SMclim (red) in Figure 4.1 g. Because an interactive (passive) land surface induces (suppresses) SAT variability in the central US, the region is identified as a land-atmosphere hot spot (Koster et al., 2004a).

A schematic midlatitude cross-section, shown in Figure 4.2, helps to illustrate the opportunities for evaluating dynamical adjustment afforded by SMclim. In both CTL (Figure 4.2, left) and SMclim (Figure 4.2, right), atmospheric circulation patterns (black contours) establish

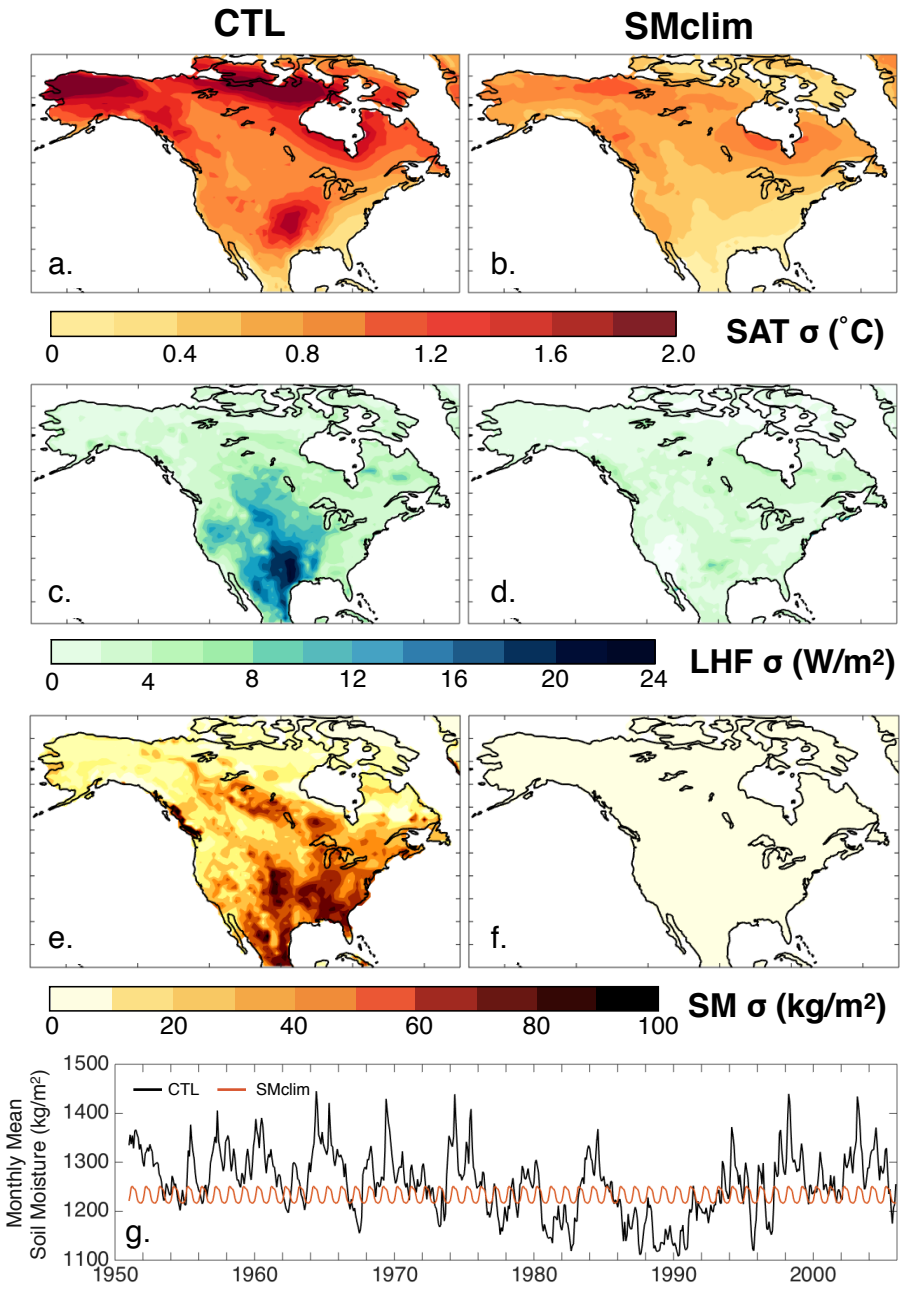

Figure 4.1: (a-f) Standard deviations (σ) of June-July-August (JJA) fields and (g) monthly mean soil moisture at a grid point (36.28°N, 103.75°W) in the CESM GLACE simulations. (a,b) SAT (°C) and (c,d) latent heat fluxes (LHF; W/m^2) vary notably more year-to-year in the central US in the CTL simulation than in SMclim. This difference is understood to result from the absence of interannual soil moisture variability (kg/m^2) in SMclim (f).

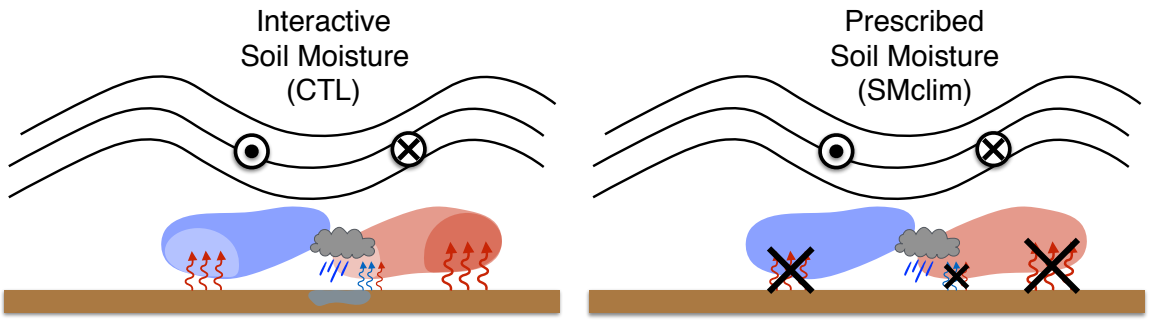

Figure 4.2: Schematic representation of the GLACE experiments evaluated. (left) In the control simulation (CTL), atmospheric circulation patterns establish SAT anomalies that are modified by surface fluxes partitioned by the presence or absence of soil moisture. (right) In the prescribed soil moisture simulation (SMclim), soil moisture is set to climatological values (computed as the 1971-2000 average), severing the land surface feedback on SAT (Seneviratne et al., 2013).

SAT anomalies (color); the schematic represents an idealized ridge-trough pattern that sets up a cooler northerly flow and warmer southerly flow. In the CTL simulation, the SAT anomalies are modified by surface fluxes (arrows), which are themselves modified by radiation availability and the presence or absence of soil moisture. Rainfall, which tends to accompany southerly flows, moistens soils and limits incoming shortwave radiation (due to an increase in cloud cover). The presence of soil moisture partitions outgoing surface energy into the latent heat flux (blue arrows), which serves to damp the warm SAT anomaly set by circulation. In regions with clearer skies and drier soils, outgoing surface energy warms SAT through the sensible heat flux (red arrows), notably amplifying the warm SAT anomaly.

Ideally, dynamical adjustment will characterize the dynamic SAT as the anomalies that are due to the attendant circulation pattern, but will not capture the amplification or damping contributed by the land surface feedback. The removal of dynamic SAT anomalies from total SAT would then reveal residual SAT anomalies that reflect this land surface influence. In practice, residual SAT anomalies reflect method uncertainty and thermodynamic processes that have not been accounted for in addition to the thermodynamic contribution of the land surface feedback. While a thermodynamic narrative can be developed for residual SAT anomalies (i.e. a warm

anomaly is related to an enhancement of the sensible heat flux due to drier than average soils), there is no formal way to separate physical contributions to residual SAT from methodological uncertainty in the CTL simulation.

In order to quantify the magnitude of method uncertainty, we evaluate a model simulation (SMclim) that does not have a land surface feedback. In the SMclim simulation, there are no soil moisture anomalies to partition surface fluxes (by design). The lack of anomalous soil moisture suppresses surface flux variation and severs the land surface feedback (black x's). Therefore, SAT anomalies in SMclim should be largely dynamic in nature and residual SAT anomalies should reflect method uncertainty, which includes the uncertainty associated with the empirical construction of the dynamic SAT and uncertainty associated with thermodynamic processes that have not been accounted for.

4.3.1 Quantifying Method Uncertainty

While this chapter focuses on summer dynamical adjustment, method uncertainty is estimated in all seasons for comparison purposes and to inform future applications of dynamical adjustment. Method uncertainty is determined through leave-one-out dynamical adjustment on SMclim. Because method uncertainty is heterogeneous over the domain, four regions of North America are considered with regional boundaries shown in Figure 4.3. The regions are based on CESM's orography (Figure 4.3, color) and magnitude of seasonally-averaged SAT variability in SMclim, which is shown in terms of standard deviation (σ; °C) scaled by domain average standard deviation of total SAT (σ_{mean}; °C) in Figure 4.4. The North region (Figure 4.3, "N") includes most of Canada and Alaska. The US and Northern Mexico are split into three regions with the West region (Figure 4.3, "W") covering the majority of the North American Cordillera, the Central region (Figure 4.3, "C") covering the US Great Plains, and the East region (Figure 4.3, "E") covering the US East Coast.

Throughout this chapter, the dynamic and residual components of SAT derived from

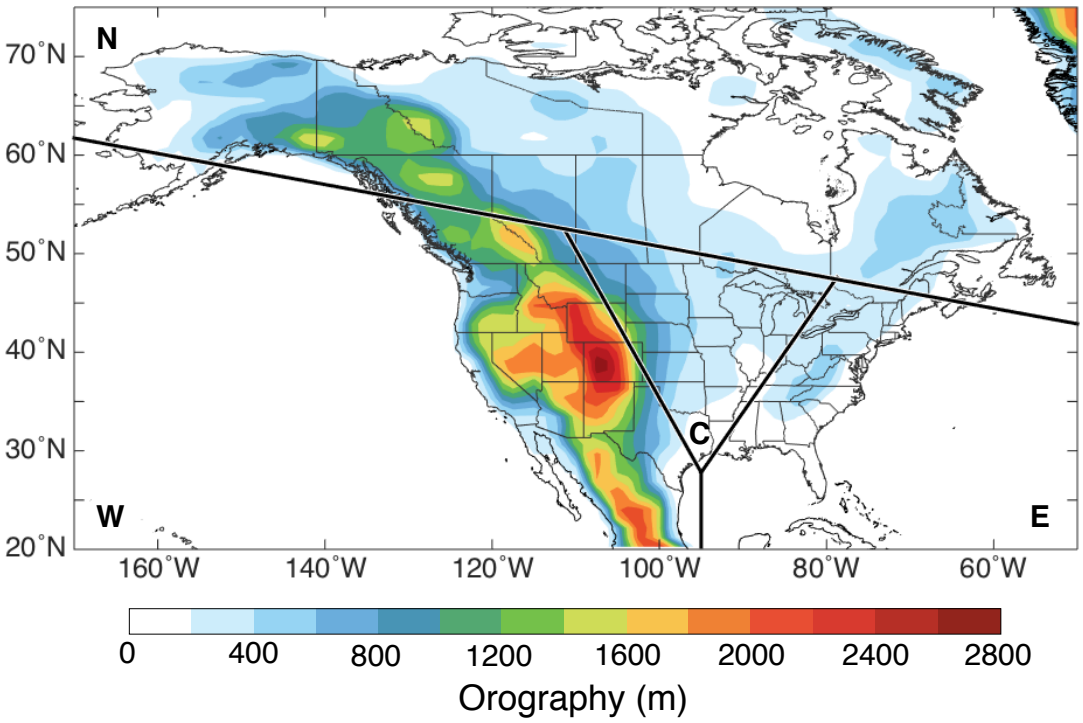

Figure 4.3: Four regions used in the study: North (N), which includes most of Canada and Alaska, West (W), which includes the western mountain ranges, Central (C), which includes the US Great Plains, and East (E), which covers the US East Coast. Boundaries are superposed on CESM's orography (color; m above the geiod).

dynamical adjustment will be presented in terms of standard deviation. This provides a general measure of the contribution of circulation to interannual SAT variability (dynamic) and, in the case of SMclim, the uncertainty associated with dynamical adjustment (residual). Total (i), dynamic (ii), and residual (iii) North American SAT variability are shown for boreal winter (DJF; a), spring (MAM; b), summer (JJA; c), and fall (SON; d) in Figure 4.4. To allow for comparison across seasons, each variability map is divided by the domain-averaged standard deviation of total SAT (σ_{mean}) at each grid point, given for each season in the top left of Figure 4.4 panels a-d. i.

SMclim SAT variability is largest in DJF (Figure 4.4 a.i) and smallest in JJA (Figure 4.4 c.i), with maximum absolute magnitudes exceeding 4°C and less than 1.4°C respectively. In all seasons, variability is largest in the North, where SAT fluctuations are associated with the strength and location of the polar jet (Lewis, 2003). Dynamic SMclim SAT variability, empirically constructed through dynamical adjustment, is shown in Figure 4.4 a-d ii. In terms of spatial pattern, dynamic SAT variability resembles total SAT variability in all seasons, which supports our hypothesis that SAT variability is largely dynamic in nature in SMclim. In terms of magnitude, dynamic SAT variability is not as large as total SAT variability, particularly in the North region. In DJF, total SAT variability exceeds dynamic SAT variability by approximately 0.5 – 1°C in absolute magnitude. Residual SMclim SAT variability (Figure 4.4 a-d iii) is non-zero in SMclim and is on the order of 0.5°C in all seasons. Relative to σ_{mean}, residual SAT variability is approximately twice as large in JJA than it is in DJF. This suggests that some of the method uncertainty is due to the seasonal difference in the strength and structure of atmospheric circulation. Due to the spatial similarity of total and dynamic SAT variability, residual SAT variability does not share regional maxima with total SAT variability. The relative magnitude of residual SAT variability in each region is presented in terms of percent of total SAT variance explained by residual SAT in Figure 4.5.

The dynamical adjustment of SMclim allows us to quantify method uncertainty in terms of residual SAT variability. Ultimately, this definition of method uncertainty will help us to

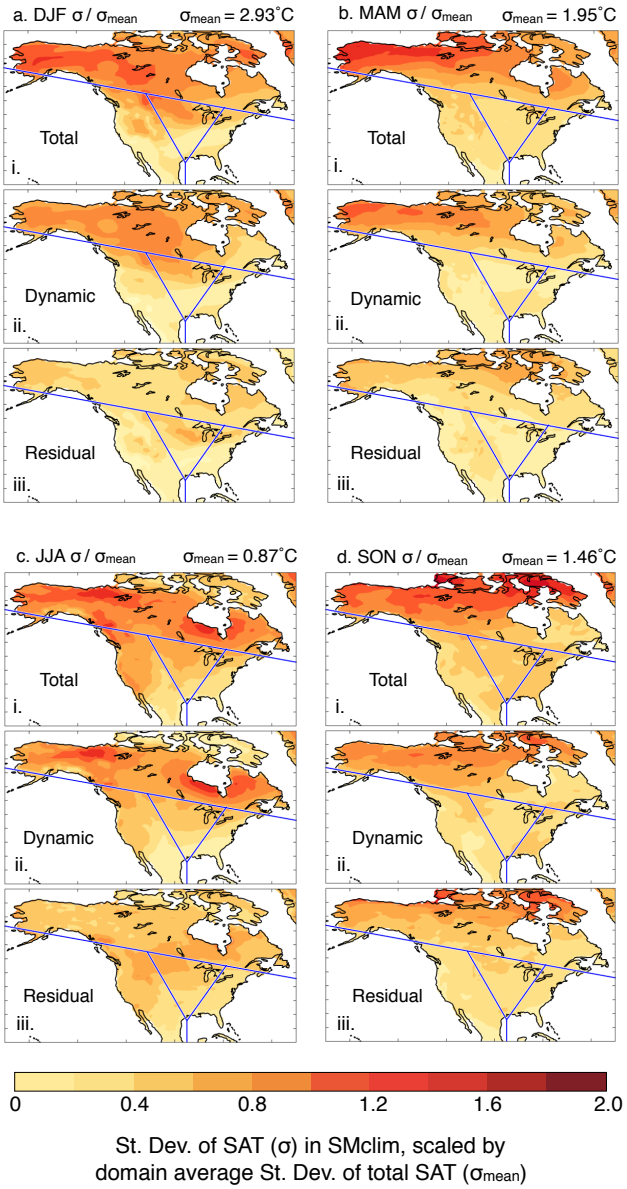

Figure 4.4: Standard deviations (σ; °C) of seasonally-averaged SMclim SAT and its components, scaled by the domain average standard deviation of total SAT (σ_{mean}; °C).

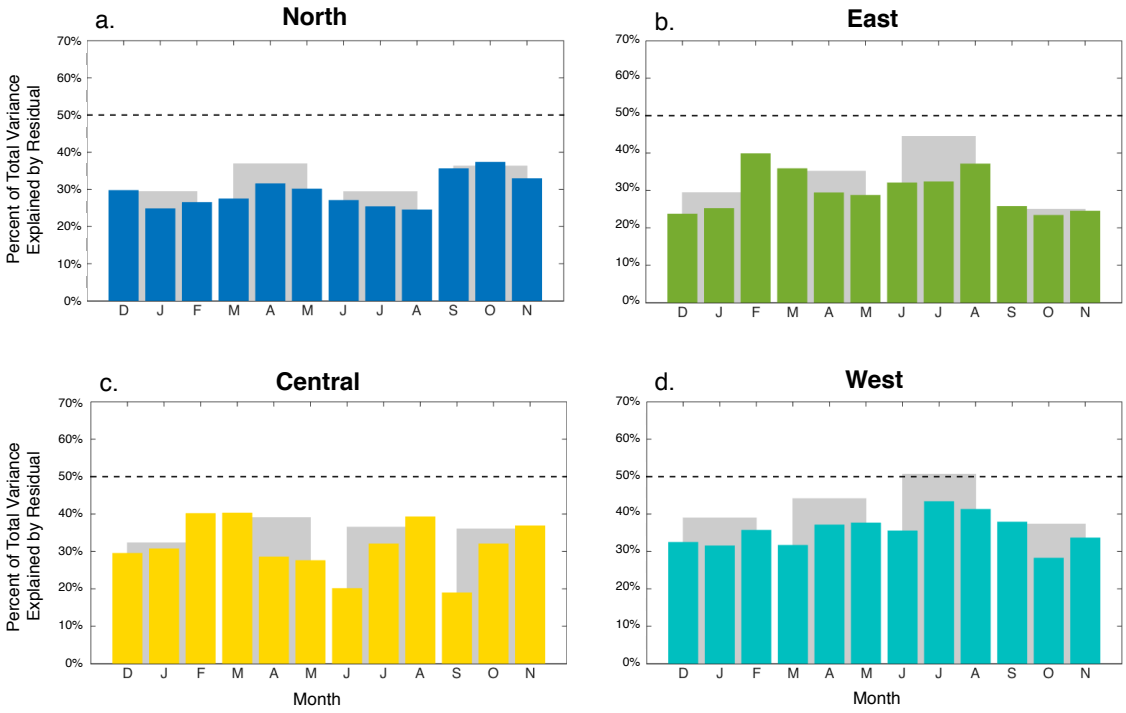

Figure 4.5: Percent of total SAT variance explained by residual SAT in SMclim, averaged over the four regions shown in Figure 4.3. Colored bars show the percent of monthly mean variance explained. Gray bars show the percent of seasonally-averaged (DJF, MAM, JJA, and SON) variance explained. The criteria used to define hot spot SAT in Merrifield et al. (2017), residual SAT explains $\geq$ 50% of total SAT variance, is shown as a dashed line.

formalize a residual SAT-based land-atmosphere hot spot metric. In Merrifield et al. (2017), we defined the land-atmosphere hot spot as a region where residual SAT explains ≥ 50% of total SAT variance (Figure 4.5, dashed black line). The 50% variance explained threshold identified (ruled out) the central (western) US as a land-atmosphere hot spot region, which was in line with the finding of others (e.g. Koster et al., 2004a; Findell and Eltahir, 2003b). However, there was no way to definitively verify that exceedance of the 50% threshold was not due to large method uncertainty. If this is the case, our hot spot definition is not identifying regions where land surface processes contribute to SAT variability, rather it likely identifies regions where dynamic SAT isn't being effectively characterized. Because the SMclim residual reflects method error, we can use it to determine the point at which we confidently attribute residual SAT variance to physical processes.

For comparison with the land-atmosphere hot spot threshold, we define method uncertainty as the percent of total SAT variance explained by residual SAT. Percent variance explained is computed using linearly detrended monthly-averaged (Figure 4.5, colored bars) and seasonally-averaged (Figure 4.5, gray bars) SAT records at each grid point, which are subsequently area-averaged over the regions shown in Figure 4.3. Method uncertainty falls below the hot spot requirement of ≥ 50% every month in an aggregate sense, but not necessarily at each grid point in space (not shown). Notable exceptions in JJA include the Canadian Arctic north of 70°N and regions south of 40°N in the West, East, and Central regions. In both exceptional regions, total SAT variability is relatively low, less than 0.75°C. This suggests that method uncertainty becomes larger when total SAT variability approaches zero. It also excludes potential hot spot regions from being exceptional in terms of method uncertainty, as hot spot regions tend to have relatively large variability.

In the North region (Figure 4.5 a), method uncertainty ranges between a minimum of 24% in August to a maximum of 37% in October. Seasonally-averaged method uncertainty is about 7% larger in MAM (37%) and SON (36%) during the warm-cold seasonal transitions than

in DJF and JJA (29%). In the East region (Figure 4.5 b), method uncertainty ranges between a minimum of 23% (October) and a maximum of 40% (February). JJA method uncertainty in the East is relatively large (44%), but this again is likely due to minimal total SAT variability in the region ($< 0.5°C$) more than it is due to issues with dynamical adjustment.

In the Central region (Figure 4.5 c), method uncertainty is at a minimum in September (19%) and at a maximum in March (40%). Uncertainty approximately doubles from June (20%) to August (39%), resulting in JJA method uncertainty of 37% which must be exceeded for SAT variability to be ascribed to the land surface feedback. JJA method uncertainty in the hot spot region defined in Merrifield et al. (2017) (32.5-41.9°N, 90-98.7°W) is 43% (not shown). This level of hot spot method uncertainty supports the conclusion that hot spot SAT variability is land surface driven in the CESM large ensemble.

In the West region (Figure 4.5 d), method uncertainty ranges between 28% (October) and 43% (July). Seasonally, however, the hot spot requirement (residual SAT explaining $\geq$ 50% of total SAT variance) is exceeded in JJA. We posit this is due to the regions' complex topography. Because SLP is a derived and somewhat noisy quantity at altitude (Jeff Strong, personal comm.), it may not characterize dynamic SAT anomalies as well as it does at altitudes closer to sea level, thus leaving behind larger residual SAT that explains more total SAT variance. In Merrifield et al. (2017), this hypothesis was supported by comparing dynamical adjustment using the 500mb height field (Z500) as an indicator of circulation to the traditional method of using SLP. While Z500 may be a superior choice of circulation indicator for summer dynamical adjustment, we do not evaluate it here because it cannot be used for observational dynamical adjustment due to lack of direct observations before 1948 (Kalnay et al., 1996). Further, Z500 is not suitable for GLACE dynamical adjustment because analogues are selected from the 1951-2100 period over which Z500 is subject to forced change due to atmospheric expansion. Issues associated with forced changes in analogues are further discussed in section 3c.

Regardless of limitations, method uncertainty remains at approximately 20-45% in all

regions and seasons. This threshold does not prohibit the use of leave-one-out dynamical adjustment to define hot spots of land surface driven variability, as residual SAT variability in excess of 45% may therefore be attributed to thermodynamic land surface processes. However, we recommend that care be taken in interpreting residual SAT in regions where total SAT variability is less than 0.75°C and over altitudes of approximately 1000 m or more above sea level.

4.3.2 Interactive vs. Fixed Soil Moisture Analogues

The CESM GLACE simulations also can be used to assess the potential contribution of the land surface feedback to the constructed dynamic component of SAT. This "thermodynamic contamination" arises from the existence of the land surface feedback in analogues. In theory, each analogue has different land surface conditions. The iterative random selection process then samples the distribution and after averaging, provides a dynamic component that is not influenced by the state of the land surface in any particular analogue. In practice, analogues of a particular target month may share similar land surface states i.e. analogues featuring a persistent blocking high may also share drier than average soil conditions. It is also possible that a particular analogue with a strong SAT anomaly that is related to the state of the land surface may be selected multiple times and may thus bias dynamic SAT.

Possible thermodynamic contamination can be assessed through dynamical adjustment of the CESM GLACE CTL simulation. Two CTL simulation adjustments are performed. The first is a leave-one-out dynamical adjustment using analogues selected from the CTL simulation with interactive soil moisture. The second is a dynamical adjustment using analogues selected from SMclim with fixed soil moisture. Unlike CTL simulation analogues, SMclim analogues have no land surface feedback to contaminate dynamic SAT. If there is no thermodynamic contamination by CTL run analogues, both methods will have similar dynamic SAT.

Before the CTL simulation dynamical adjustments are performed, we verify that the CTL and SMclim simulations have statistically similar SLP patterns. This ensures that analogues

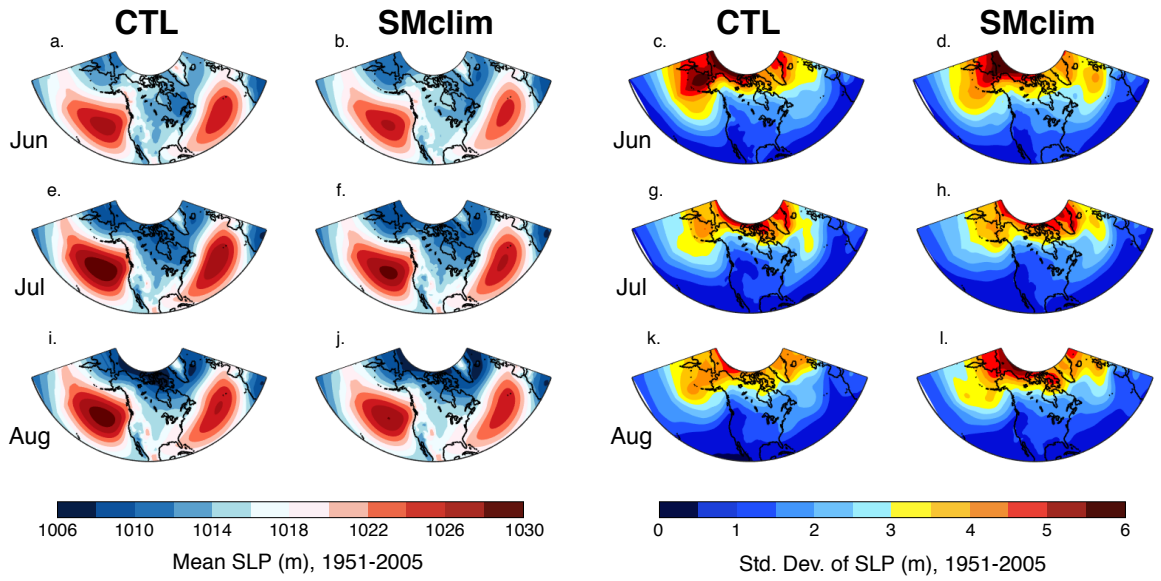

Figure 4.6: Climatology and variability of SLP (m) over the historical forcing period (1951-2005) in June (a-d), July (e-h), and August (i-l) for the CTL and SMclim simulations.

of CTL SLP can be found in SMclim simulation. A comparison of the June (a-d), July (e-h), and August (i-l) SLP historical period means and standard deviations are shown in Figure 4.6. The CTL and SMclim simulations have very similar mean state SLP throughout the summer, featuring the semi-permanent North Pacific and North Atlantic Subtropical highs (Davis et al., 1997; Nigam and Ruiz-Barradas, 2006; Li et al., 2011) and lower pressure at high latitudes that extends into the central US. The high pressure centers are slightly larger in magnitude in the CTL simulation (Figure 4.6 a,e,i) than SMclim (Figure 4.6 b,f,j), but otherwise the two experiments have near equivalent climatology. CTL and SMclim also have similar SLP variability patterns, with a general meridional increase in variability and a higher (lower) variability excursion on the northern (western) edge of the North Pacific high. The main spatial difference in SLP variability occurs on the northern edge of the North Atlantic Subtropical High in June (Figure 4.6 c,d) and August (Figure 4.6 k,l).

Beyond means and standard deviations, CTL and SMclim have statistically similar modes of SLP variability determined through empirical orthogonal function (EOF) analysis. Figure 4.7

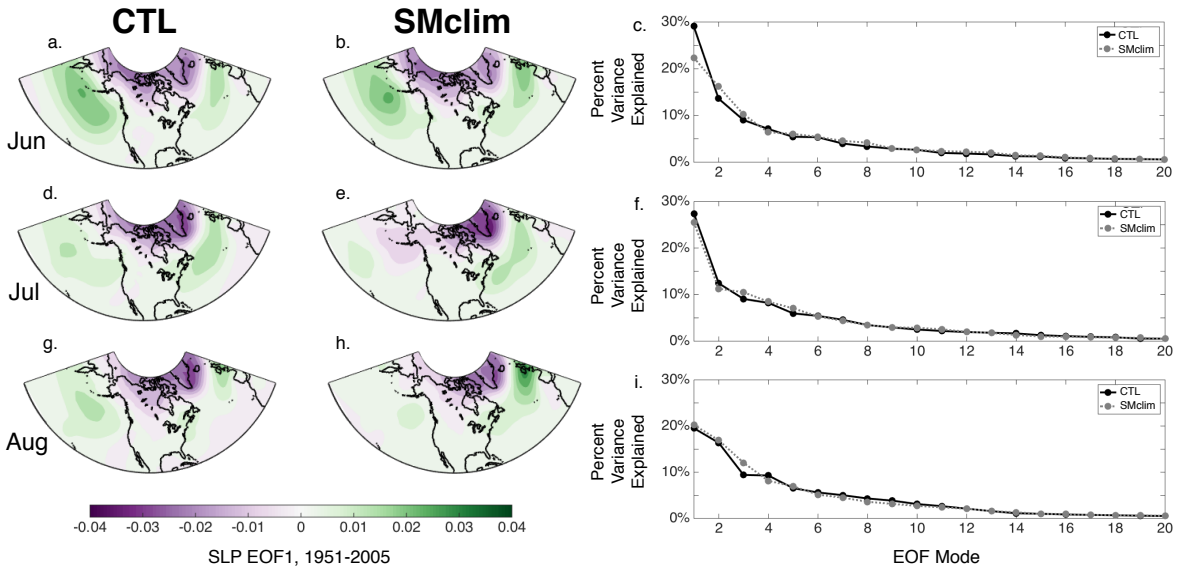

Figure 4.7: SLP Empirical Orthogonal Function (EOF) mode 1 in the CTL (a,d,g) and SMclim (b,e,h) simulations are similar in June, July and August. (c,f,i) The CTL (black solid line) and SMclim (gray dashed line) simulations also have subsequent EOF modes that explain similar amount of SLP variance.

shows SLP EOF1 spatial modes and the percent variance explained by SLP EOF modes 1-20 for the CTL and SMclim simulations. In June (Figure 4.7 a-c), SLP EOF1 is spatially similar for CTL and SMclim, but the mode explains about 4% less of the total SLP variance in SMclim than it does in CTL. In July (Figure 4.7 d-f), CTL and SMclim SLP EOF1 differ in sign over Alaska and in magnitude over Greenland, but are near identical in terms of percent variance explained by EOF1 and subsequent modes. In August (Figure 4.7 g-i), spatial differences in CTL and SMclim SLP EOF1 occur over the North Pacific and North Atlantic, but as in July, percent variance explained is nearly identical in both simulations.

Because CTL and SMclim SLP patterns are similar, the two dynamical adjustments necessary to detect thermodynamic contamination can be performed. We compare the dynamic component of SAT variability constructed using CTL analogues (i) with the dynamic component constructed using SMclim analogues (ii) for each season in Figure 4.8. There is little difference between the CTL and SMclim-derived dynamic components of SAT variability in boreal winter,

spring, and fall (Figure 4.8 a,b,d). The similarity indicates that the land surface feedback does not contribute to the dynamic component in these seasons. In JJA, however, CTL-derived dynamic SAT variability (Figure 4.8 ci) features a region of variability in the southern central US that is 0.7°C larger than dynamic SAT variability constructed with SMclim analogues (Figure 4.8 cii). Furthermore, the region is the same shape and in the same location as the region where total SAT variability is elevated by the active land surface feedback in CTL as compared to SMclim (Figure 4.1 a,b).

To explore this evidence of thermodynamic contamination, we select a July from the CTL simulation which features an SAT anomaly in the central US and thus contributes to the elevated total JJA SAT variability in the region. Total SAT (°C; color) and SLP (m; contours) anomalies in July 1996 are shown in Figure 4.9 a. SAT is approximately 4°C warmer than the historical period average in the central US, but there is no accompanying local SLP anomaly that would direct analogue selection and favor a dynamic SAT anomaly in the region. Therefore, the warm SAT anomaly should not be captured by dynamical adjustment. A dynamic SAT anomaly in the region would likely result from thermodynamic contamination by the land surface feedback in analogues. This is borne out when the July 1996 dynamic SAT anomaly constructed using CTL analogues (Figure 4.9 b) is compared to the July 1996 dynamic SAT anomaly constructed using SMclim analogues (Figure 4.9 c). With an active land surface feedback in the analogues (Figure 4.9 b), there is a warm anomaly in the dynamic component. Without an active land surface feedback in the analogues (Figure 4.9 c), there is no warm anomaly in the central US in dynamic SAT. The difference suggests thermodynamic contamination; CTL simulation analogues tend to have large SAT anomalies in the central US which contribute to dynamic SAT even when anomalous SAT is not necessitated by circulation.

The thermodynamic contamination hypothesis is further supported by assessing the land surface conditions in two Julys with similar atmospheric circulation, but different land surface states. A SMclim July, commensurate to July 1996 in the CTL simulation, was selected through

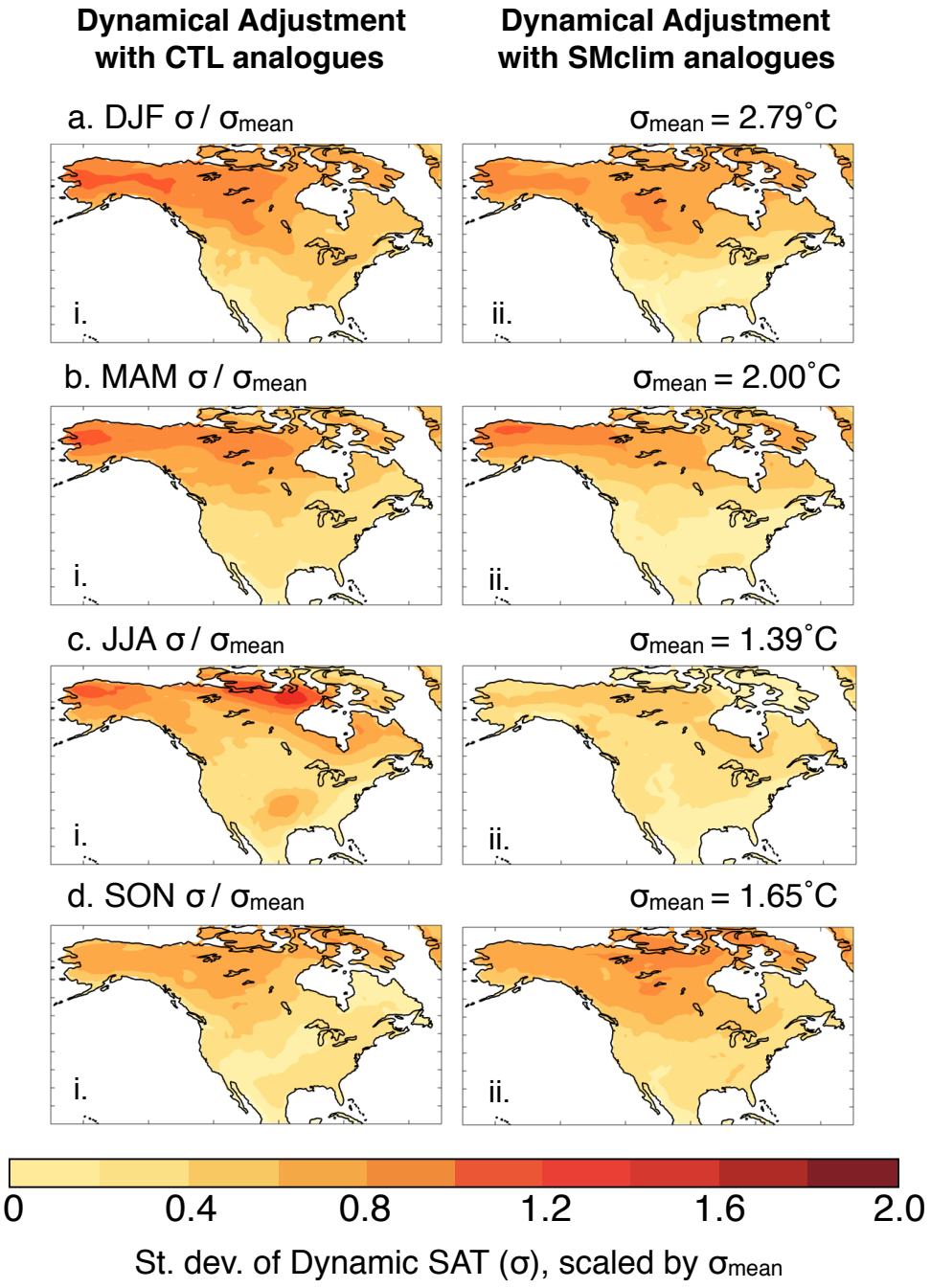

Figure 4.8: Standard deviations (σ; °C) of the seasonally-averaged dynamic component of CTL SAT, scaled by the domain average standard deviation of total SAT (σ_{mean}; °C). Panels a-d i (ii) show CTL dynamic SAT variability computed from dynamical adjustment using analogues from CTL (SMclim).

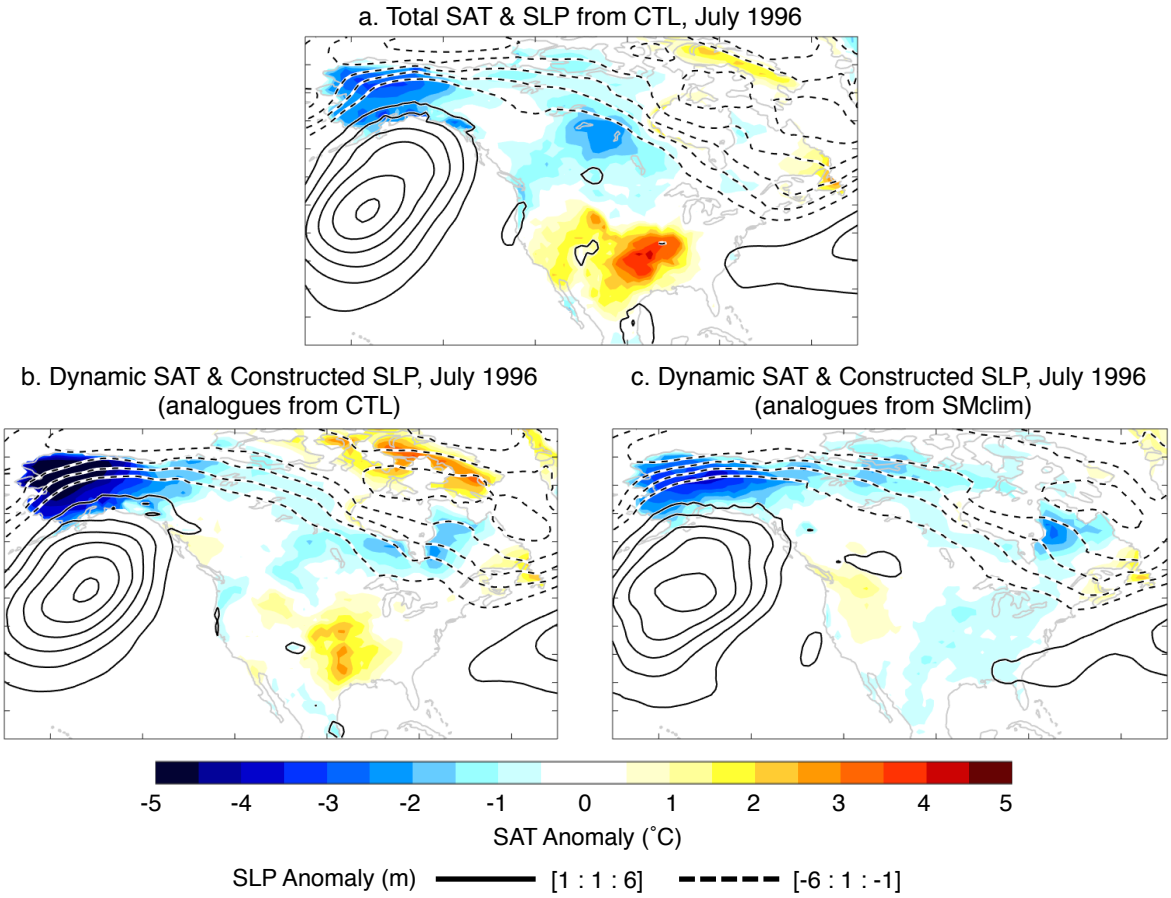

Figure 4.9: (a) July 1996 total SAT (°C) and SLP (m) anomalies in CTL. (b) July 1996 dynamic SAT (°C) and SLP (m) constructed using analogues from CTL. (c) July 1996 dynamic SAT (°C) and SLP (m) constructed using analogues from SMclim.

spatial correlation of Z500 anomaly fields, which are shown in contours in Figure 4.10 a and b. Z500, as opposed to SLP, is used for case selection because Z500 is anomalous locally over the central US, whereas SLP is not.

Differences in the Z500 fields of the two cases demonstrate that it is challenging to find a "perfect" analogue of a particular circulation pattern. July 1965 in SMclim was selected because it featured a center of action over the central US and midlatitude - high latitude pressure dipole over most of the domain as in July 1996 in the CTL simulation, but the two Julys are actually negatively correlated. For comparison purposes, the negative of July 1965 Z500 and SAT anomalies are shown in Figure 4.10 b.

Both cases feature Z500 anomalies of similar magnitude that are spatially concomitant with SAT in the central US, but the maximum anomaly in CTL July 1996 is 2°C than hotter than the (negative) maximum anomaly in SMclim July 1965. This difference in SAT is physically consistent with the difference in sensible heat flux anomalies in the two cases (Figure 4.10 c,d). Sensible heat flux anomalies represent the energetic pathway through which soil moisture can influence SAT (Seneviratne et al., 2010). July 1965 has no soil moisture anomalies by design (Figure 4.10 f), and a slightly negative sensible heat flux anomaly which may contribute somewhat to the 2°C difference in central US SAT anomalies (Figure 4.10 d). July 1996 does have drier than average soil conditions (Figure 4.10 e) in the vicinity of the central US SAT and sensible heat flux anomalies, but the soil moisture anomalies are not exceptional over the record (not shown). The relatively large sensible heat flux response to a relatively small soil moisture anomaly suggests that the atmosphere is very sensitive to land surface perturbations in the central US in CESM (Merrifield and Xie, 2016).

Anomalies in Figure 4.10 confirm that heat flux anomalies resulting from soil moisture variability underpin SAT anomalies in the central US in the CTL simulation. Though the land surface influence in CTL analogues does thermodynamically contaminate dynamic SAT somewhat, there is no observed equivalent to SMclim from which analogues can be picked.

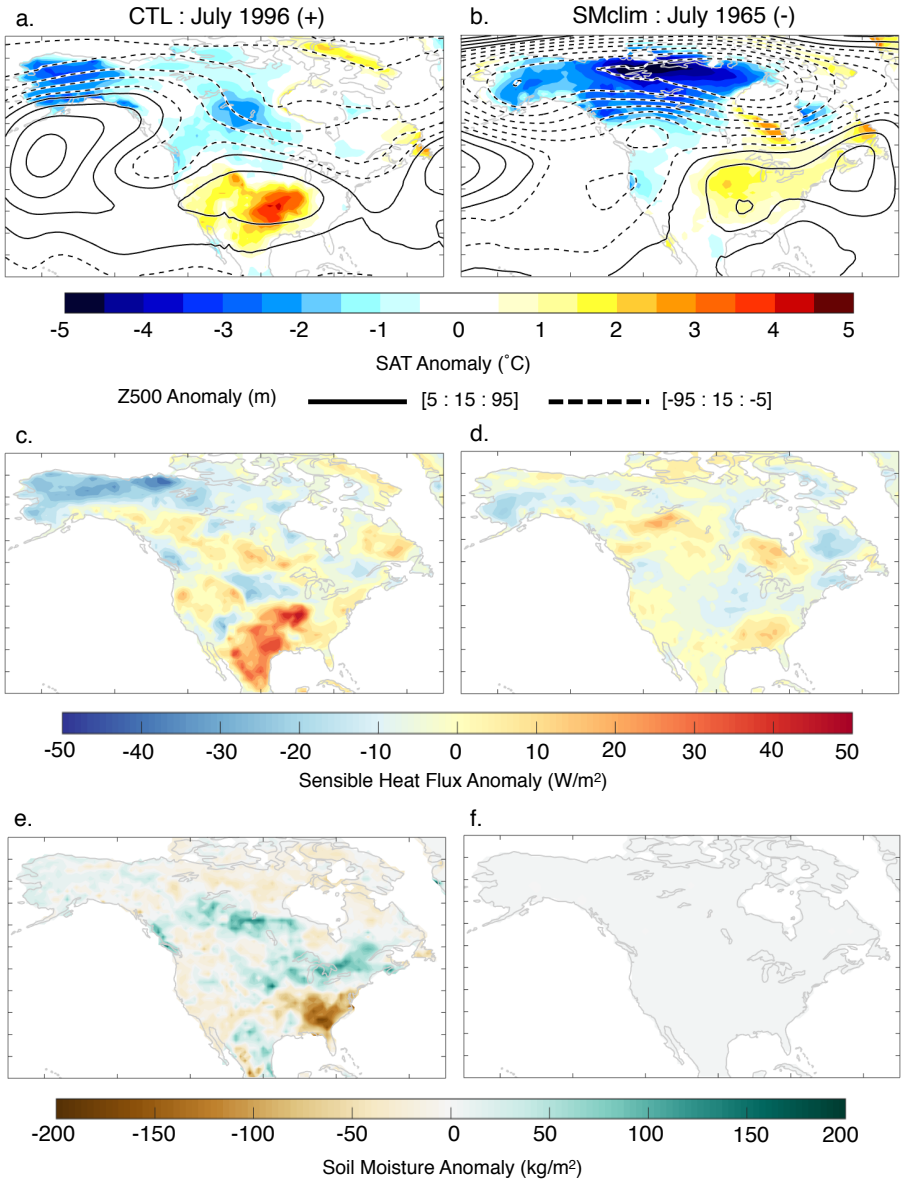

Figure 4.10: Total SAT (°C; color) and Z500 (m; contours) anomalies for (a) July 1996 in CTL and (b) July 1965 in SMclim, shown with the opposite sign for comparison purposes. Sensible heat flux (W/m^2) and soil moisture (kg/m^2) anomalies for the two Julys are shown in panels c, d and e,f respectively.

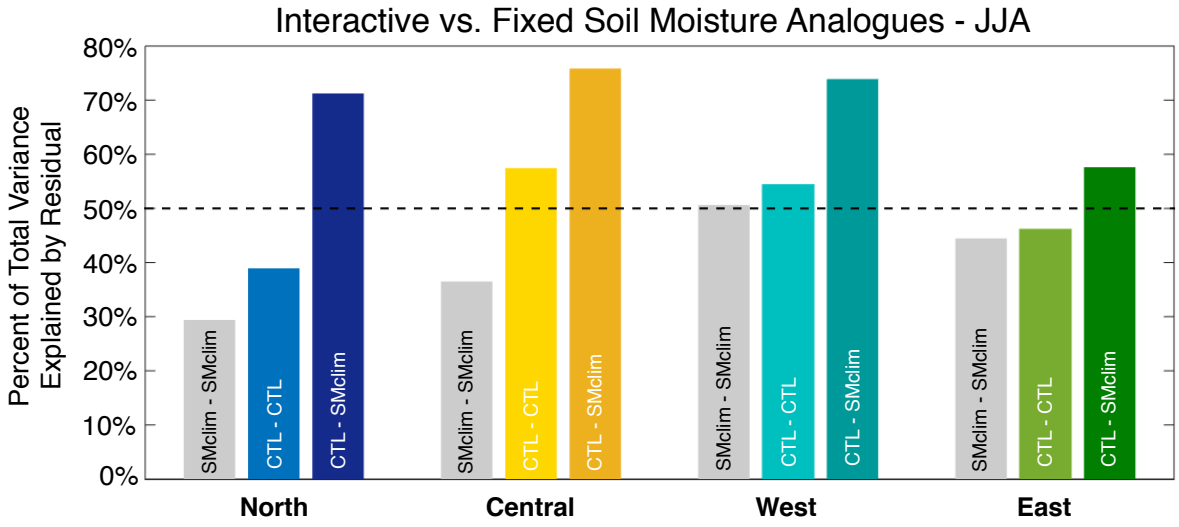

Figure 4.11: As in Figure 4.5, percent of total SAT variance explained by residual SAT, averaged over the four regions shown in Figure 4.3. Gray bars indicate method uncertainty determined from the dynamical adjustment of SMclim SAT using SMclim analogues. Lighter colored bars show the relative magnitude of the interactive analogue residual obtained through dynamical adjustment of CTL SAT using CTL analogues. Darker colored bars show the relative magnitude of the fixed soil moisture analogue residual obtained through dynamical adjustment of CTL SAT using SMclim analogues.

Because observed dynamical adjustment must be done with interactive soil moisture analogues, we evaluate whether JJA residual SAT exceeds method uncertainty (gray bars) despite thermodynamic contamination in Figure 4.11. JJA residual SAT computed from SMclim analogues (Figure 4.11, darker colored bars) explains more of total SAT variance than JJA residual SAT computed from CTL analogues (Figure 4.11, lighter colored bars) in all regions. CTL analogue-derived residual SAT exceed method uncertainty by only 2% in the East (green), 3% in the West (teal), and 10% in the North (blue). In contrast, 20% more variance is explained in the Central region, which suggests the region is distinct and a land-atmosphere hot spot.

4.3.3 Sensitivity to Analogue Selection Period

The remainder of this chapter focuses on leave-one-out dynamical adjustment of the CTL simulation and two potential sensitivities of the method in the summer. The setup emulates

observed dynamical adjustment and can therefore inform analogue specifications and parameter choices.

First, we assess whether dynamical adjustment is sensitive to analogue selection period. For leave-one-out dynamical adjustment of the CTL, analogues are selected from the 150-year CESM GLACE experiment period of 1950-2100. The CTL simulation, however, is also a part of the CMIP5 archive, and as such has a historical forcing period that extends back to 1850. We leverage this 155-year extended historical record and repeat the dynamical adjustment of the CTL simulation using analogues selected from 1850-2005. The two adjustments differ because the analogues of SLP and SAT experience different radiative forcings. Both analogue selection periods sample the (extended) historical forcing period from (1850) 1950 to 2005, but leave-one-out CTL dynamical adjustment also samples the RCP8.5 forcing period from 2006-2100 (Riahi et al., 2011). The 8.5 W/m^2 increase in radiative forcing from 2006-2100 induces a forced trend in SAT and results in a warmer mean climate by the end of the CTL simulation. Due to this mean warming, an SLP analogue selected from the end of the CTL simulation will have corresponding SAT anomalies that are warmer than an SLP analogue selected from the beginning of the CTL simulation (Lehner et al., 2017). To correct for the forced warming, a quadratic least-squares fit is removed from CTL SAT at each grid point. The quadratic detrending and other high-pass filtering techniques are discussed in more detail in Deser et al. (2016).

Ultimately, the quadratic detrending of SAT should ensure that SLP analogues have corresponding unforced SAT anomalies throughout the extended CTL simulation. Selecting analogues from the 1850-2005 period should be equivalent to selecting analogues from the 1950-2100 period. The dynamic components of SAT variability for the 1950-2100 (i) and 1850-2005 (ii) analogue selection periods are shown for each season in Figure 4.12. Despite analogues being selected from different portions of the CTL simulation, dynamic SAT variability is similar both spatially and in terms of magnitude in the two cases. This supports the hypothesis

that the method of dynamical adjustment relatively insensitive to analogue selection period as a result of forced SAT trend removal.

In JJA, both analogue selection periods result in a region of elevated dynamic SAT variability in the central US (Figure 4.12 c). This suggests that thermodynamic contamination is also insensitive to analogue selection period. To summarize the sensitivity of summer dynamical adjustment to analogue selection period, Figure 4.13 shows regional averages of percent variance explained by JJA residual SAT. Solid colored bars signifying analogue selection from the 1950-2100 period and outlined bars signifying analogue selection from the 1850-2005 period. As in Figure 4.11, gray bars show the method uncertainty threshold for each region. On average, JJA residual SAT explains approximately 38% of total SAT variance in the North (Figure 4.13 blue bars) for both the selection periods. In other regions, percent variance explained is similar for the two selection periods (within ±5%).

4.3.4 Sensitivity to Number of Analogues (N_s)

The final aspect of summer dynamical adjustment we evaluate is the sensitivity of constructed SLP and dynamic SAT to the number of analogues (N_s) used in their formation. We perform ten additional leave-one-out dynamical adjustments on the CTL simulation varying N_s from 5 to 55 analogues in five analogue increments. The N_s analogues are selected from $N_a = 80$ possibilities and the process is repeated $N_r = 100$ times, as in other dynamical adjustments in this chapter.

To assess sensitivity, we compare the spatial match of total and constructed SLP for each year of the historical period (Figure 4.14). Spatial match is determined through SLP spatial correlation over the North American domain ($20 - 75°$N, $50 - 170°$W). SLP spatial correlations are, on average, above 0.90 in each season, regardless of the number of analogues used in construction. This confirms dynamical adjustment is successful in reconstructing SLP, even with as few as 5 analogues. Spatial correlations are lower and more variable in MAM (Figure 4.14,

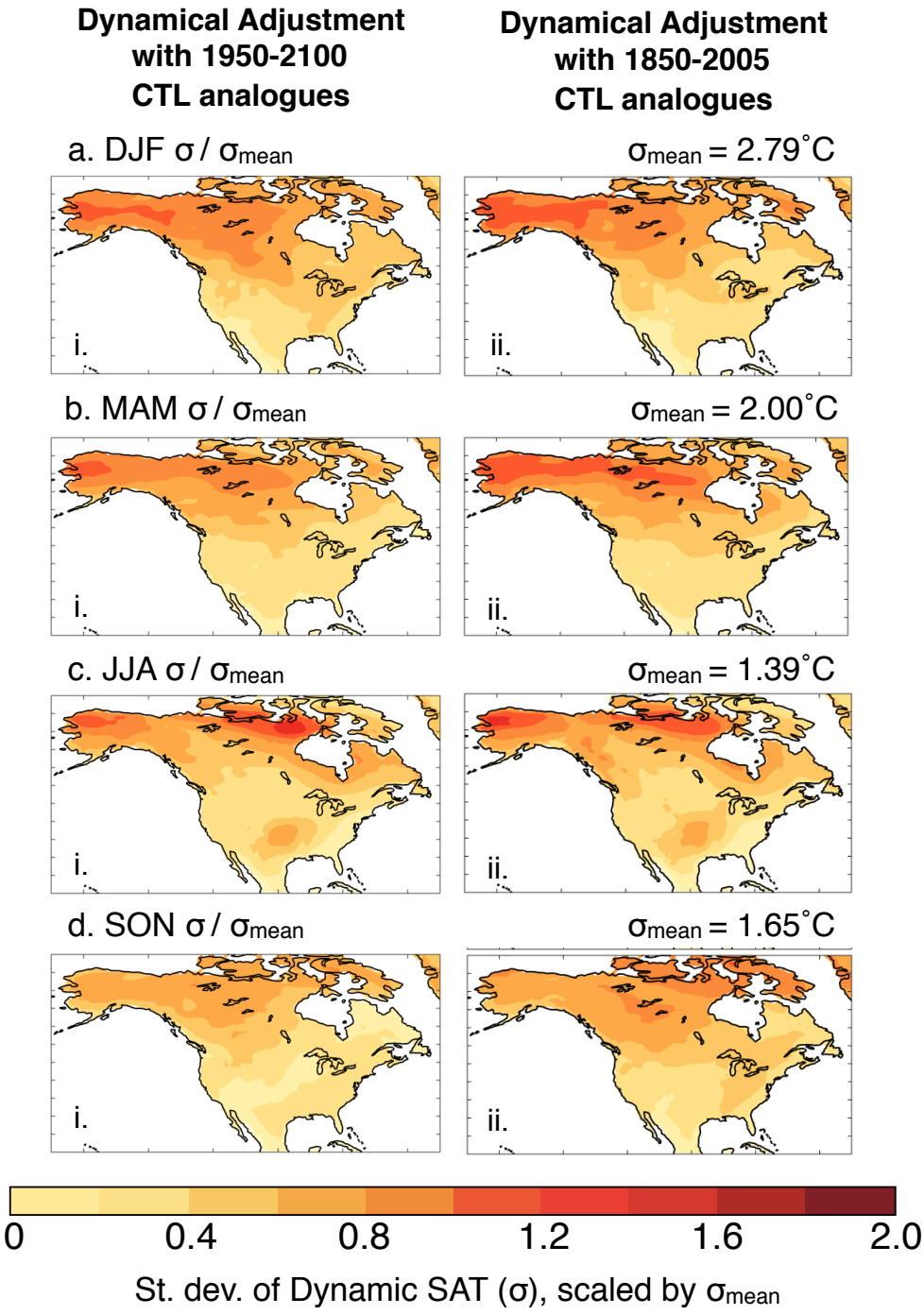

Figure 4.12: Standard deviations (σ; °C) of the seasonally-averaged dynamic component of CTL SAT, scaled by the domain average standard deviation of total SAT (σ_{mean}; °C). Panels a-d i (ii) show CTL dynamic SAT variability computed from dynamical adjustment using analogues from years 1950-2100 (years 1850-2005) of the CTL simulation.

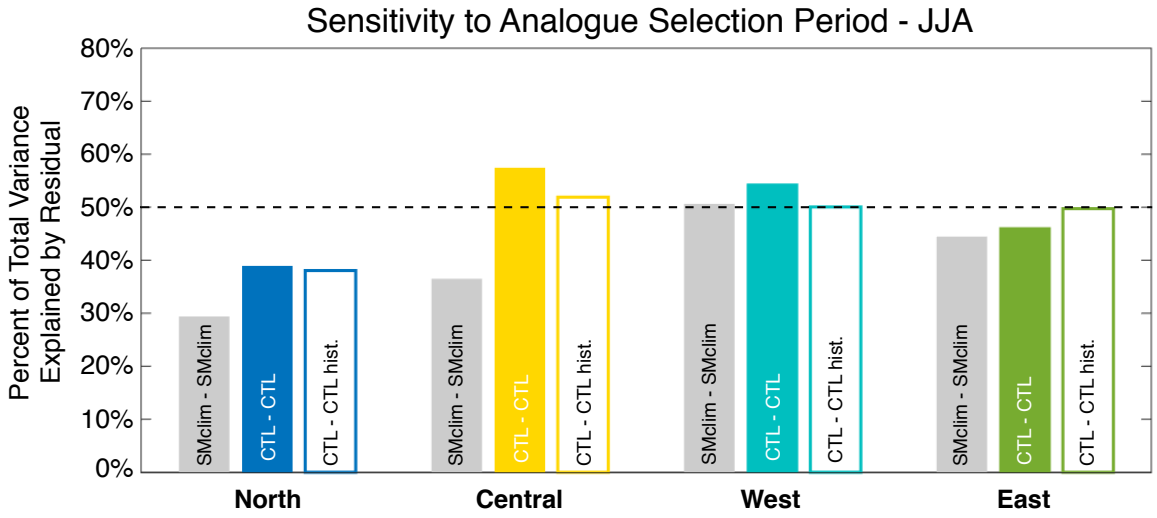

Figure 4.13: As in Figure 4.5 and Figure 4.11, percent of total SAT variance explained by residual SAT, averaged over the four regions shown in Figure 4.3. Gray bars indicate method uncertainty determined from the dynamical adjustment of SMclim SAT using SMclim analogues. Solid bars show the relative magnitude of the CTL residual obtained through dynamical adjustment using the CTL 1950-2100 analogue period. Outlined bars show the relative magnitude of CTL residual obtained through dynamical adjustment using the CTL 1850-2005 analogue period.

cyan) than in other seasons. As more analogues are used to construct SLP (increasing N_s), correlations approach unity. Spread is reduced to values of 10^{-3} by $N_s = 30$ in JJA and SON, and by $N_s = 35$ in DJF. In MAM, spread remains larger than 10^{-3} by $N_s = 55$. Correlations have converged to average values of 0.997-0.999 in each season by $N_s = 50$, which is the value used for the other dynamical adjustments in this chapter.

Another way to assess sensitivity to the number of analogues is through the dynamic component of SAT, which is shown in terms of percent of total variance explained as a function of N_s in Figure 4.15. Dynamic SAT explains less total SAT variance when fewer analogues are used in its construction, which confirms that the efficacy of dynamical adjustment relies on the having a large pool of analogues to pick from. Averaged over the whole North American domain, the percent of DJF SAT variance explained by dynamic SAT increases from 40% for $N_s = 5$ to 63% by $N_s = 40$ (Figure 4.15, blue). A similar evolution with increasing N_s occurs in JJA,

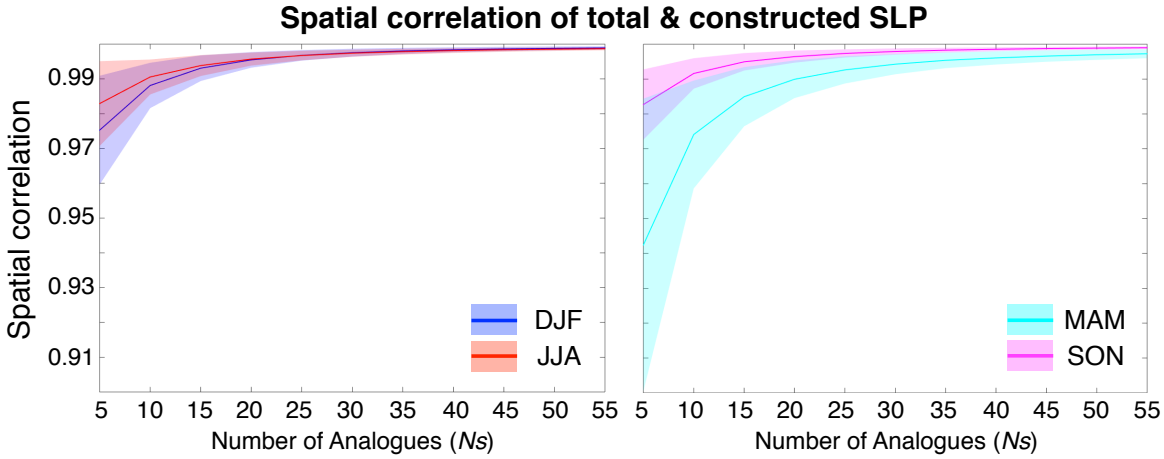

Figure 4.14: Spatial correlation between SLP and constructed SLP, constructed by selecting N_s analogues from a set of 80 possibilities, where N_s is 5 through 55 in steps of 5. Lines indicate the average spatial correlation and the shading indicates $\pm 1\sigma$ spread in spatial correlation across the 55 years in the historical period (1951-2005). DJF (blue) and JJA (red) correlations are shown in the left panel. MAM (cyan) and SON (magenta) correlations are shown in the right panel.

with the percent variance explained by dynamic SAT increases from 24% for $N_s = 5$ to 44% by $N_s = 30$, and remains between 44 – 45% thereafter (Figure 4.15, red). In MAM, however, percent of variance explained by dynamic SAT increases to 53% by $N_s = 30$ and then decreases to 48% by $N_s = 55$ (Figure 4.15, cyan). The percent of SON SAT variance explained by dynamic SAT also decreases, from 43% for $N_s = 25$ to 40% for $N_s = 55$ (Figure 4.15, magenta). Based on the sensitivity analysis of SLP and dynamic SAT, we advise further evaluation of the optimal parameters to use for dynamical adjustment of MAM and SON SAT.

4.4 Developing an Observation-Based Land-Atmosphere Hot Spot Metric

One of the objectives of evaluating the dynamical adjustment of the CESM GLACE experiment is to inform the development of a land-atmosphere hot spot metric that leverages the longer, more spatially complete observational records of SAT and SLP. With this in mind,

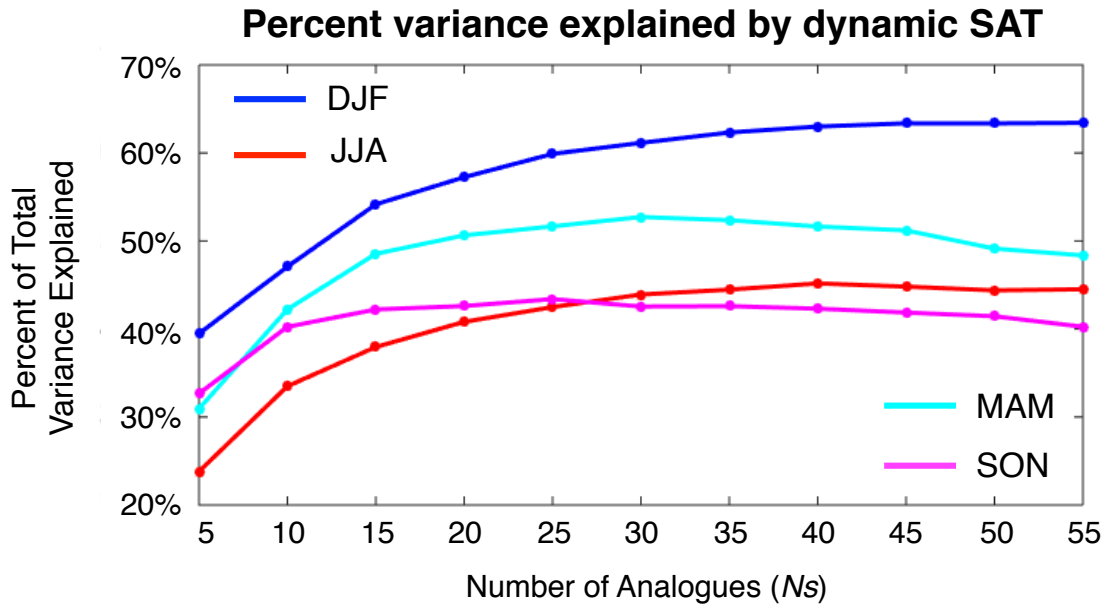

Figure 4.15: Percent of total SAT variance explained by dynamic SAT for different values of N_s, for each season, averaged over the full North American domain.

we used the same version of dynamical adjustment, the leave-one-out method, that is used to dynamically adjust observations (Deser et al., 2016; Lehner et al., 2017). Analogues are selected from a 150-year long record, which approximately corresponds to the record length of SAT and SLP observations. We provide evidence that the method is relatively insensitive to selection period, provided SAT is first quadratically-detrended to remove any forced warming trend, and to the number of analogues used, provided that N_s is greater than 30.

Beyond guiding methodological choices, the dynamical adjustment of the SMclim simulation demonstrates that method uncertainty accounts for 20-45% of total SAT variance, depending on region, season, and possibly on orography. The implication of this is that dynamical adjustment should not be used as a black box. If residual SAT explains less than 45% of total SAT variance, a case must be made for its physical basis. Similar care must be taken in regions where total SAT variability is low (unlikely to be a hot spot due to a lack of signal) or regions where elevations are 1000 m or more above sea level (where method error is largest). However, if a region has both relatively larger SAT variability and a residual component that explains more

than 45% of total SAT variance, it can be identified as a land-atmosphere hot spot.

Finally, it is important to recognize that an analogue method has limitations, which could affect one's ability to use dynamical adjustment to characterize the dynamic or thermodynamic contribution to individual events. The summer stands out as the season most susceptible to contamination of the dynamic component by thermodynamically-driven SAT anomalies in analogues. Thermodynamic contamination in the summer often leads to an underestimate of residual SAT and could affect the land-atmosphere hot spot metric. We recommend determining the soil moisture conditions in each analogue as a way to document that you are averaging across a variety of different land surface states and therefore less likely to contaminate the dynamic component of SAT with the thermodynamic signal you wish to evaluate.

4.5 Summary

In this chapter, we present a systematic evaluation of summer dynamical adjustment and conclude that the method can be used to remove the effect of circulation on SAT to reveal a North American hot spot of land-atmosphere interaction. We find is no methodological limitation that would prevent using dynamical adjustment to identify land-atmosphere hot spots in an observational framework. Method uncertainty was demonstrated to be smaller than the land-atmosphere hot spot threshold defined in (Merrifield et al., 2017), which confirms that residual SAT in the central US hot spot had a physical basis. We suggest that is residual SAT explains more than 45% of total SAT variance in a region, the region is a candidate land-atmosphere hot spot and should be explored further.

There are several caveats to the 45% variance explained land-atmosphere hot spot threshold, which are discussed in section 4. The main limitation of summer dynamical adjustment, however, is the potential for thermodynamic contamination of the dynamical component. Contamination is likely to occur in regions of strong land surface feedback and is another source of method

uncertainty. While it is recommended that as many analogues as possible are used, SLP can be effectively reconstructed in DJF and JJA using 100 30 analogues sets. The dynamic components of DJF and JJA SAT become insensitive to the number of analogues per set for sets of more than 45 analogues. Further analysis of parameter sensitivity in MAM and SON is warranted.

Chapter 5

The Role of the Land-Atmosphere Interactions during a Persistent European Heat Wave

5.1 Introduction

In prior chapters, we explored the role of soil moisture on year-to-year variations of summer surface air temperature (SAT) in the central United States. While understanding the relationship between soil moisture and interannual SAT variability is useful, it is also important to understand the role of soil moisture during heat waves. Heat waves are socioeconomically impactful throughout the Northern Hemisphere midlatitudes but are of particular concern in densely populated Europe. Recent persistent hot extremes, including the 2003 heat wave in western Europe, have caused billions of dollars of agricultural losses (Heck et al., 2001) and tens of thousands of excess deaths (Robine et al., 2008). Moreover, as the climate system warms, it is anticipated that European heat waves will become more frequent, intense, and persistent (e.g Schär and Jendritzky, 2004; Meehl and Tebaldi, 2004; Beniston et al., 2007).

Soil moisture has been identified as a key contributor to the intensity and duration of European heat waves (e.g Vautard et al., 2007; Lorenz et al., 2010; Jaeger and Seneviratne, 2011). Using a regional climate model, Fischer et al. (2007b) concluded that wetter soils could have mitigated the exceptional summer temperatures during the 2003 heat wave by up to 40%; climatological soil moisture would have offered up to 2°C of relief. Primarily, soil moisture influences surface climate through the partitioning of outgoing surface energy between the latent and sensible heat fluxes (Seneviratne et al., 2010; Berg et al., 2014). Under typical circumstances, the partitioning of fluxes by soil moisture affects SAT only in not too wet, not too dry "hot spots" of land-atmosphere interaction (Koster et al., 2004a), such as the Mediterranean region in southern Europe (Seneviratne et al., 2006b; Hirschi et al., 2011; Diffenbaugh et al., 2007). During heat waves, however, as soils dry out under above average SAT, the land surface feedback can occur on a continental scale (Fischer et al., 2007a).

While the land surface can amplify or damp extreme SAT, heat waves are set in the atmosphere. In most cases, heat waves accompany persistent, stationary high pressure systems, or blocking highs (Charney and DeVore, 1979; Hurrell, 2015). Blocking highs over Europe tend to form in the quiescent region between splits in the polar jet (Egger, 1978; Barnes and Screen, 2015) and can be amplified by the quasi-stationary component of both free and thermally/orographically forced atmospheric Rossby waves (Schubert et al., 2011; Petoukhov et al., 2013; Coumou et al., 2015). Blocking highs tend to be dynamically linked to low pressure systems, which help to stall them (Perkins, 2015), and may occur more frequently during episodes of anomalous tropical Atlantic convective heating (Cassou et al., 2005). Once established, blocking highs bring clear skies, light winds, subsidence, and warm air advection, all of which contribute to heat wave conditions (Meehl and Tebaldi, 2004; Fischer et al., 2007b).

On synoptic timescales, the circulation and the land surface operate in tandem to amplify SAT. The feedback process is summarized by Miralles et al. (2014). In the atmosphere, advection and enhanced entrainment bring warm air to the boundary layer during the day, which dries

soils. An inversion traps the day's heat in the boundary layer overnight. Over several days, heat accumulates and the surface atmosphere is warmed further by the continual desiccation of soil moisture, resulting in a heat wave. By this mechanism, dry initial soil conditions increase the risk of dangerously extreme heat. Quesada et al. (2012) documented the asymmetry in heat wave influence, finding that summer temperature is more sensitive to the occurrence of blocking regimes when soils are initially dry.

While there are many ways to define a heat wave (Meehl and Tebaldi, 2004; Perkins, 2015), we assess a persistent seasonal hot extreme (Figure 5.1 a, red dot), which for clarity, will be referred to as a heat wave following Fischer et al. (2007b) and Zampieri et al. (2009). In this chapter, we aim to quantify to what extent dry spring soils exacerbate a summer heat wave in central Europe. We use a Community Earth System Model (CESM) preindustrial control simulation to create three ensembles with varying degrees of internal atmospheric variability to establish the relationship between preseason land surface conditions and SAT. Relationships between summer SAT and other concurrent dynamic and thermodynamic controls are also explored. The remainder of this chapter is structured as follows. Section 2 details the experimental design, section 3 presents the results and section 4 provides a summary.

5.2 Experimental Design

To assess the role of preseason soil moisture on a subsequent European heat wave, a model experiment was performed within a CESM preindustrial control framework, which is summarized in Table 1. A 306-year control simulation, henceforth referred to as CTL, was used as the basis of the experiment. CTL experiences preindustrial (1850) radiative forcing levels and has prescribed climatological sea surface temperature (SST) and sea ice. SST and sea ice climatology is calculated as the average of years 401-1399 of the CESM Large Ensemble 1850 control simulation (Kay et al., 2015). The AMIP-style (Gates, 1992), preindustrially forced CTL

allows for the isolation of internal atmospheric variability, as ocean-atmosphere feedbacks are suppressed by the prescription of climatological SST and the atmosphere experiences no change in radiative forcing from 1850 levels. The only component of the climate system coupled with and capable of modifying atmospheric conditions is the land surface.

Table 5.1: Description of CESM simulation experiments used in this chapter.

Experiment	Abbreviation	Description
Control Simulation	CTL	306 year AMIP-style simulation, with prescribed climatological SST from years 401 - 1399 of the CESM Large Ensemble control run and preindustrial (1850) radiative forcing.
Heat wave Case	Year 200	Year selected from CTL to evaluate conditions during a seasonally persistent heat wave.
Prescribed Circulation Ensemble	PCE	Ensemble of 44 CTL years, branched from June 1 and with Year 200 circulation imposed above 322 hPa.
Prescribed Circulation Ensemble, Full Column	PCE_{full}	Ensemble of 44 CTL years, branched from June 1 and with Year 200 circulation imposed over the full vertical column.

5.2.1 Control Simulation

Interannual summer SAT variability in CTL simulation is illustrated in Figure 5.1 a. The CTL timeseries (Figure 5.1 a, black) shows June-July-August (JJA) SAT, area-averaged over the boxed region which encompasses central Europe (Figure 5.1 a, inlay; 41.94°-53.25°N, 1.25°W-23.75°E). Throughout this chapter, CEU is used to refer to fields area-averaged over this region. The CEU region also approximately bounds the region that experienced the 2003 European summer heat wave (Black et al., 2004).

A seasonally-persistent European heat wave occurs in Year 200 of the CTL simulation. JJA CEU SAT in the Year 200 (Figure 5.1 a, red dot) is 21.9°C, 2.5°C above the long-term average for the region. The May-September evolution of the Year 200 heat wave, in terms of monthly

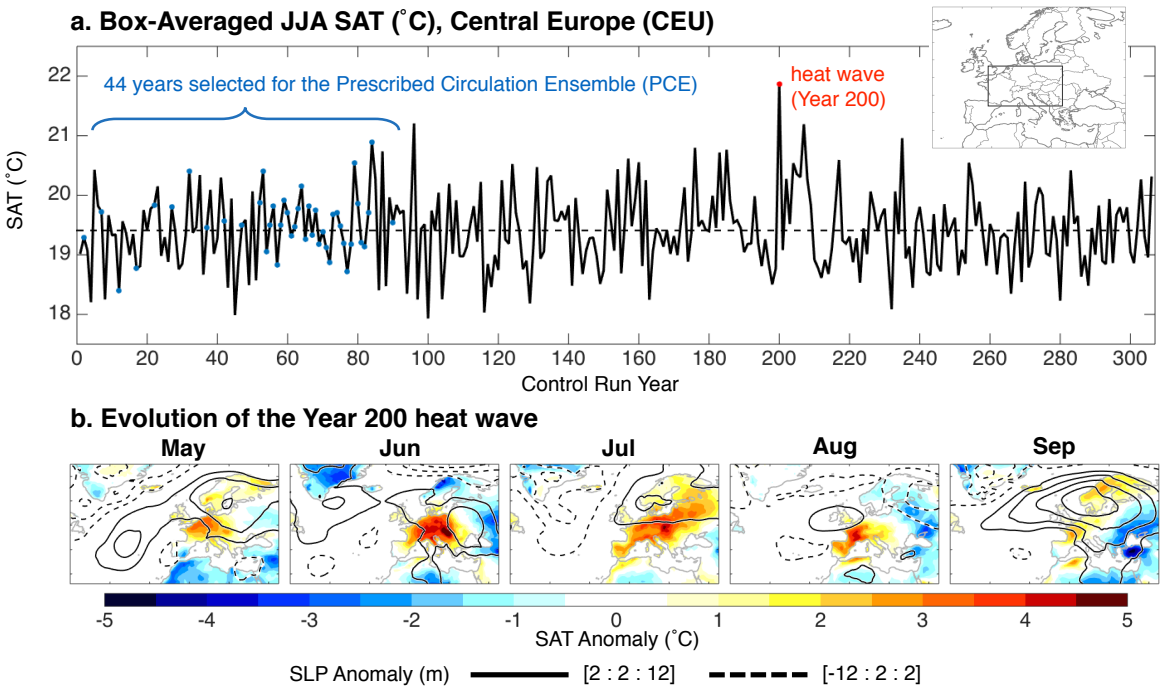

Figure 5.1: (a) June-July-August (JJA) Surface Air Temperature, box-averaged over central Europe (CEU; inlay), in an AMIP-style preindustrial control run. The year with the highest average SAT (Year 200; red dot) is selected as the heat wave case. Years selected to comprise the Prescribed Circulation Ensemble (PCE) are indicated with blue dots. The PCE is a set of runs branched from the control run with Year 200 winds imposed from June to September. Initial land surface states differ between PCE members. (b) SAT (°C; color) and SLP (m; contours) anomalies during the Year 200 heat wave.

mean SAT (color) and sea level pressure (SLP; contours) anomalies, is shown in Figure 5.1 b. Anomalies in this chapter are computed with respect to the 306-year climatology unless otherwise noted.

In May, prior to the heat wave, Year 200 SAT is between 1.5 and 3°C above average in the CEU, with anomalies largest in Northern France, Belgium, and the Netherlands (Figure 5.1 b). The warm temperatures accompany a ridge of SLP that extends from the North Atlantic to northern Europe. The heat wave starts in earnest in June, with SAT anomalies reaching 5°C over Hungary and Slovakia. A high pressure system remains over continental Europe, now centered over eastern Europe. By July, nearly the whole of Europe is experiencing above average SAT, while the high pressure block remains over the continent for a third consecutive month. By August, the persistent blocking high weakens, alleviating heat wave conditions in most of the CEU. Temperatures in France, however, still remain over 4°C hotter than average. In September, a strong high pressure system returns, but SAT in the CEU remains less than 3°C above average. With consistent blocking conditions in the atmosphere and a large spatial extent, the Year 200 heat wave is optimal for a land surface feedback assessment.

5.2.2 Prescribed Circulation Ensembles (PCEs)

With the target heat wave chosen, 44 other years are selected to provide a representative distribution of the CTL (Figure 5.1 a, blue dots). The CTL is then branched from of each of these 44 years. Starting June 1 of, for example, Year 2, zonal (u) and meridional (v) winds are linearly relaxed from Year 2 values towards Year 200 values. U and v are updated in the model every 6 hours and are linearly interpolated between time steps; the linear relaxation is towards the linearly interpolated values and takes place between the interval. This process effectively prescribes the atmospheric circulation that sets the Year 200 heat wave onto an initial condition ensemble, thus creating a Prescribed Circulation Ensemble (PCE). Year 200 conditions are prescribed through the summer, culminating September 30.

Two PCEs of June through September monthly-averaged fields are considered in this chapter. The primary ensemble considered is the PCE, which has circulation prescribed above 322 hPa (top 16 pressure levels of the CESM atmosphere model, CAM5). Secondarily, we consider the PCE_{full}, which has circulation prescribed over the full atmospheric column (each of the 30 pressure levels in CAM5 from 992.6 to 3.6 hPa). To compare with the PCEs, an ensemble of the original 44 years from the CTL, or CTL ensemble, is also considered.

The CTL, PCE, and PCE_{full} ensembles can also be interpreted in terms of their respective levels of internal atmospheric variability. The CTL ensemble has full internal variability; each of the 44 years encounters a different set of atmospheric circulation patterns through the summer. The PCE has partial internal variability, atmospheric circulation is fixed to Year 200 conditions at the top of the troposphere, but left free to vary beneath. The PCE_{full} has the least amount of internal variability, as atmospheric conditions present during the Year 200 heat wave are prescribed over the full atmospheric column. We anticipate that the land surface feedback on SAT will be damped in the PCE_{full} by the atmospheric constraint, because SAT modified by dry soil conditions will not experience amplification associated with the feedback between SAT and atmospheric circulation (Fischer et al., 2007b; Haarsma et al., 2009; Koster et al., 2016).

5.2.3 Initial land surface states

Though the three ensembles differ in aspects of atmospheric circulation, the PCE, PCE_{full}, and CTL ensemble share a set of initial conditions, represented by soil moisture in Figure 5.2. Throughout this chapter, soil moisture refers to the average of soil liquid water (SOILLIQ) over the top 8 levels (approximately 1 m) of CESM's land model, CLM4.5, which approximately corresponds to the root zone (Shukla and Mintz, 1982; Hirschi et al., 2014). May soil moisture anomalies (kg/m^2) for each of the 44 ensemble member years and Year 200 (bottom right, gray background) are shown in Figure 5.2 a, with the CEU region boxed on each panel. The distribution of May CEU soil moisture is shown in Figure 5.2 b. 283 CTL run years have soil moisture output

available from May through September (Figure 5.2 b, gray bars); CEU anomaly values range from -20.7 to 17.7 kg/m^2. Year 200 soil moisture is anomalously dry in May, (Figure 5.2 b, red line), but at -20.0 kg/m^2, it is not the driest initial state in the CTL distribution. Mays that are drier than Year 200 in the CTL are not followed by a Year 200-level heat wave, which indicates that preseason soil dryness must be accompanied by heat wave favorable circulation to instigate an exceptionally hot summer.

The 44-year distribution of initial conditions (Figure 5.2 b, black bars) is representative of the 283 year CTL distribution, though does not capture the full extent of the dry side tail. Two extreme initial condition years are indicated in Figure 5.2 b with vertical lines; the driest CEU May, Year 54, is shown in magenta, and the second wettest CEU May, Year 55, is shown in cyan. Year 54 is slightly drier than Year 200 in an area-average sense, and is notably drier in the southern portion of the CEU domain, the Mediterranean region where an active land surface feedback has been identified (Seneviratne et al., 2006b; Vidale et al., 2007; Fischer and Schär, 2009). A dry anomaly in the northern portion of the CEU domain keeps Year 55 from being the wettest CEU May, but a relatively large positive soil moisture anomaly in the Mediterranean portion of the CEU domain make it among the wettest in the distribution.

5.3 Results

5.3.1 Evolution of Prescribed Heat Waves

Year 54 in the PCE, which starts out with the driest May soil moisture anomaly, has the maximum June through August heat wave in the PCE (Figure 5.3 a, i-iii). With initial soil moisture conditions on the other extreme, Year 55 has the minimum June through August heat wave in the PCE (Figure 5.3 a, iv-vi). All PCE (and PCE$_{\text{full}}$) ensemble members feature heat waves that are spatially similar to the Year 200, but differ in SAT anomaly magnitude. This confirms that the atmospheric circulation pattern we prescribe is responsible for setting SAT

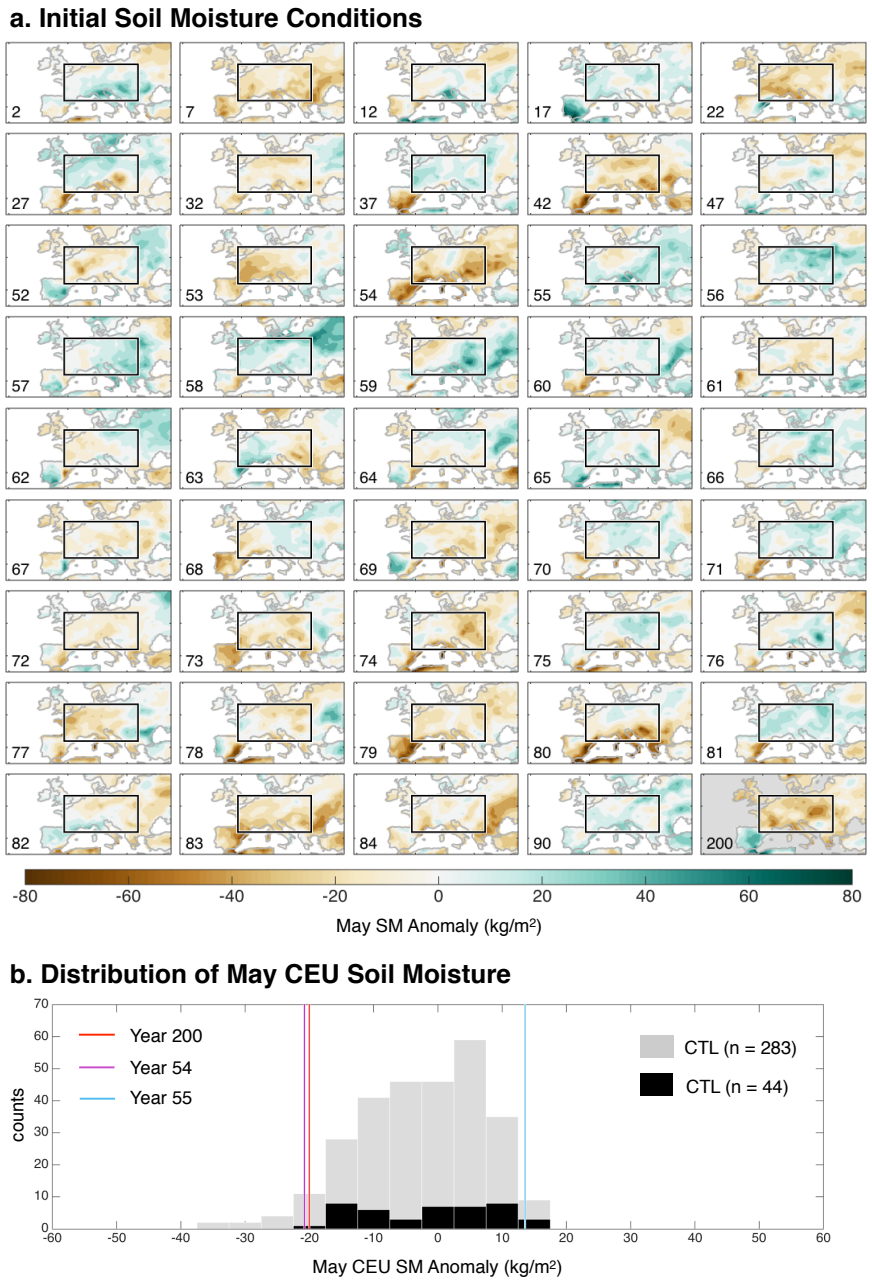

Figure 5.2: (a) May soil moisture anomalies (kg/m^2), which represent initial land surface states for each of the 44 PCE members and the Year 200 (bottom right, gray background). The index in the bottom left of each panel indicates the CTL year each member was branched from. The CEU averaging region is boxed in each panel. (b) Histograms of May CEU soil moisture anomalies (kg/m^2), for all available CTL years (gray bars) and the 44 CTL years selected for the PCE (black). Lines represent May CEU soil moisture anomalies for the Year 200 (red), and two extreme members of the PCE, Year 54 (magenta) and Year 55 (cyan).

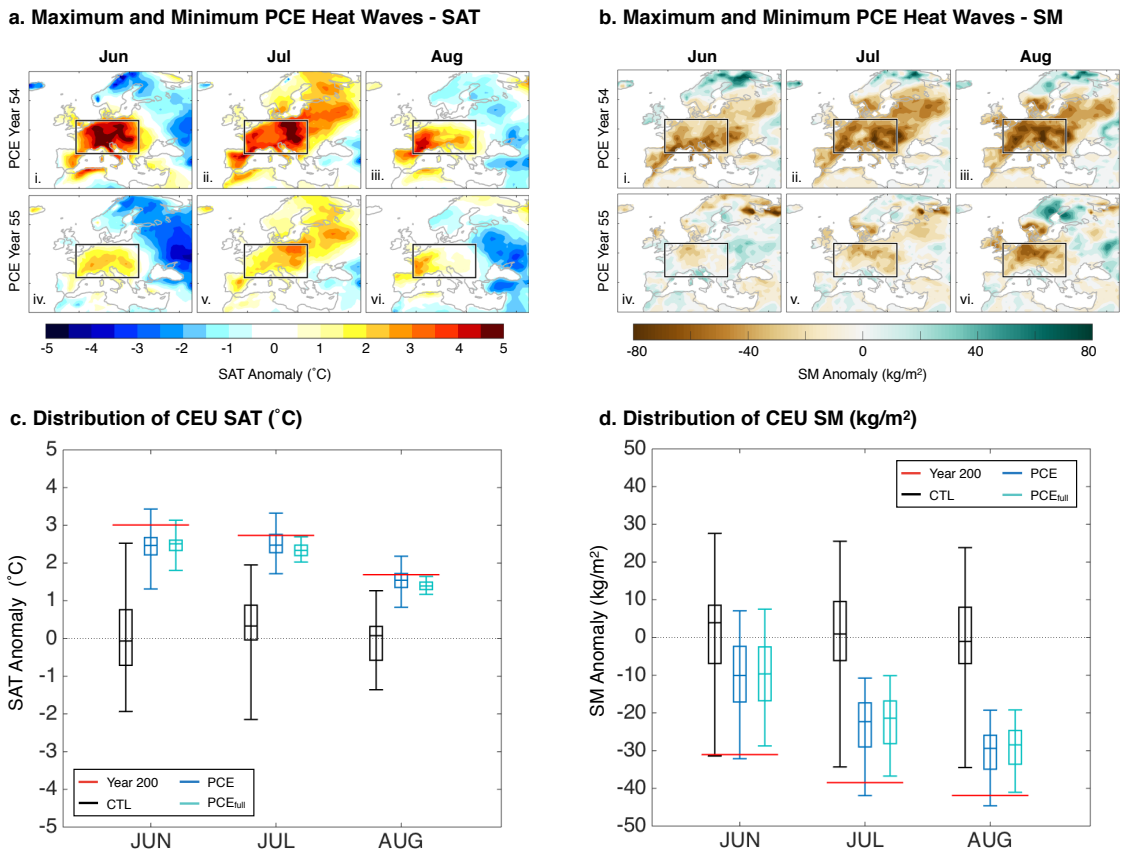

Figure 5.3: (top) June, July, and August (a) SAT anomalies (°C) and (b) soil moisture anomalies (kg/m^2) for Year 54, the hottest member of the PCE (i-iii) and Year 55, the coolest member of the PCE (iv-vi). (bottom) Box-and-whisker plots illustrating the PCE (blue) and PCE$_{full}$ (teal) distributions of CEU (c) SAT (°C) and (d) soil moisture (kg/m^2) anomalies from June through August. Year 200 values are indicated in red.

patterns in this CESM framework. Soils dry beneath the heat wave in both years (Figure 5.3 b), with Year 54 reaching a CEU average anomaly of -44.6 kg/m^2. Year 55 reaches a CEU average anomaly of only -20.9 kg/m^2. Consistent with the canonical land surface feedback (Seneviratne et al., 2010), Year 54 starts drier and evolves to be hotter than Year 55.

The effect of partial vs. full column prescribed circulation can be assessed by comparing the CTL, PCE, and PCE$_{full}$ CEU distributions. The box and whisker plots of SAT (Figure 5.3 c) and soil moisture (Figure 5.3 d) anomalies demonstrate that the PCE heat waves (blue) span a

larger range of SAT and a comparable but slightly drier range of soil moisture than PCE_{full} heat waves (teal). Without the circulation constraint, CTL CEU SAT and soil moisture anomalies (black) are distributed more uniformly about the mean. Missing CTL soil moisture values in July and August are replaced with alternate CTL years in order for n = 44 in each distribution. The box and whisker elements show the interquartile range (between the 25th and 75th percentiles) and the maximum and minimum CEU values. Year 200 CEU values are shown in red.

In Figure 5.3 c, CEU SAT anomalies range from 1.3 to 3.4 °C in the PCE and 1.8 to 3.1°C in the PCE_{full} in June; Year 200 CEU SAT (3°C) falls within the upper quartile of both distributions. In July and August, Year 200 CEU SAT falls below the 75th percentile of the PCE distribution, but above the maximum of the PCE_{full}. The narrowing of the PCE_{full} to span less than 0.7°C by July suggests that the atmospheric circulation constraint also strongly constrains SAT.

The PCE and PCE_{full} have similar CEU soil moisture distributions (Figure 5.3 d), which allows us to rule out soil moisture as the cause of reduced SAT spread in the PCE_{full}. Though the CTL, PCE, and PCE_{full} ensembles share initial soil moisture, exposure to the heat wave causes a systematic drying of all PCE and PCE_{full} members. By July, the PCE and PCE_{full} contain only members that are drier than average. PCE_{full} members do not dry out enough for Year 200 CEU soil moisture to fall within the distribution, which suggests that the atmospheric constraint on SAT damps the land surface feedback in the PCE_{full}. Because the PCE has approximately twice the SAT spread of the PCE_{full} and members that are drier than Year 200, we focus on evaluating the land surface feedback in the PCE in this chapter.

Because PCE atmospheric circulation is set only in the upper troposphere, circulation patterns beneath may vary. Differences in the unconstrained portion of the troposphere could be due to differences in land surface states and/or to random fluctuations that occur internally in the atmosphere. The extent of tropospheric differences in the PCE can be explored in vertical longitude sections (Figure 5.4). We chose the center latitude of the CEU, (47.6°N; dashed line), as

representative of the heat wave circulation pattern, based on Year 200 SLP anomalies (Figure 5.4 a). Geopotential height (Z; m) anomalies, from 60°W to 45°E and 992.6-200 hPa, for Year 200, PCE Year 54, and PCE Year 55 are shown in Figure 5.4 b-d respectively. The sections cross the Alps and the western slope of the Carpathian mountain range, which are shown in each panel in black; orographic features in the CEU are discussed further in Figure 5.5. As a guide, the longitudinal boundaries of the CEU (1.25°W-23.75°E) are also marked in each panel by dotted lines.

Prescribing atmospheric circulation above 322 hPa results in PCE members having the same geopotential height anomaly pattern as Year 200 (Figure 5.4 b-d). In June (i), atmospheric circulation takes the form of a wave train with low pressure center west of the CEU region, a strong high pressure center over the CEU region, and low pressure to the east. This blocking pattern is similar to the one that occurred in June during the 2003 heat wave (Ferranti and Viterbo, 2006; Della-Marta et al., 2007). In July (ii), a dipole pattern is present. In August (iii), the high pressure center that remains has shifted to the west of the CEU region, consistent with the heat wave contracting westward.

As the extremes of the PCE, the maximum heat wave in Year 54 (Figure 5.4 c) and minimum heat wave in Year 55 (Figure 5.4 d) are likely to have the largest Z anomaly differences. In terms of magnitude, the maximum (minimum) PCE heat wave has a stronger (weaker) high pressure center over the CEU region in June, July, and August. In addition to being stronger, the CEU high pressure center is also broader in the Year 54 maximum heat wave than in Year 55 minimum heat wave throughout the summer. Outside of the CEU, low pressure anomalies tend to be weaker in Year 54 than Year 55, particularly in July over the North Atlantic.

An awareness of the orography in the CEU is important for the interpretation of relationships between SAT and other fields. CESM orography, in m above the geoid, is shown in Figure 5.5. The CEU encompasses the lower elevation Northern European plain between the southwestern United Kingdom and Poland as well as the higher elevation Pyrenees, Alps, and

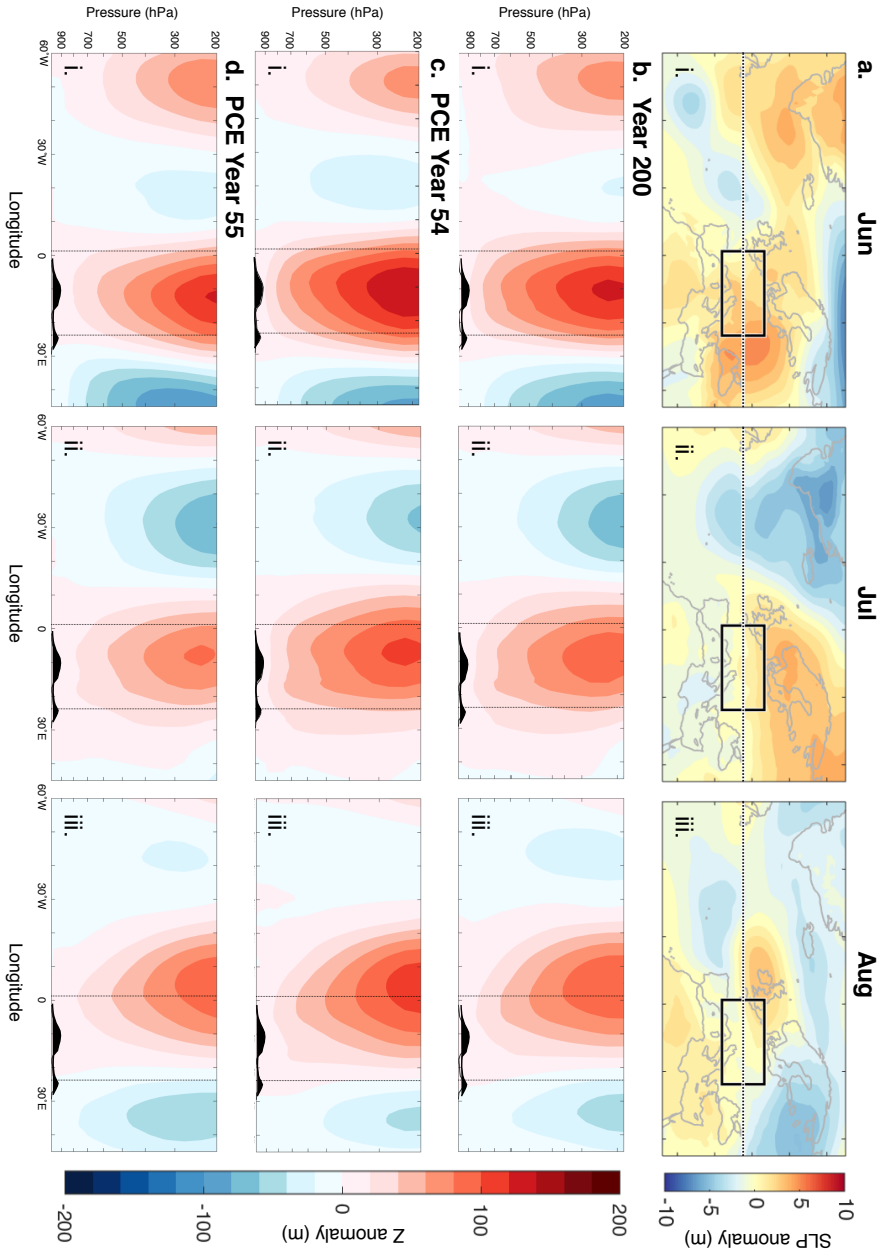

Figure 5.4: June, July, and August (i-iii) anomalies of (a) Year 200 SLP (m) and (b)-(d) geopotential height (Z; m), shown in longitude vertical sections above 47.6°N (dotted line in a). Z anomalies are shown for Year 200 in b, for Year 54 (hottest PCE member) in c, and for Year 55 (coolest PCE member) in d.

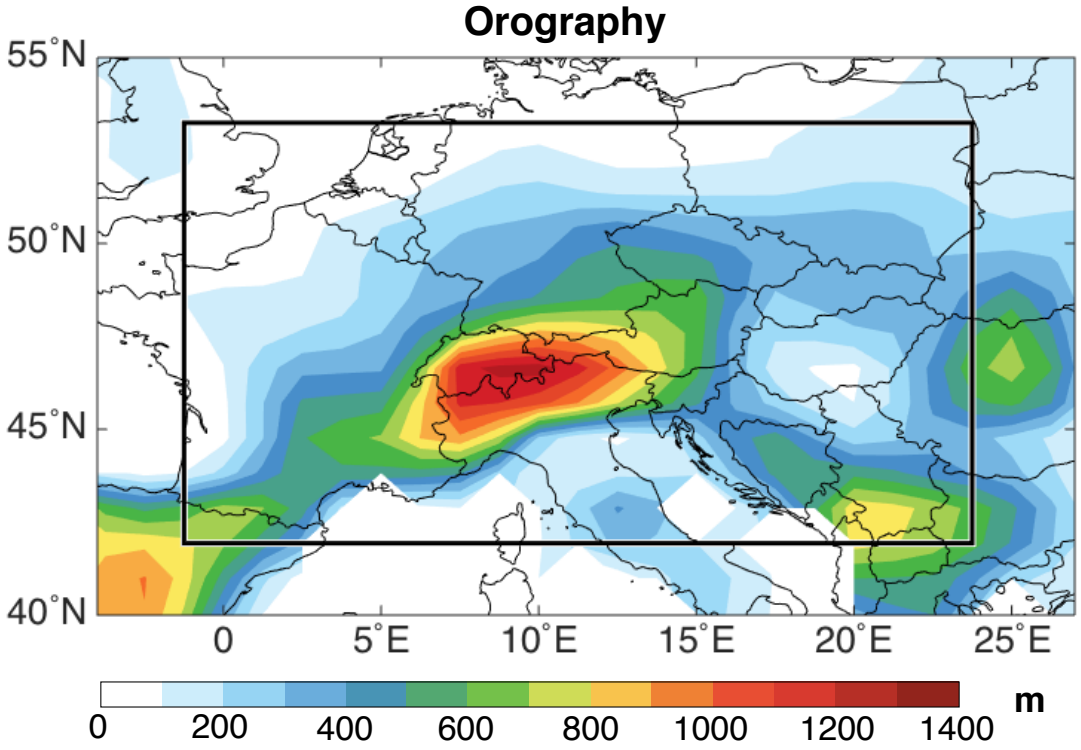

Figure 5.5: CESM's orography (m above the geiod) in the CEU box region.

Balkan mountain ranges. Because the nature of the land surface feedback changes at elevation (Wilson and Barros, 2017), orographic features more than 600 meters above the geoid are shown in black dashed contours as a visual guide in Figures 5.6, 5.9 and 5.12.

5.3.2 Concurrent relationships in the PCE

Before the role of preseason soil moisture conditions on a heat wave can be ascertained, it must be demonstrated that soil moisture influences SAT in the PCE. The first order influence of soil moisture on SAT occurs through the partitioning of the outgoing surface turbulent heat flux between sensible (Q_H) and latent (Q_E) heat fluxes (e.g. Seneviratne et al., 2010; Dirmeyer, 2011; Miralles et al., 2012). In the case of a heat wave, dry soils lack water to evaporate, leaving more outgoing energy available to heat the atmosphere through Q_H. Therefore, we anticipate that PCE members with drier soils will also have more total outgoing energy (Q_H + Q_E) in the sensible

heat flux (Q_H).

To determine if soil moisture dictates Q_H fraction ($Q_H/(Q_H + Q_E)$) in the PCE, we regress the latter on the former at each grid point (Figure 5.6 a). Prior to the regression, soil moisture is normalized at each grid point by subtracting the PCE mean and dividing by the PCE standard deviation. Regression coefficients are negative and can be interpreted as the percent increase in Q_H fraction per standard deviation of soil moisture (σ_{SM}) reduction.

In June (i), changes in soil moisture result in the largest changes in Q_H fraction, up to 6% per σ_{SM}, in the southern and eastern portions of the CEU region. By July (ii), Q_H fraction is sensitive to soil moisture over the whole CEU region except at altitude (dotted contours in Figure 5.6 a mark elevations above 600 m). The scatter plots in Figure 5.6 b show the relationship between normalized CEU soil moisture (σ_{SM}) and CEU Q_H fraction for June (yellow), July (orange) and August (red). Least squares regression lines of best fit for the CEU relationships (Figure 5.6 b) suggest that years that are one σ_{SM} drier than average have a 2% larger Q_H fraction. In Year 54 of the PCE, when soils are driest and SAT is the hottest, CEU Q_H fraction ranges from 0.41 in June to 0.56 in August. On the other extreme, in Year 55 of the PCE, CEU Q_H fraction ranges from 0.35 in June to 0.48 in August. The relationship between drier soils and a larger Q_H fraction among PCE members suggests that the land surface influences heat wave SAT in central Europe.

Along with the land surface feedback, other processes may contribute to the intensity of heat waves in the PCE. Two possible atmospheric contributors are the shortwave cloud radiative effect (SWCRE; W/m^2) and vertical velocity at 700 hPa (Ω_{700}; Pa/s). The SWCRE is the difference between all-sky and clear-sky downward shortwave radiation at the surface, and represents the reflectivity of clouds (Cheruy et al., 2014). More shortwave radiation reaches the surface when skies are clear, so the SWCRE is always negative. Larger negative values correspond to more cloud cover. Ω_{700} is the vertical wind velocity in pressure coordinates across the 700 hPa pressure level, with negative values representing upward motion and positive values

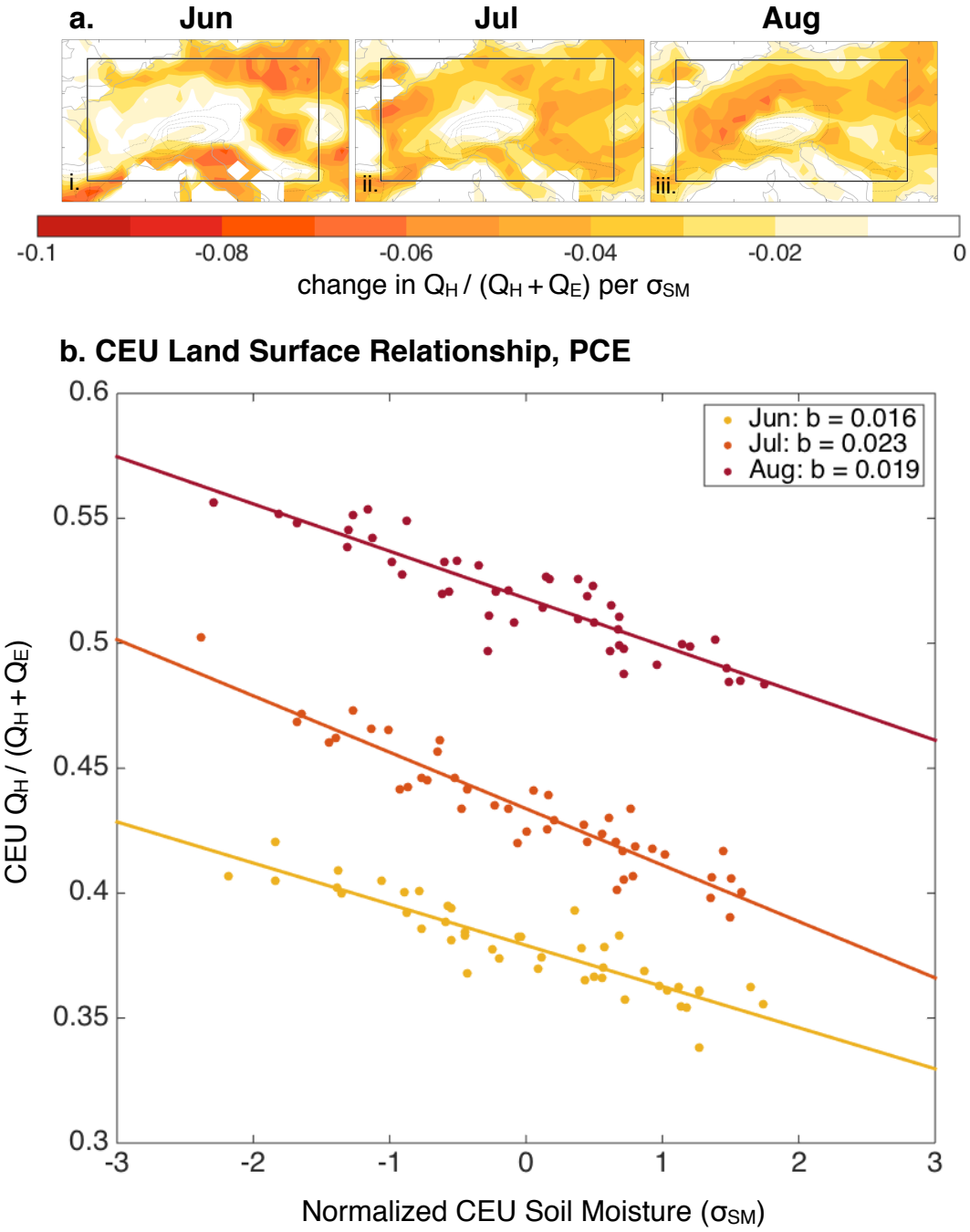

Figure 5.6: (a) Regression coefficient at each grid point, of the sensible heat flux fraction ($Q_H/(Q_H+Q_E)$) regressed on normalized concurrent soil moisture (σ_{SM}) for June (i), July (ii), and August (iii) in the PCE. (b) Scatter plot for June (yellow), July (orange), and August (red) CEU σ_{SM} vs. ($Q_H/(Q_H+Q_E)$), with coefficients of linear least-squares regressions for each month listed in the top right of the panel.

representing subsidence (Trenberth, 1978).

The climatology of (a) the SWCRE (W/m^2), (b) Ω_{700} (Pa/s), (c) SAT (°C), (d) Q_H fraction (dimensionless),and (e) soil moisture (kg/m^2) are shown in the left panel of Figure 5.7. In all summer months, there tends to be more cloud cover in the center of the CEU (over the Alps) and clearer skies in the southern CEU (Figure 5.7, left, row a). This cloud distribution is consistent with the climatological regions of positive and negative Ω_{700} (Figure 5.7, left, row b), as clouds form in regions of rising air (negative values of Ω_{700}) and clear skies tend to be associated with subsidence (positive values of Ω_{700}). SAT is coolest (warmest) at higher (lower) elevations and latitudes and warmer in the eastern than western CEU (Figure 5.7, left, row c). The distributions of Q_H fraction (Figure 5.7, left, row d) and soil moisture (Figure 5.7, left, row e) are also consistent with one another, larger Q_H fractions occur over the drier southern and eastern CEU. Between June (i) and August (iii), the largest evolution occurs in the southeastern corner of the CEU for the SWCRE, Q_H fraction, and soil moisture. The region becomes less cloudy, has an increase in Q_H fraction, and dries by more than 60 kg/m^2. SAT and Ω_{700} increase from June to August in the southern CEU.

The right panel of Figure 5.7 shows Year 200 anomalies for the SWCRE, Ω_{700}, SAT, Q_H fraction and soil moisture. During the Year 200 heat wave, the SWCRE is more positive than average (less cloudy) over the majority of the CEU, most strikingly in June (Figure 5.7, right, ai). Ω_{700} (Figure 5.7, right, row b) also becomes positive, indicating subsidence, in the regions of the CEU that are beneath the high pressure system shown in Figure 5.4 b. The SAT anomalies (Figure 5.7, right, row c) in Year 200 are physically consistent with clear skies and subsiding air, but are largest in regions where the Q_H fraction is larger than average (Figure 5.7, right, row d). Soil moisture is drier than average over the whole CEU domain (Figure 5.7, right, row e), but the dry conditions only elevate the Q_H fraction in the regions of land surface feedback shown in Figure 5.6 a.

The PCE is an ensemble of 44 Year 200 heat waves, which can be assessed in terms

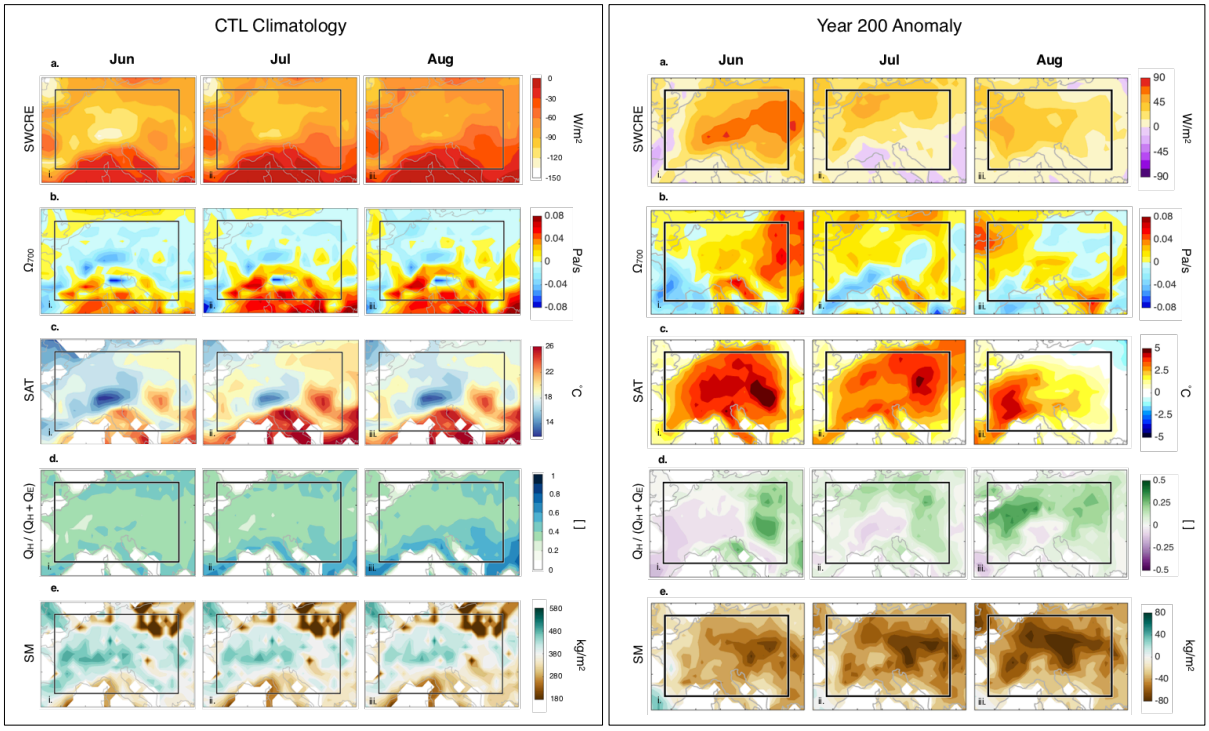

Figure 5.7: June, July, and August (i-iii) CTL climatology (left) and anomalies of Year 200 (right). Atmospheric fields are shown in the top two rows: (a) shortwave cloud radiative effect (SWCRE; W/m^2) and (b) vertical velocity in pressure coordinates at 700 hPa (Ω_{700}; Pa/s). SAT (°C) is shown in row (c). Field related to the land surface feedback are shown in the bottom two rows: (d) sensible heat flux fraction (Q_H/(Q_H+Q_E); W/m^2) and (e) soil moisture (SM; kg/m^2).

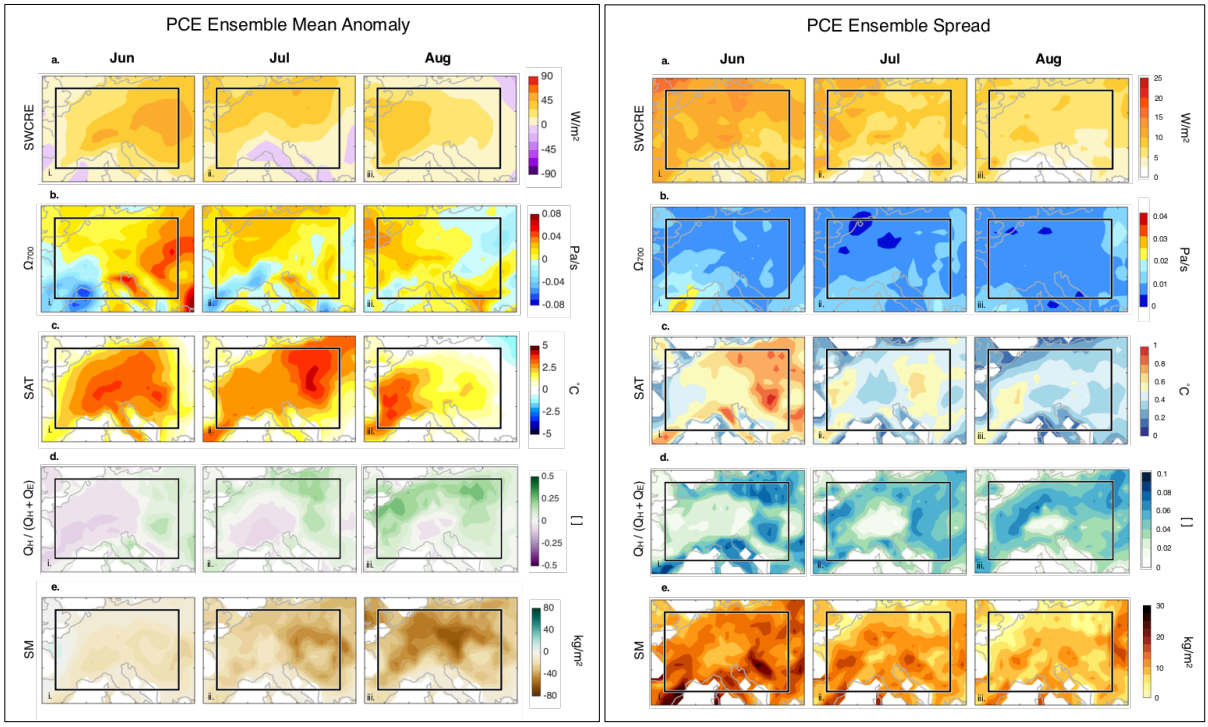

Figure 5.8: (left) As in Figure 5.7, but for the mean of the PCE anomalies. (right) As in Figure 5.7, but for the standard deviation across the PCE.

of ensemble mean (Figure 5.8, left) and standard deviation (Figure 5.8, right). The ensemble mean anomalies for all fields have similar spatial patterns to their Year 200 counterparts. This spatial similarity is not guaranteed, as only horizontal upper tropospheric winds are explicitly prescribed in the PCE. Owing to the diversity of initial soil moisture condition (Figure 5.2 a) and soil moisture memory, the ensemble mean of PCE soil moisture anomalies (Figure 5.8, left, row e) only slightly negative in June but converges to within about 35% of Year 200 in August.

The ensemble spread in the PCE is larger in June (i) than in August (iii) for all fields. For SAT (Figure 5.8, right, row c), the PCE spread is largest in the regions of maximum SAT anomaly: in the eastern CEU in June (i) and July (ii), and in the western CEU in August (iii). The SAT PCE spread is also elevated in the northeastern portion of the CEU in June (i), which then become the region of maximum SAT anomaly in July (ii), and western portion of the CEU in July (ii), which then becomes the region of maximum SAT anomaly in August (iii). The coincidence

between elevated SAT spread and maximum anomaly the following month suggests that it may be possible to identify where a heat wave will be most amplified a month in advance.

The evolution of heat wave SAT suggests that anticipating regions of extreme heat requires an understanding of the processes that introduce spread in PCE SAT. The land surface feedback is a candidate because the pattern of SAT PCE spread more closely resembles the pattern of Q_H fraction PCE spread (Figure 5.8,right, row d) than the patterns of SWCRE (Figure 5.8, right, row a) and Ω_{700} (Figure 5.8, right, row b) PCE spread. Q_H fraction PCE spread is larger (smaller) in regions where it is anomalously above (below) average (Figure 5.8, left, row d) and is nearly identical spatially to the Q_H fraction - soil moisture regression maps shown in Figure 5.6 a. This suggests that the land surface feedback is the process that introduces spread and amplifies PCE SAT the following month. Regions of maximum PCE soil moisture spread occur in the vicinity of the colocated SAT and Q_H fraction maximums, but are situated to the southwest of the eastern CEU maximum in June (Figure 5.8, right, ei) and July (Figure 5.8, right, eii) and to the southeast of the western CEU maximum in July. In August (Figure 5.8, right, eiii), the maximum PCE spreads of SAT, Q_H fraction, and soil moisture are all spatially colocated in the western CEU.

While colocated spread is suggestive of a relationship, correlations between CEU SAT and its associated fields provide a clearer picture of what makes one PCE member hotter than another. In Figure 5.9 b, we compare the CTL ensemble correlations with PCE correlations to determine the atmospheric and land surface associations with SAT in each case. Correlations between the June, July, and August CEU SAT timeseries' and concurrent SWCRE (i-iii), Ω_{700} (iv-vi), Q_H fraction (vii-ix), and soil moisture (x-xii) at each grid point are shown in the left panel of Figure 5.9 b for the CTL ensemble and in the right panel of Figure 5.9 b for the PCE. White regions of the maps indicate where correlations are not significant at the 95% confidence level (± 0.3 determined through a StudentâĂŹs T-test).

The CTL ensemble has approximately twice the spread of the PCE (Figure 5.9 a). We posit that SAT ensemble spread in the CTL is due to internal atmospheric variability. Each CTL

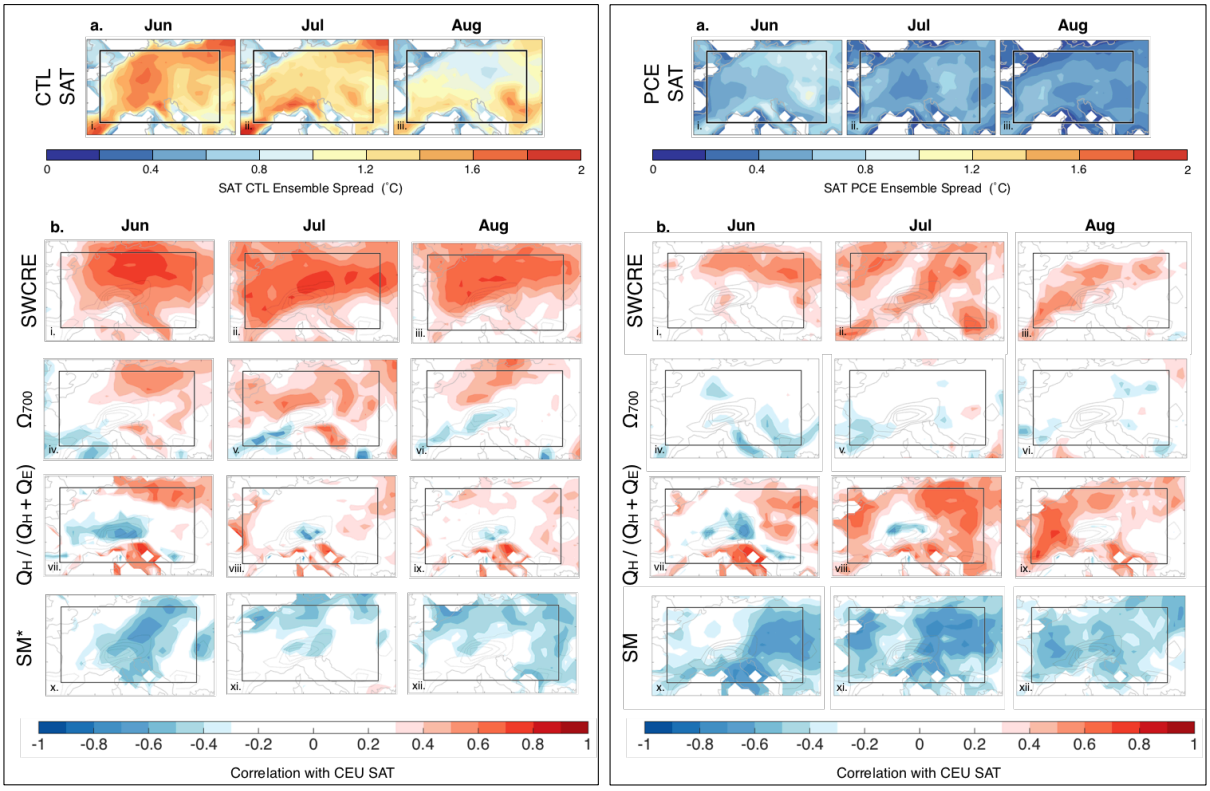

Figure 5.9: (left) The standard deviation of SAT (°C) across the CTL for June, July, and August (i-iii) are shown in (a). The correlation between CTL CEU SAT and associated fields at each grid point (color) are shown in (b). Dotted contours show orographic features above 600 m. Correlations with atmospheric fields, SWCRE (i-iii) and Ω_{700} (iv-vi), and surface fields, Q_H fraction (vii-ix) and SM (x-xii) illucidate potential relationships with CTL SAT ensemble spread. Because SM is not available for every CTL ensemble member, panels x-xii show correlations between CEU SAT and SM at each grid point for CTL years 1-44 (labelled SM*). (right) As in the left panel, but for the PCE.

ensemble member experiences a different atmospheric circulation pattern, which sets a different SAT pattern. Because of this atmospheric control, we expect that CEU SAT in the CTL ensemble will be highly correlated with the SWCRE, which is influenced by dynamics, and Ω_{700}, which is a direct indicator of dynamics.

The positive correlation between CTL CEU SAT and SWCRE over most of the CEU in June, July, and August suggest that cloud cover is key to whether or not a summer is hot (Figure 5.9 b, left, i-iii). As in the Year 200, hotter SAT accompanies clearer skies (less negative SWCRE). Correlations are higher in the northern portion of the CEU, where conditions are climatologically cloudier, than in the climatologically clearer southeastern CEU (Figure 5.7, left, row a). There is also a positive correlation between CTL CEU SAT and Ω_{700} in the northern portion of the CEU (Figure 5.9 b, left, iv-vi), which indicates that summers with more subsidence are hotter. Negative CEU SAT-Ω_{700} correlations are found in the southwestern portion of the CEU, in a region where, on average, downward motion is experienced (Figure 5.7, left, row b).

Correlations between CTL CEU SAT and Q_H fraction (Figure 5.9 b, left) are mixed in the CEU in June (vii), but tend to be not significant in the majority of the CEU in July (viii) and August (ix). This suggests that SAT in the CTL ensemble is more closely associated with atmospheric processes than land surface processes over most of the CEU domain. However, positive SAT-Q_H fraction correlations do occur in the CTL ensemble in the Mediterranean throughout the summer.

Because soil moisture is not available for every CTL ensemble year, we perform correlations between CEU SAT and soil moisture for years 1 through 44 of the CTL simulation (Figure 5.9, left panel, x-xii). The negative correlation between CEU SAT and soil moisture indicates that dry soils and hot summers coincide. While soil moisture can influence SAT, dry soils won't necessarily cause a summer to be hotter. A hotter summer will cause soils to be drier though, leading to the negative correlation.

By comparing CTL and PCE correlations, we aim to determine if the processes that

underpin CTL ensemble spread also govern heat wave intensity in the PCE. Overall, correlations between PCE CEU SAT and associated fields are of the same sign as their CTL counterparts, with the exception of Ω_{700} (Figure 5.9 b, right). This confirms that a hotter heat wave tends to have less cloud cover, a larger Q_H fraction, and drier soil moisture than a less intense heat wave. The lack of correlation between PCE CEU SAT and Ω_{700} is likely related to the minimal Ω_{700} spread in the PCE (Figure 5.8 b, right panel) that results from the prescribed atmospheric circulation constraint. Correlations between PCE CEU SAT and SWCRE (Figure 5.9 b, right, i-iii) are also weaker and occur over less of the CEU domain than the CTL CEU SAT and SWCRE correlations (Figure 5.9 b, left, i-iii). In contrast, the land surface process indicators, Q_H fraction and soil moisture, are more strongly correlated with PCE CEU SAT than CTL CEU SAT. The correlation between PCE CEU SAT and Q_H fraction is largest in regions where the PCE SAT spread is the largest and Q_H is influenced by soil moisture (Figure 5.6 a). This, in conjunction with strong negative correlations between PCE CEU SAT and soil moisture in the same CEU regions, suggests the land surface feedback affects the intensity of central European heat waves.

5.3.3 Role of preseason soil moisture

Because the land surface feedback has been shown to operate during a European heat wave, preseason soil moisture conditions may provide insight into the potential severity of a subsequent heat wave should atmospheric circulation induce one. Our objective is to quantify to what extent dry soils in May exacerbate heat wave conditions in the months that follow.

The heat wave we evaluate in the PCE begins in June and continues through August, which results in soil desiccation through the season. The rate at which soil dries out in the PCE is nonlinear, which is illustrated by the correlations between May CEU soil moisture and the change in CEU soil moisture between May and each successive month (ΔSM) shown in Figure 5.10. Correlations in the PCE are shown in blue and the PCE_{full} in teal. Because soil moisture is not available for all CTL ensemble members, CTL correlations (black) are presented in terms of

the mean (dots) and standard deviation (shading) of a bootstrap distribution of 100,000 CTL correlation coefficients, computed from ensembles of 44 randomly selected CTL simulation years.

Beneath the Year 200 heat wave, PCE and PCE_{full} members with drier initial soil moisture condition dried out more than their wetter counterparts, resulting in positive correlations between May CEU soil moisture and ΔSM from June through September. The magnitude of the correlations increased with time for both the PCE, from 0.32 in June to 0.91 in September, and the PCE_{full}, from 0.51 in June to 0.95 by September. Internal variability in the lower troposphere causes PCE correlations to be lower than PCE_{full} correlations. This evolution is suggestive of the land surface feedback's influence on soil moisture. When soils start out drier, the land surface feedback kicks in to elevate SAT, which in turn causes more soil desiccation. In contrast, when soils start out wetter and a heat wave occurs, there is a delay in the activation of the land surface feedback, buffering heat wave SAT and causing less total drying. This delayed activation is shown in the climatologically wetter northeastern CEU in Figure 5.3 ai.

In the CTL, there is not a clear relationship between initial soil moisture conditions and total soil desiccation, with the ensemble mean correlation remaining at or below 0.3 through the summer. This indicates that the land surface feedback is only active over the whole of central Europe during a heat wave, and that the potential to anticipate summer SAT from preseason soil moisture depend on atmospheric circulation patterns. The relationship between May CEU soil moisture and June-September CEU SAT, shown in Figure 5.11, demonstrates how the dependence of the land surface feedback on atmospheric circulation affects the predictive power of preseason soil moisture. As in Figure 5.10, PCE correlations are shown in blue, PCE_{full} in teal and the distribution of CTL correlations obtained through bootstrapping are shown in black.

For the PCE_{full}, drier (wetter) May soils result in hotter (cooler) CEU SAT; correlations increase from -0.68 in June to -0.92 in August. In the PCE, where both the land surface feedback and partially constrained internal atmospheric variability both contribute to heat wave SAT,

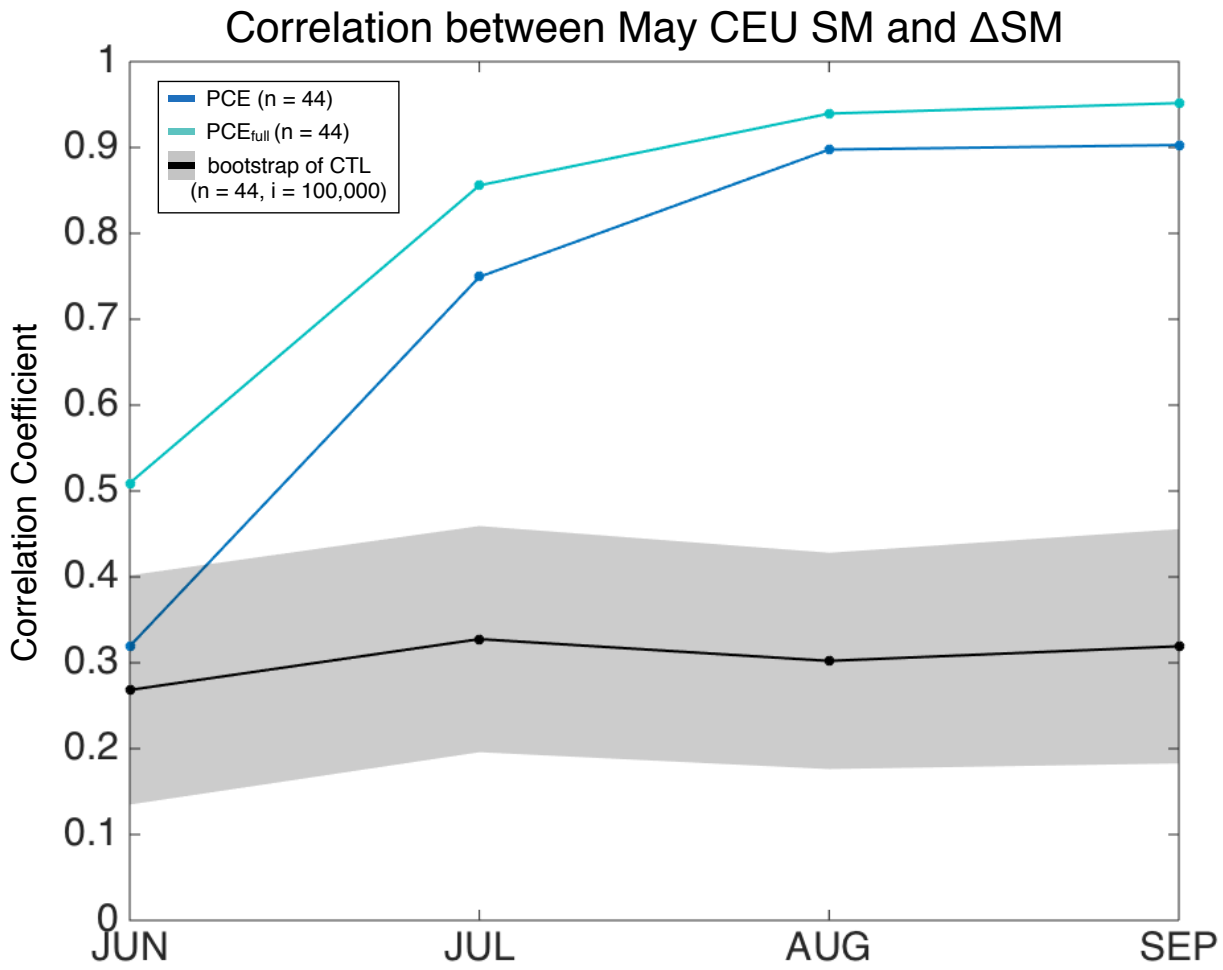

Figure 5.10: Correlation between May CEU soil moisture and change (Δ) in CEU soil moisture (i.e. June - May, July - May, etc.) for the PCE (blue) and the PCE_{full} (teal). A bootstrap scheme provides an estimate of preseason soil moisture-SAT correlations possible in the CTL simulation.

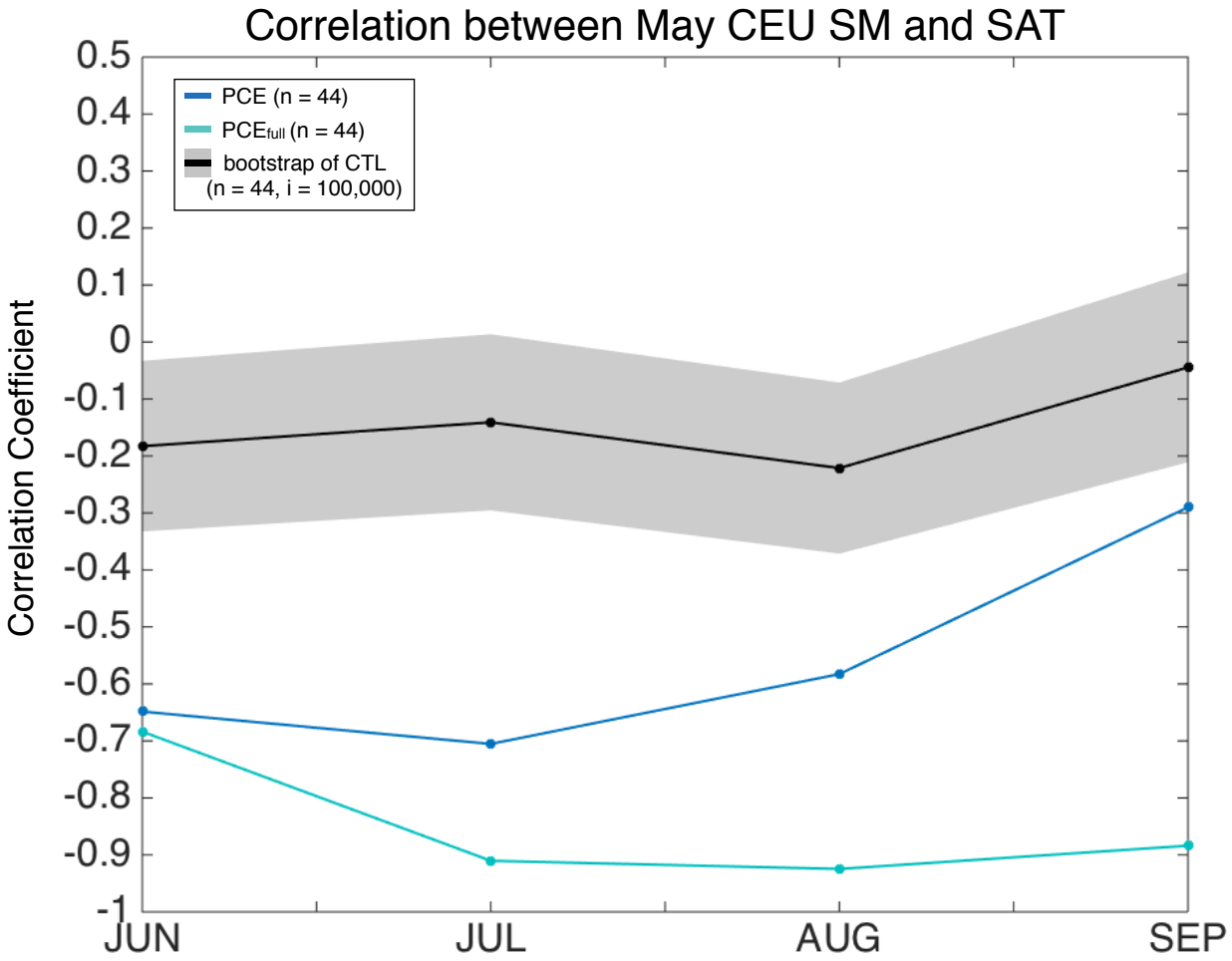

Figure 5.11: As in Figure 5.10, but for correlations between May CEU soil moisture and June-September CEU SAT

correlations increase from -0.65 in June to -0.71 in July, but decrease to -0.29 by September. In the CTL, with full internal atmospheric variability and no guarantee of a land surface feedback, correlations between May CEU soil moisture and summer CEU SAT remain around -0.2.

We quantify to what extent preseason soil moisture affects heat wave SAT in the CEU in Figure 5.12. Regression coefficients obtained by regressing SAT on normalized May soil moisture (σ_{SM}) at each grid point is shown for the PCE (i-iii) and the PCE_{full} (iv-vi). Both ensembles have similar spatial patterns and magnitudes consistent with their respective atmospheric constraints. In both PCE and PCE_{full}, SAT can be up to 0.5°C hotter in June if May soils are one standard deviation drier than the PCE average. The influence of preseason soil moisture persists in the PCE in regions of maximum SAT anomaly, with SAT being more than 0.4°C hotter per σ_{SM} reduction in the eastern CEU in July and western CEU in August. Due to SAT being more constrained by full column prescribed atmospheric circulation, PCE_{full} SAT increases about 0.25°C per σ_{SM} reduction.

A scatter plot of normalized May CEU soil moisture and CEU SAT for June, July, and August (Figure 5.12 bi-iii) summarizes the local regression analysis. CTL CEU SAT is shown in black to demonstrate the lack of clear linear relationship between preseason soil moisture and summer SAT that was determined through correlation in Figure 5.11. The PCE_{full} and PCE provide an idea of the upper and lower bounds on how much preseason soil moisture conditions exacerbated the Year 200 European heat wave: June SAT was 0.19-0.30°C hotter, July SAT was 0.16-0.24°C hotter, and August SAT was 0.11-0.17°C hotter for one σ_{SM} drier soils in May.

5.4 Summary

In this chapter, we demonstrate that drier spring soils result in hotter European heat waves at a rate of up to 0.5° per σ_{SM}. We use a global climate model framework to quantify the influence of preseason soil moisture, creating ensembles from a CESM control simulation

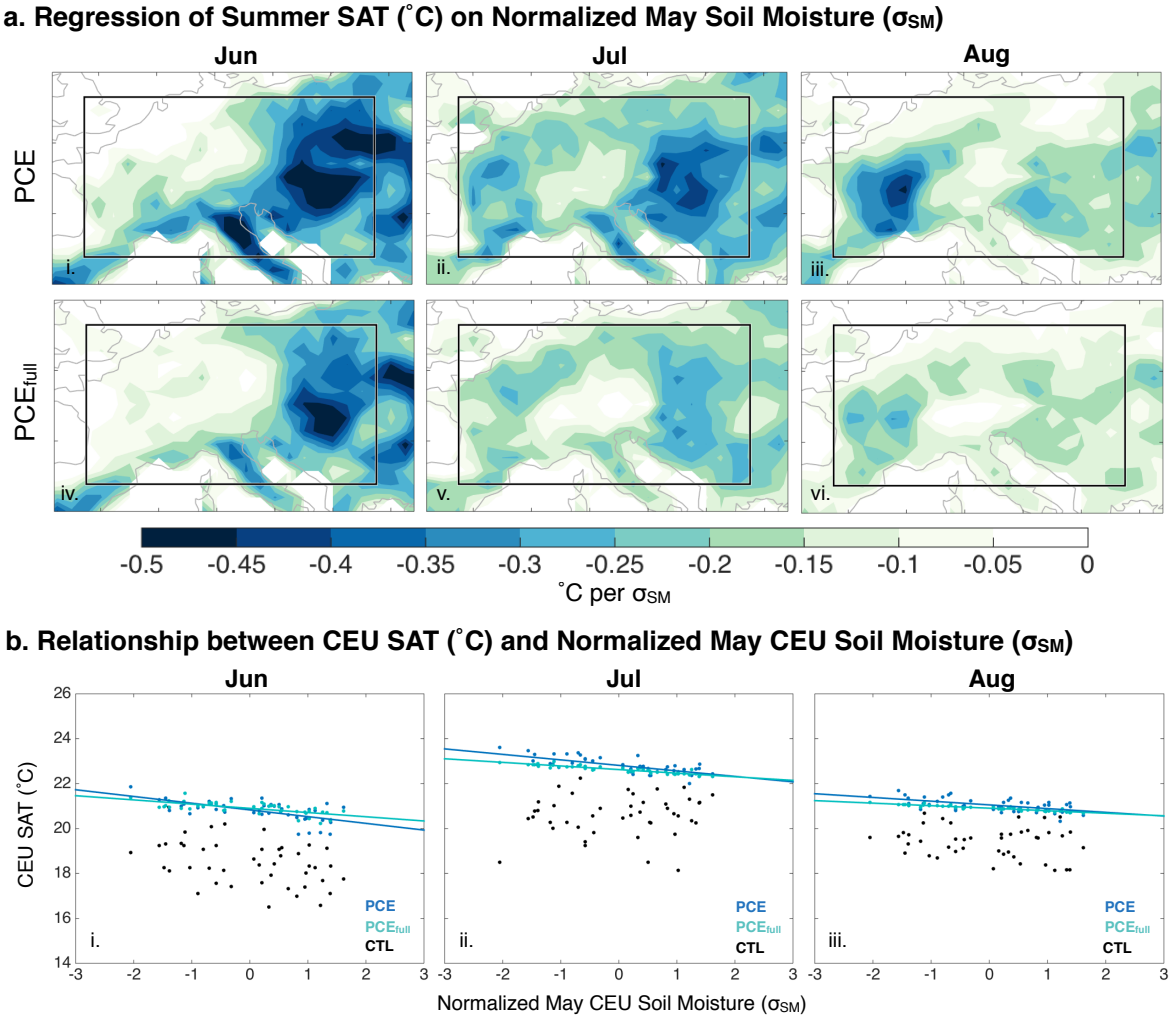

Figure 5.12: (a) Regression coefficient (°C / σ_{SM}) at each grid point, quantifying the relationship between normalized May soil moisture (σ_{SM}) and summer SAT (°C). Panels i-iii show PCE SAT and panels iv-vi show PCE_{full} SAT, both regressed on May σ_{SM}. (b) Scatter plots showing the relationship between normalized May CEU Soil Moisture (σ_{SM}) and CEU SAT in June (i), July (ii), and August (iii). PCE CEU SAT is shown in blue, PCE_{full} CEU SAT is shown in teal, and CTL CEU SAT is shown in black.

where each member has a unique initial land surface state and subsequently experiences the same atmospheric circulation pattern. The two prescribed circulation ensembles considered differ in terms of internal atmospheric variability, prescribing atmospheric circulation in the upper troposphere results in approximately twice as much SAT ensemble spread as prescribing atmospheric circulation over the whole model atmosphere. Vertical longitude sections show that prescribing circulation in the upper troposphere is sufficient to constrain atmospheric circulation below, ensuring that each member of the PCE has a spatially similar heat wave.

The state of the land surface is shown to contribute to the magnitude of PCE SAT. Soil moisture is shown to be closely related to the sensible heat flux fraction over most of central Europe during the heat wave. A PCE member with soils one standard deviation below the PCE average had about 2% increase in sensible heat relative to the total outgoing surface flux. Other factors that could introduce SAT spread in the PCE, such as the shortwave cloud radiative effect and vertical velocity at 700 hPa, were also assessed. SAT spread in the PCE is shown to be more closely related to indicators of the land surface feedback, while SAT spread in the original control run was shown to be more closely related to cloud cover and dynamics.

In terms of the land surface feedback, soil moisture both influenced and was influenced by PCE SAT. Drier initial soil moisture leads to a hotter heat wave, which in turn lead to more soil drying overall. This feedback relationship is not evident in the control run in general, which supports the conclusion that the influence of the land surface feedback in central Europe depends on attendant circulation patterns. Should a heat wave occur, drier soils in May exacerbate heat wave risk by triggering the land surface feedback in regions that it ordinarily would not operate.

Chapter 5, in part is currently being prepared for submission for publication of the material. Anna L. Merrifield, Isla Fischer, and Clara Deser. The dissertation/thesis author was the primary investigator and author of this material.

Chapter 6

Conclusion

Biases in simulating summer SAT variability over the continental US in climate models forced with observed sea surface temperatures are documented and investigated in Chapter 2. Regions of high SAT variability in the central U.S. are found to be related to regions of high sensible heat flux (Q_H) variability. This accordance between surface flux and temperature variability is not clear in observations. It is shown that models with Q_H-dominated SAT variability have higher values of mean evapotranspiration in the central US than models with circulation-associated SAT variability. These higher values aid in setting realistic SAT climatology in the central United States but contribute to additional SAT variability. Models with circulation-dominated SAT variability tend to have a climatological warm bias in the central United States, with mean summer SAT up to 8°C warmer than observed. This warm bias is tied to lower mean evapotranspiration in the region than observed, which results in the land surface having a more realistic influence on SAT variability. All models evaluated appear to have some manner of land surface-associated SAT bias in the central US.

It is demonstrated that the method of dynamical adjustment can be used to further our understanding of land-surface driven SAT variability in the central US in Chapters 3 and 4. Removing the effects of circulation on SAT in the CESM Large Ensemble reveals the central US

as the primary region where SAT variability remains after dynamical adjustment. This residual SAT variability is shown to have temporal characteristics consistent with soil moisture memory. A more comprehensive thermodynamic narrative is developed for residual SAT based on lead-lag relationships with soil moisture and colocated covariability between SAT and SLP in the hotspot. Residual SAT in the central US is shown to be more correlated with preseason soil moisture than total hotspot SAT, which supports the hypothesis that dynamical adjustment reveals the land surface influence by removing the confounding effects of atmospheric variability. The magnitude of method uncertainty for dynamical adjustment is determined by comparing residual SAT is fixed and interactive soil moisture simulations. The possibility of thermodynamic contamination of the dynamic component is documented and optimal methodological choices for defining an SAT-based land-atmosphere hot spot metric are discussed.

The influence of the land surface on a persistent European heat wave is assessed in Chapter 5. Initial condition ensembles are created in a general circulation model framework to evaluate land surface influence, each ensemble member has different initial land surface conditions but experiences the same heat wave-inducing atmospheric circulation pattern. With this experimental framework, both the influence of a heat wave on soil moisture and the influence of soil moisture on a heat wave are investigated. The land-atmosphere coupling is shown to depend on initial soil conditions, as regions in central and western Europe must dry out before the land surface feedback begins to operate. A comparison to an ensemble of CTL members demonstrates that while European SAT is more closely related to cloud cover and dynamics in general, the land surface feedback can amplify or damp SAT by a few degrees during a heat wave. A heat wave following a dry spring can be up to 3°C hotter than a heat wave that follows a wet spring.

References

Barnes, E. and Screen, J. (2015). The impact of Arctic warming on the midlatitude jet-stream: Can it? has it? will it? *WIREs Clim Change*, 6:277–286.

Beniston, M., Stephenson, D. B., Christensen, O. B., Ferro, C. A. T., Frei, C., Goyette, S., Halsnaes, K., Holt, T., Jylh, K., Koffi, B., Palutikof, J., Schll, R., Semmler, T., and Woth, K. (2007). Future extreme events in European climate: an exploration of regional climate model projections. *Climatic Change*, 81:71–95.

Berg, A., Lintner, B., Findell, K., and Giannini, A. (2017). Soil Moisture Influence on Seasonality and Large-Scale Circulation in Simulations of the West African Monsoon. *J. Climate*, 30:2295–2317.

Berg, A., Lintner, B. R., Findell, K. L., Malyshev, S., Loikith, P. C., and Gentine, P. (2014). Impact of Soil Moisture–Atmosphere Interactions on Surface Temperature Distribution. *J. Climate*, 27:7976–7993.

Betts, A. K., Ball, J. H., Beljaars, A. C. M., Miller, M. J., and Viterbo, P. A. (1996). The land surface-atmosphere interaction: A review based on observational and global modeling perspectives. *J. Geophys. Res.*, 101:7209–7225.

Black, E., Blackburn, M., Harrison, G., and Methven, J. (2004). Factors contributing to the summer 2003 European heat wave. *Weather*, 59:217–223.

Branstator, G. and Teng, H. (2017). Tropospheric Waveguide Teleconnections and Their Seasonality. *J. Atmos. Sci.*, 74:1513–1532.

Brohan, P., Kennedy, J. J., Harris, I., Tett, S. F. B., and Jones, P. D. (2006). Uncertainty estimates in regional and global observed temperature changes: A new data set from 1850. *J. Geophys. Res.*, 111:D12106.

Cassou, C., Terray, L., and Phillips, A. (2005). Tropical Atlantic Influence on European Heat Waves. *J. Climate*, 18:2805–2811.

Charney, J. and DeVore, J. (1979). Multiple flow equilibria in the atmosphere and blocking. *J. Atmos. Sci.*, 36:1205–1216.

Cheruy, F., Dufresne, J. L., Hourdin, F., and Ducharne, A. (2014). Role of clouds and land-atmosphere coupling in midlatitude continental summer warm biases and climate change amplification in CMIP5 simulations. *Geophys. Res. Lett.*, 41:6493–6500.

Coumou, D., Lehmann, J., and Beckmann, J. (2015). The weakening summer circulation in the Northern Hemisphere mid-latitudes. *Science*, 348:324–327.

Davis, R. E., Hayden, B. P., Gay, D. A., Phillips, W. L., and Jones, G. V. (1997). The North Atlantic subtropical anticyclone. *J. Climate*, 10:728–744.

Della-Marta, P., Luterbacher, J., von Weissenfluh, H., Xoplaki, E., Brunet, M., and Wanner, H. (2007). Warm Season Subseasonal Variability and Climate Extremes in the Northern Hemisphere: The Role of Stationary Rossby Waves. *Clim. Dyn.*, 29:251–275.

Deser, C., Phillips, A., Alexander, M. A., and Smoliak, B. V. (2014). Projecting North American climate over the next 50 years: Uncertainty due to internal variability. *J. Climate*, 27:2271–2296.

Deser, C., Walsh, J., , and Timlin, M. (1993). Arctic Sea Ice Variability in the Context of Recent Atmospheric Circulation Trends. *J. Climate*, 13:617–633.

Deser, C. A., Terray, L., and Phillips, A. S. (2016). Forced and internal components of winter air temperature trends over North America during the past 50 years: Mechanisms and implications. *J. Climate*, 29:2237–2258.

Diffenbaugh, N. S., Pal, J. S., Giorgi, F., and Gao, X. (2007). Heat stress intensification in the Mediterranean climate change hotspot. *Geophys. Res. Lett.*, 34:L11706.

Dirmeyer, P. A. (2011). The terrestrial segment of soil moisture-climate coupling. *Geophys. Res. Lett.*, 38:L16702.

Egger, J. (1978). Dynamics of blocking highs. *J. Atmos. Sci.*, 35:1788–1801.

Fast, J. and McCorcle, M. (1991). The Effect of Heterogeneous Soil Moisture on a Summer Baroclinic Circulation in the Central United States. *Mon. Wea. Rev.*, 119:2140–2167.

Ferguson, C. R., Wood, E. F., and Vinukollu, R. K. (2012). A Global Intercomparison of Modeled and Observed Land-Atmosphere Coupling. *J. Hydrometeor*, 13:749–784.

Ferranti, L. and Viterbo, P. (2006). The european Summer of 2003: Sensitivity to Soil Water Initial Conditions. *J. Climate*, 19:3659–3680.

Findell, K. and Eltahir, E. (2003a). The impact of El Niño-Southern Oscillation on maximum temperature extremes. *J. Hydrometeorol.*, 4:570–583.

Findell, K. L. (2015). Data length requirements for observational estimates of land-atmosphere coupling strength. *J. Hydrometeor.*, 16:1615–1635.

Findell, K. L. and Eltahir, E. A. (2003b). Atmospheric Controls on Soil Moisture-Boundary Layer Interactions. Part II: Feedbacks within the Continental United States. *J. Hydrometeorol.*, 4:570–583.

Findell, K. L., Gentine, P., Lintner, B. R., and Kerr, C. (2011). Probability of afternoon precipitation in eastern United States and Mexico enhanced by high evaporation. *Nat. Geosci.*, 4:434–439.

Fischer, E., Seneviratne, S., Lüthi, D., and Schär, C. (2007a). Contribution of landâĂŘatmosphere coupling to recent European summer heat waves. *Geophys. Res. Lett.*, 34:L06707.

Fischer, E., Seneviratne, S., Vidale, P., Lüthi, D., and Schär, C. (2007b). Soil Moisture–Atmosphere Interactions during the 2003 European Summer Heat Wave. *J. Climate*, 20:5081–5097.

Fischer, E. M. and Schär, C. (2009). Future changes in daily summer temperature variability: driving processes and role for temperature extremes. *Climate Dyn.*, 33:917–935.

Ford, T. W. and Quiring, S. M. (2014). In situ soil moisture coupled with extreme temperatures: A study based on the Oklahoma Mesonet. *Geophys. Res. Lett.*, 41:4727–4734.

Gates, W. L. (1992). Amip: the atmospheric model intercomparison project. *Bull. Amer. Meteor. Soc.*, 73:1962–1970.

Guo, Z., Dirmeyer, P., Koster, R., Sud, Y., Bonan, G., Oleson, K., Chan, E., Verseghy, D., Cox, P., Gordon, C., McGregor, J., Kanae, S., Kowalczyk, E., Lawrence, D., Liu, P., Mocko, D., Lu, C., Mitchell, K., Malyshev, S., McAvaney, B., Oki, T., Yamada, T., Pitman, A., Taylor, C., Vasic, R., and Xue, Y. (2006). GLACE: The Global Land-Atmosphere Coupling Experiment. Part II: Analysis. *J. Hydrometeor.*, 7:611–625.

Guo, Z. and Dirmeyer, P. A. (2013). Interannual variability of land-atmosphere coupling strength. *J. Hydrometeorol.*, 14:1636–1646.

Haarsma, R. J., Selten, F., van den Hurk, B., Hazeleger, W., and Wang, X. (2009). Drier Mediterranean soils due to greenhouse warming bring easterly winds over summertime central Europe. *Geophys. Res. Lett.*, 36:L04705.

Hansen, J., Sato, M., and Ruedy, R. (2012). Perception of climate change. *Proc. Natl. Acad. Sci.*, 109(37):E2415 – E2423.

Heck, P., Lüthi, D., Wernli, H., and Schär, C. (2001). Climate impacts of European-scale anthropogenic vegetation changes: A study with a regional climate model. *J. Geophys. Res.*, 106:7817–7835.

Hirschi, M., Mueller, B., Dorigo, W., and Seneviratne, S. (2014). Using remotely sensed soil moisture for land-atmosphere coupling diagnostics: The role of surface vs. root-zone soil moisture variability. *Remote Sensing of Environment*, 154:246–252.

Hirschi, M., Seneviratne, S. I., Alexandrov, V., Boberg, F., Boroneant, C., Christensen, O. B., Formayer, H., Orlowsky, B., and Stepanek, P. (2011). Observational evidence for soil-moisture impact on hot extremes in southeastern Europe. *Nat. Geosci.*, 4:17–21.

Hurrell, J. (2015). Climate and Climate Change | Climate Variability: North Atlantic and Arctic Oscillation. In North, G. R., Pyle, J., and Zhang, F., editors, *Encyclopedia of Atmospheric Sciences (Second Edition)*, pages 47–60. Academic Press, 2 edition.

Jaeger, E. and Seneviratne, S. (2011). Impact of soil moisture-atmosphere coupling on European climate extremes and trends in a regional climate model. *Climate Dyn.*, 36:1919–1939.

Jimenez, P., de Arellano, J., Navarro, J., and Gonzalez-Rouco, J. (2014). Understanding Land-Atmosphere Interactions across a Range of Spatial and Temporal Scales. *Bull. Amer. Meteor. Soc.*, 95:ES14–ES17.

Johnson, R. (2003). Thermal low. In Holton, J., Pyle, J., and Curry, J., editors, *Encyclopedia of Atmospheric Science*, pages 2269–2273. Academic Press: London.

Kalnay, E., Kanamitsu, M., Kistler, R., Collins, W., Deaven, D., L. Gandin, M. I., Saha, S., White, G., Woollen, J., Zhu, Y., Chelliah, M., Ebisuzaki, W., Higgins, W., Janowiak, J., Mo, K., Ropelewski, C., Wang, J., Leetmaa, A., Reynolds, R., Jenne, R., and Joseph, D. (1996). The NCEP/NCAR 40-Year Reanalysis Project. *Bull. Amer. Meteor. Soc.*, 77:437–472.

Kay, J. E., Deser, C., Phillips, A., Mai, A., Hannay, C., Strand, G., Arblaster, J., Bates, S., Danabasoglu, G., Edwards, J., Holland, M., Kushner, P., Lamarque, J. F., Lawrence, D., Lindsay, K., Middleton, A., Munoz, E., Neale, R., Oleson, K., Polvani, L., and Vertenstein, M. (2015). The Community Earth System Model (CESM) Large Ensemble Project: A community resource for studying climate change in the presence of internal climate variability. *Bull. Amer. Met. Soc.*, 96:1333–1349.

Koster, R., Chang, Y., Wang, H., and Schubert, S. (2016). Impacts of Local Soil Moisture Anomalies on the Atmospheric Circulation and on Remote Surface Meteorological Fields during Boreal Summer: A Comprehensive Analysis over North America. *J. Climate*, 29:7345–7364.

Koster, R. D., Dirmeyer, P. A., Guo, Z., Bonan, G., Chan, E., Cox, P., Gordon, C. T., Kanae, S., Kowalczyk, E., Lawrence, D., Liu, P., Lu, C.-H., Malyshev, S., McAvaney, B., Mitchell, K., Mocko, D., Oki, T., Oleson, K., Pitman, A., Sud, Y. C., Taylor, C. M., Verseghy, D., Vasic, R., Xue, Y., and Yamada, T. (2004a). Regions of Strong Coupling Between Soil Moisture and Precipitation. *Science*, 305:1138–1140.

Koster, R. D., Mahanama, S. P. P., Yamada, T. J., Balsamo, G., Berg, A. A., Boisserie, M., Dirmeyer, P. A., Doblas-Reyes, F. J., Drewitt, G., Gordon, C. T., Z. Guo, J.-H. J., Lee, W.-S., Li, Z., Luo, L., Malyshev, S., Merryfield, W. J., Seneviratne, S. I., Stanelle, T., van den Hurk, B. J. J. M., Vitart, F., and Wood, E. F. (2011). The Second Phase of the Global Landï£¡Atmosphere Coupling Experiment: Soil Moisture Contributions to Subseasonal Forecast Skill. *J. Hydrometeor.*, 12:805–822.

Koster, R. D., Suarez, M., Liu, P., Jambor, U., Berg, A., Kistler, M., Reichle, R., Rodell, M., and Famiglietti, J. (2004b). Realistic initialization of land surface states: Impacts on subseasonal forecast skill. *J. Hydrometeor.*, 5:1049–1063.

Koster, R. D., Sud, Y. C., Guo, Z., Dirmeyer, P. A., Bonan, G., Oleson, K. W., Chan, E., Verseghy, D., Cox, P., Davies, H., Kowalczyk, E., Gordon, C. T., Kanae, S., Lawrence, D., Liu, P., Mocko, D., Lu, C.-H., Mitchell, K., Malyshev, S., McAvaney, B., Oki, T., Yamada, T., Pitman, A., Taylor, C. M., Vasic, R., and Xue, Y. (2006). GLACE: The Global Land-Atmosphere Coupling Experiment. Part I: Overview. *J. Hydrometeor.*, 7:590–610.

Krakauer, N. Y., Cook, B. I., and Puma, M. J. (2010). Contribution of soil moisture feedback to hydroclimatic variability. *Hydrol. Earth Syst. Sci.*, 14:505–520.

Kushnir, Y., Seager, R., Ting, M., Naik, N., and Nakamura, J. (2010). Mechanisms of Tropical Atlantic SST Influence on North American Precipitation Variability. *J. Climate*, 23:5610–5628.

Lawrence, D. M., Oleson, K. W., Flanner, M. G., Thornton, P. E., Swenson, S. C., Lawrence, P. J., Zeng, X., Yang, Z., Levis, S., Sakaguchi, K., Bonan, G. B., and Slater, A. G. (2011). Parameterization improvements and functional and structural advances in version 4 of the Community Land Model. *J. Adv. Model. Earth Syst.*, 3:1–27.

Lehner, F., Deser, C., and Terray, L. (2017). Toward a New Estimate of "Time of Emergence" of Anthropogenic Warming: Insights from Dynamical Adjustment and a Large Initial-Condition Model Ensemble. *J. Climate*, 30:7739–7756.

Lewis, J. (2003). Ooishi's observation. *Bull. Amer. Meteor. Soc.*, 84:357–370.

Li, W., Li, L., Fu, R., Deng, Y., and Wang, H. (2011). Changes to the North Atlantic Subtropical High and Its Role in the Intensification of Summer Rainfall Variability in the Southeastern United States. *J. Climate*, 24:1499–1506.

Lorenz, E. N. (1969). Atmospheric predictability as revealed by naturally occurring analogues. *J. Atmos. Sci.*, 26:636–646.

Lorenz, R., Argüeso, D., Donat, M. G., Pitman, A. J., van den Hurk, B., Berg, A., Lawrence, D. M., Chéruy, F., Ducharne, A., Hagemann, S., Meier, A., Milly, P. C. D., and Seneviratne, S. I. (2016). Influence of land-atmosphere feedbacks on temperature and precipitation extremes in the GLACE-CMIP5 ensemble. *Geophys. Res. Atmos.*, 121:607–623.

Lorenz, R., Jaeger, E. B., and Seneviratne, S. I. (2010). Persistence of heat waves and its link to soil moisture memory. *Geophys. Res. Lett.*, 37:L09703.

Lorenz, R., Pitman, A. J., Hirsch, A. L., and Srbinovsky, J. (2015). Intraseasonal versus Interannual Measures of Land-Atmosphere Coupling Strength in a Global Climate Model: GLACE-1 versus GLACE-CMIP5 Experiments in ACCESS1.3b. *J. Hydrometeor.*, 16:2276–2295.

Meehl, G., Washington, W., Arblaster, J., Hu, A., Teng, H., Kay, J., Gettelman, A., Lawrence, D., Sanderson, B., and Strand, W. (2013). Climate Change Projections in CESM1(CAM5) Compared to CCSM4. *J. Climate*, 26:6287–6308.

Meehl, G. A. and Tebaldi, C. (2004). More Intense, More Frequent, and Longer Lasting Heat Waves in the 21st Century. *Science*, 305:994–997.

Merrifield, A. and Xie, S. (2016). Summer U.S. Surface Air Temperature Variability: Controlling Factors and AMIP Simulation Biases. *J. Climate*, 29:5123–5139.

Merrifield, A. L., Lehner, F., Xie, S.-P., and Deser, C. (2017). Removing circulation effects to assess central U.S. land-atmosphere interactions in the CESM Large Ensemble. *Geophys. Res. Lett.*, 44:9938–9946.

Miralles, D. G., Teuling, A. J., van Heerwaarden, C. C., and de Arellano, J. V.-G. (2014). Mega-heatwave temperatures due to combined soil desiccation and atmospheric heat accumulation. *Nat. Geosci.*, 7:345–349.

Miralles, D. G., van den Berg, M., Teuling, R., and Jeu, R. D. (2012). Soil moisture-temperature coupling: A multiscale observational analysis. *Geophys. Res. Lett.*, 39:L21707.

Mueller, B. and Seneviratne, S. (2014). Systematic land climate and evapotranspiration biases in CMIP5 simulations. *J. Hydrometeor*, 41:128–134.

Neale, R. B., Richter, J., Park, S., Lauritzen, P. H., Vavrus, S. J., Rasch, P. J., and Zhang, M. (2013). The mean climate of the Community Atmosphere Model (CAM4) in forced SST and fully coupled experiments. *J. Climate*, 26 (14):5150–5168.

Nigam, S. and Ruiz-Barradas, A. (2006). Seasonal hydroclimate variability over North America in global and regional reanalyses and AMIP Simulations: a mixed assessment. *J. Climate*, 19:815–837.

Oki, T. and Kanae, S. (2006). Global hydrological cycles and world water resources. *Science*, 313:1068–1072.

Perkins, S. E. (2015). A review on the scientific understanding of heatwaves-their measurement, driving mechanisms, and changes at the global scale. *Atmospheric Research*, 164:242–267.

Petoukhov, V., Rahmstorf, S., Petri, S., and Schellnhuber, H. J. (2013). Quasiresonant amplification of planetary waves and recent northern hemisphere weather extremes. *Proc. Natl. Acad. Sci. (USA)*, 110:5336–5341.

Phillips, T. J. and Klein, S. A. (2014). Land-atmosphere coupling manifested in warm-season observations on the U.S. southern great plains. *J. Geophys. Res. Atmos.*, 119:509–528.

Quesada, B., Vautard, R., Yiou, P., Hirschi, M., and Seneviratne, S. I. (2012). Asymmetric European summer heat predictability from wet and dry southern winters and springs. *Nature Climate Change*, 2:736–741.

Riahi, K., Rao, S., Krey, V., Cho, C., Chirkov, V., Fischer, G., Kindermann, G., Nakicenovic, N., and Rafaj, P. (2011). RCP 8.5âĂŤA scenario of comparatively high greenhouse gas emissions. *Climatic Change*, 109:33–57.

Robine, J.-M., Cheung, S. L. K., Roy, S. L., Oyen, H. V., Griffiths, C., Michel, J.-P., and Herrmann, F. R. (2008). Death toll exceeded 70,000 in Europe during the summer of 2003. *Comptes Rendus Biologies*, 331:171–178.

Ruiz-Barradas, A. and Nigam, S. (2005). Warm Season Rainfall Variability over the U.S. Great Plains in Observations, NCEP and ERA-40 Reanalyses, and NCAR and NASA Atmospheric Model Simulations. *J. Climate*, 18:1808–1830.

Ruiz-Barradas, A. and Nigam, S. (2006). IPCC's 20th century climate simulations: varied representations of North American hydroclimate variability. *J. Climate*, 19:4041–4058.

Ruiz-Barradas, A. and Nigam, S. (2013). Atmosphere-Land Surface Interactions over the Southern Great Plains: Characterization from Pentad Analysis of DOE ARM Field Observations and NARR. *J. Climate*, 26:875–886.

Saffioti, C., Fischer, E., and Knutti, R. (2017). Improved Consistency of Climate Projections over Europe after Accounting for Atmospheric Circulation Variability. *J. Climate*, 30:7271–7291.

Santanello, J., Dirmeyer, P., Ferguson, C., Findell, K., Tawfik, A., Berg, A., Ek, M., Gentine, P., Guillod, B., van Heerwaarden, C., Roundy, J., and Wulfmeyer, V. (2017). Land-Atmosphere Interactions: The Loco Perspective. *Bull. Amer. Meteor. Soc.*

Schär, C. and Jendritzky, G. (2004). Hot news from summer 2003. *Nature*, 432:559–560.

Schubert, S., Wang, H., and Suarez, M. (2011). Warm Season Subseasonal Variability and Climate Extremes in the Northern Hemisphere: The Role of Stationary Rossby Waves. *J. Climate*, 24:4773–4792.

Seager, R., Harnik, N., Kushnir, Y., Robinson, W., and Miller, J. (2003). Mechanisms of hemispherically symmetric climate variability. *J. Climate*, 16:2960–2978.

Seneviratne, S., Corti, T., Davin, E., Hirschi, M., Jaeger, E., Lehner, I., Orlowsky, B., and Teuling, A. (2010). Investigating soil moisture–climate interactions in a changing climate: a review. *Earth-Sci. Rev.*, 99:125–161.

Seneviratne, S., Koster, R., Guo, Z., Dirmeyer, P., Kowalczyk, E., Lawrence, D., Liu, P., Lu, C.-H., Mocko, D., Oleson, K., and Verseghy, D. (2006a). Soil moisture memory in agcm simulations: analysis of global landâĂŞatmosphere coupling experiment (glace) data. *J. Hydrometeorol.*, 7:1090–1112.

Seneviratne, S., Lüthi, D., Litschi, M., and Schär, C. (2006b). Land-atmosphere coupling and climate change in Europe. *Nature*, 443:205–209.

Seneviratne, S. I., Wilhelm, M., Stanelle, T., van den Hurk, B., Hagemann, S., Berg, A., Cheruy, F., Higgins, M. E., Meier, A., Brovkin, V., Claussen, M., Ducharne, A., Dufresne, J., Findell, K. L., Ghattas, J., Lawrence, D. M., Malyshev, S., Rummukainen, M., and Smith, B. (2013). Impact of soil moisture-climate feedbacks on CMIP5 projections: First results from the GLACE-CMIP5 experiment. *Geophys. Res. Lett.*, 40:5212–5217.

Sheffield, J., Camargo, S. J., Fu, R., Hu, Q., Jiang, X., Johnson, N., Karnauskas, K. B., Kim, S. T., Kinter, J., Kumar, S., Langenbrunner, B., Maloney, E., Mariotti, A., Meyerson, J. E., Neelin, J. D., Nigam, S., Pan, Z., Ruiz-Barradas, A., Seager, R., Serra, Y. L., Sun, D.-Z., Wang, C., Xie, S.-P., Yu, J.-Y., Zhang, T., and Zhao, M. (2013). North American climate in CMIP5 experiments. Part II: Evaluation of historical simulations of intraseasonal to decadal variability. *J. Climate*, 26:9247–9290.

Shukla, J. and Mintz, Y. (1982). Influence of land-surface evapotranspiration on the Earth's climate. *Science*, 215:1498–1501.

Smoliak, B., Wallace, J., Lin, P., and Fu, Q. (2015). Dynamical Adjustment of the Northern Hemisphere Surface Air Temperature Field: Methodology and Application to Observations. *J. Climate*, 28:1613–1629.

Song, H.-J., Ferguson, C. R., and Roundy, J. K. (2016). Land-Atmosphere Coupling at the Southern Great Plains Atmospheric Radiation Measurement (ARM) Field Site and Its Role in Anomalous Afternoon Peak Precipitation. *J. Geophys. Res. Atmos.*, 17:541–556.

Tawfik, A. B., Dirmeyer, P. A., and Santanello, J. A. (2015a). The heated condensation framework. Part I: Description and Southern Great Plains case study. *J. Hydrometeor.*, 16:1929–1945.

Tawfik, A. B., Dirmeyer, P. A., and Santanello, J. A. (2015b). The heated condensation framework. Part II: Climatological behavior of convective initiation and land-atmosphere coupling over the conterminous United States. *J. Hydrometeor.*, 16:1946–1961.

Taylor, K. E., Stouffer, R. J., and Meehl, G. A. (2012). An Overview of CMIP5 and the Experiment Design. *Bull. Amer. Meteor. Soc.*, 93:485–498.

Trenberth, K. (1978). On the Interpretation of the Diagnostic Quasi-Geostrophic Omega Equation. *Mon. Wea. Rev.*, 106:131–137.

Trenberth, K., Fasullo, J., and Kiehl, J. (2009). Earth's global energy budget. *Bull. Amer. Meteor. Soc.*, 90 (3):311–323.

Trenberth, K. and Paolino, D. (1980). The Northern Hemisphere Sea-Level Pressure Data Set: Trends, Errors and Discontinuities. *Mon. Wea. Rev.*, 108:855–872.

van den Dool, H. M. (1994). Searching for analogues, how long must we wait? *Tellus A*, 46:314–324.

Vautard, R., Yiou, P., D'Andrea, F., de Noblet, N., Viovy, N., Cassou, C., Polcher, J., Ciais, P., Kageyama, M., and Fan, Y. (2007). Summertime European heat and drought waves induced by wintertime Mediterranean rainfall deficit. *Geophys. Res. Lett.*, 34:L07711.

Vidale, P. L., Lüthi, D., Wegmann, R., and Schär, C. (2007). European summer climate variability in a heterogeneous multi-model ensemble. *Climatic Change*, 81:209–232.

Vogel, M. M., Orth, R., Cheruy, F., Hagemann, S., Lorenz, R., van den Hurk, B., and Seneviratne, S. (2017). Regional amplification of projected changes in extreme temperature strongly controlled by soil moisture-temperature feedbacks. *Geophys. Res. Lett.*, 44:1944–8007.

Wallace, J., Fu, Q., Smoliak, B. V., Lin, P., and Johanson, C. M. (2012). Simulated versus observed patterns of warming over the extratropical Northern Hemisphere continents during the cold season. *Proc. Natl. Acad. Sci. (USA)*, 109:14337–âĂŞ14342.

Wallace, J. M., Zhang, Y., and Renwick, J. A. (1995). Dynamic contribution to hemispheric mean temperature trends. *Science*, 270:780–783.

Wilson, A. and Barros, A. (2017). Orographic Land-Atmosphere Interactions and the Diurnal Cycle of Low-Level Clouds and Fog. *J. Hydrometeor.*, 18:1513–1533.

Wu, W. and Dickinson, R. E. (2005). Warm-season rainfall variability over the U.S. Great Plains and its correlation with evapotranspiration in a climate simulation. *Geophys. Res. Lett.*, 32:L17402.

Zampieri, M., F. D'Andrea, R. V., Ciais, P., de Noblet-Ducoudré, N., and Yiou, P. (2009). Hot European Summers and the Role of Soil Moisture in the Propagation of Mediterranean Drought. *J. Climate*, 22:4747–4758.

Zhang, J., Wang, W.-C., and Leung, L. R. (2008). Contribution of land-atmosphere coupling to summer climate variability over the contiguous United States. *J. Geophys. Res.*, 113:D22109.

Zhou, Z.-Q., Xie, S.-P., Zheng, X.-T., Liu, Q., and Wang, H. (2014). Global warming-induced changes in El Niño teleconnections over the North Pacific and North America. *J. Climate*, 27:9050–9064.